

Annual Report

5 June 1973-4 June 1974

ANALYTICS OF CRYSTAL GROWTH IN SPACE

by

William R. Wilcox

Chong E. Chang

Paul J. Shlichta

Pei-Shiun Chen

Chong K. Kim

Distribution of this report is provided in the interest of  
information exchange. Responsibility for the contents  
resides with the authors.

Prepared under Contract No. NAS8-29847

UNIVERSITY OF SOUTHERN CALIFORNIA

Chemical Engineering Department

Los Angeles, California 90007

For

NASA-GEORGE C. MARSHALL SPACE FLIGHT CENTER

# ANALYTICS OF CRYSTAL GROWTH IN SPACE

by

William R. Wilcox, Chong E. Chang, Paul J. Shlichta,  
Pei-Shiun Chen, and Chong E. Kim

University of Southern California  
Los Angeles, California 90007

## ABSTRACT

Two crystal growth processes being considered for Spacelab experiments were studied in this program in order to permit anticipation and understanding of phenomena not ordinarily encountered on earth. Computer calculations were performed on transport processes in floating zone melting and on growth of a crystal from solution in a spacecraft environment. Experiments intended to simulate solution growth at micro accelerations were performed.

Surface-tension driven convection was found to be vigorous in floating zone melting of silicon. It is relatively unaffected by zone movement and by buoyancy effects even at earth's gravity. With very effective heat shielding, a laminar cell resembling a smoke ring is set up in the top half of the zone, and another in the lower half. Mass transfer is slow between these cells. It is also less effective along the center of the zone than at the periphery, leading to a significant radial variation in composition in the resulting crystal, unless very low growth rates are employed. Less effective heat shielding would produce secondary cells in the melt. These would probably become oscillatory and cause compositional striations parallel

to the growth interface. Without heat shielding the convection would almost certainly be turbulent. Turbulence would result in a fairly uniform composition radially, but would cause very fine compositional striations, probably on a scale too small to be detected by ordinary means. Electrical and optical properties would probably be degraded, however. In good thermal conductors, the surface driven convection has only a small effect on heat transfer. In poor thermal conductors, the influence is large. As a consequence, one might expect a twitching or oscillatory convection at the melt surface when a poor conductor is heated by radiation along the entire melt.

Both our transient numerical calculations and previous steady state theory predict that a vortex-like ring should be established about a suspended sphere slowly growing from a solution at low  $g$ . However our low  $g$  simulation experiments produce a stream which separates from the sphere and meanders about the solution, only slowly mixing in. The solution soon became very inhomogeneous. The convection was insensitive to mechanical perturbations. These results are to be contrasted with the usual solution-growth system in which the solution density depends strongly on composition. The stream which separates from the crystal in this case rapidly mixes with the bulk solution. Small mechanical perturbations produce "explosions" in this convection--a sudden increase in convection, with turbulent eddies, which then decrease again to steady state. Perhaps the most encouraging result was that inclusion-free faceted crystals were produced under simulated low  $g$  conditions.

Two papers on this work were delivered at the May 17 San Diego meeting of the Western Section of the American Association of Crystal Growth. A talk on the floating zone studies was given at the June 1974 meeting of the American Institute of Chemical Engineers in Pittsburgh. One paper (J. Crystal Growth 21 (1974) 182) was published and three others are in preparation.

## TABLE OF CONTENTS

Abstract . . . . .	ii
List of Illustrations . . . . .	vii
List of Tables . . . . .	xi
Summary . . . . .	xii
 I. INTRODUCTION . . . . .	 1
II. SURFACE TENSION DRIVEN FLOW IN FLOATING ZONE MELTING AT ZERO G . . . . .	 4
A. Introduction . . . . .	7
B. Model . . . . .	9
C. Streamlines for a Parabolic Temperature Profile at the Free Melt Surface (Radiation Heating) . . . . .	15
D. Fluid Flow Coupled with Heat Transfer (Electron Beam Heating) . . . . .	20
E. Influence of Prandtl Number . . . . .	22
F. Influence of Zone Travel on Hydrodynamics . . . . .	27
G. Impurity Segregation . . . . .	34
H. Constitutional Supercooling . . . . .	38
I. Influence of Gravity on Flow . . . . .	41
J. Influence of Thermal Environment on Isotherms . . . . .	41
K. Influence of Materials Parameters . . . . .	43
 III. TRANSIENT FREE CONVECTION AT LOW G ABOUT A SUSPENDED CRYSTAL . . . . .	 50
A. Introduction . . . . .	52
B. Model . . . . .	52
C. Convection-Free Mass Transfer (Diffusion) . . . . .	53
D. Convective Mass Transfer . . . . .	55
 IV. EXPERIMENTAL SIMULATION OF CRYSTALLIZATION IN A LOW G SPACECRAFT ENVIRONMENT . . . . .	 64
A. Purpose and Scope . . . . .	65
B. Low-Gravity-Simulation Systems . . . . .	67
C. Preparation and Characterization of Solutions . . . . .	81
D. Preparation of Crystals and Polycrystalline Spheres . . . . .	86
E. Optical and Photographic Apparatus . . . . .	89
F. Experimental Results . . . . .	98
G. Conclusions and Future Plans . . . . .	106

TABLE OF CONTENTS (Continued)

V. FUTURE . . . . .	111
References . . . . .	113
References - Appendix A . . . . .	114
APPENDIX A - ANALYSIS OF SURFACE DRIVEN FLOW IN FLOATING ZONE MELTING . . . . .	115
A. Dimensional Equations . . . . .	115
B. Dimensionless Equations . . . . .	120
C. Computation . . . . .	128
APPENDIX B - ANALYSIS OF FREE CONVECTION ABOUT A SPHERE . . . . .	131
A. Dimensionless Equations . . . . .	131
B. Method of Solution . . . . .	135

# LIST OF ILLUSTRATIONS

Figure 1.	Floating zone melting, geometry, coordinate system and fluid velocity components . . . . .	8
Figure 2.	Streamlines for $M' = 35$ with parabolic temperature profile along melt surface . . . . .	16
Figure 3.	Streamlines for $M' = 350$ . . . . .	17
Figure 4.	Streamlines for $M' = 3500$ . . . . .	18
Figure 5.	Streamlines for $M' = 7000$ . . . . .	19
Figure 6.	Streamlines for $M' = 35$ and $Pr = 0.023$ with electron beam heating . . . . .	21
Figure 7.	Streamlines for $M' = 350$ and $Pr = 0.023$ with electron beam heating . . . . .	23
Figure 8.	Influence of convection on isotherms for $M' = 350$ and $Pr = 0.023$ . . . . .	24
Figure 9.	Vorticity field for $M' = 350$ and $Pr = 0.023$ . . . . .	25
Figure 10.	Influence of Prandtl number and heating method on melt-surface temperature-profile . . . . .	26
Figure 11.	Isotherms and streamlines for $M' = 350$ and $Pr = 0.3$ with electron-beam heating . . . . .	28
Figure 12.	Isotherms and streamlines for $M' = 350$ and $Pr = 2$ . . . . .	29
Figure 13.	Influence of a zone travel rate of 10 cm/hour on streamlines for $M' = 35$ and $Pr = 0.023$ . . . . .	30
Figure 14.	Influence of zone travel rate of 30 cm/hour on streamlines $M' = 35$ and $Pr = 0.023$ . . . . .	31
Figure 15.	Influence of zone travel rate of 50 cm/hour on streamlines . . . . .	32
Figure 16.	Zone travel rate of 70 cm/hour . . . . .	33
Figure 17.	Concentration field for zone travel rate of 1 cm/hour, $M' = 350$ , $Pr = 0.023$ , $Sc = 5.0$ , and interfacial distribution coefficient of 0.1 . . . . .	35

# LIST OF ILLUSTRATIONS (Continued)

Figure 18.	Concentration field for 5 cm/hour zone travel rate . . . . .	36
Figure 19.	Axial concentration profiles at three radial positions for zone travel rates of 1 and 5 cm/hour . . . . .	37
Figure 20.	Impurity concentration profiles in resulting crystal . . . . .	39
Figure 21.	Dependence on radial position of interfacial temperature gradient and impurity concentration gradient . . . . .	40
Figure 22.	Isotherms and streamlines for acceleration of ten times earth's gravity for $M' = 350$ with properties of silicon . . . . .	42
Figure 23.	Conduction isotherms for electron beam heating of silicon with radiation to room temperature . . . . .	44
Figure 24.	Conduction isotherms for silicon with the end of the solid perfectly insulated . . . . .	45
Figure 25.	Conduction isotherms for silicon with the end of the solid at room temperature . . . . .	46
Figure 26.	Influence of convection on the isotherms . . . . .	47
Figure 27.	Concentration profiles for transient diffusion from sphere into infinite body of solution . . . . .	54
Figure 28.	Sherwood number for transient diffusion from sphere . . . . .	56
Figure 29.	Streamlines for flow a short time after initiation of growth on dissolution of a sphere . . . . .	57
Figure 30.	Concentration field about sphere . . . . .	58
Figure 31.	Vorticity field about sphere . . . . .	59
Figure 32.	Vorticity as a function of radial and angular positions . . . . .	60
Figure 33.	Tangential velocity about a growing or dissolving sphere . . . . .	61



# LIST OF ILLUSTRATIONS (Continued)

Figure 34.	Radial velocity about a sphere . . . . .	62
Figure 35.	Density versus concentration of three candidate LGS systems . . . . .	80
Figure 36.	Index of refraction of thymol-diethyl carbonate solutions . . . . .	82
Figure 37.	Viscosity of thymol-diethyl carbonate solutions . . . . .	84
Figure 38.	Density of thymol-diethyl carbonate solutions at 23.5°C . . . . .	85
Figure 39.	Original die for making polycrystalline spheres . . . . .	87
Figure 40.	Improved dies for pressing polycrystalline spheres . . . . .	87
Figure 41.	Diagram of Töpler schlieren apparatus . . . . .	90
Figure 42.	Sketch of mirror schlieren apparatus used at USC . . . . .	90
Figure 43.	Alternative schlieren system using mirrors . . . . .	92
Figure 44.	Resolution of schlieren system without collimator . . . . .	94
Figure 45.	Resolution of schlieren system with collimator . . . . .	94
Figure 46.	Modes of photography used with schlieren apparatus . . . . .	96
Figure 47.	Successive stages of dissolution of $\text{NH}_4\text{Cl}$ sphere in water . . . . .	101
Figure 48.	Successive stages of dissolution of $\text{NH}_4\text{Cl}$ in 90% solution . . . . .	101
Figure 49.	Frames from movie showing flow about dissolving KBr perturbed by a tap on the container . . . . .	104
Figure 50.	Frames from movie showing irregular flow about dissolving KBr without deliberate perturbations . . . . .	105

LIST OF ILLUSTRATIONS (Continued)

Figure 51.	Frames from movie showing steady plume from thymol dissolving in ethyl carbonate . . . . .	107
Figure 52.	Frames from movie showing meandering plume from thymol dissolving in ethyl carbonate . . . . .	108
Figure A-1.	Mass transfer fluxes in zone melting . . . . .	119
Figure A-2.	Grid system and computational molecules for finite difference solution . . . . .	129
Figure B-1.	Coordinate system for spherical solution growth . . . . .	131
Figure B-2.	Resolution of acceleration into angular and radial components . . . . .	132

# LIST OF TABLES

Table I.	Summary of the dependence of streamlines on surface tension . . . . .	11
Table II.	Some properties of liquids near melting point . . . . .	49
Table III.	Suitable solvents and solutes tabulated according to density . . . . .	75
Table IV.	Unacceptable LGS systems and reasons for rejection . . . . .	79
Table V.	Possible acceptable LGS systems . . . . .	79
Table VI.	Summary of growth and dissolution experiments . . . . .	99

## SUMMARY

Surface-tension driven convection in floating zone melting was studied by computer solution of the partial differential equations for steady-state momentum, heat and mass transfer. Finite difference methods were employed. Two situations were investigated-- a parabolic temperature profile along the melt surface, as might result from radiant heating; and a line heat source as with electron beam heating. Although the calculations were performed using dimensionless parameters, the conclusions below are expressed in terms of a 1 cm diameter x 1 cm long molten zone of silicon, except where noted.

1. The flow patterns for both methods of heating are similar, but with radiant heating the highest fluid velocities are at the melt periphery near the crystal interface, and with electron beam heating producing the highest velocities near the middle of the zone.

2. For a temperature difference of  $0.005^{\circ}\text{C}$  between the interface and the middle of the zone at the periphery, a single roll cell is formed in the top half of the zone, with its mirror image in the bottom half. The maximum melt velocity is about 3 cm/min. Such a small temperature difference could only be produced by use of very effective heat shields or after-heaters.

3. At about  $0.1^{\circ}\text{C}$  temperature difference, secondary cells are produced. Although our steady state calculations could not show it, we suspect that the flow would become oscillatory and eventually

turbulent as this temperature difference is increased (by reducing the heat shielding).

4. For good thermal conductors such as silicon, the fluid motion has little influence on heat transfer and interface position. The reverse is true for poor conductors.

5. Normal zone travel rates have little influence on the surface-driven flow. For example, with a temperature difference of  $0.005^{\circ}\text{C}$ , a zone travel rate of 10 cm/hour noticeably perturbs the streamlines only in the vicinity of the solid-liquid interfaces.

6. At small temperature gradients, the primary resistance to mass transfer is in the middle of the zone, unlike boundary layer flow in which the mass transfer resistance is concentrated near the solid-liquid interfaces.

7. Significant radial inhomogeneities in the resulting crystal would be expected when the convection is relatively slow. For example, a 10% radial variation would result from a zone travel rate of 1 cm/hour, a distribution coefficient of 0.1, and a temperature difference of  $0.05^{\circ}\text{C}$  along the melt surface. At 4 cm/hour zone travel rate there would be a 40% impurity concentration gradient.

8. Buoyancy-driven flow at earth's gravity is negligible compared to surface driven flow for molten silicon.

9. The vigor of surface driven flow varies considerably from material to material, increasing as the dependence of surface tension on temperature increases, as density increases, and as the viscosity of the melt decreases. Since temperature gradients generally increase

as thermal conductivity decreases, one would also expect poor thermal conductors to have greater surface driven flow, other properties being equal.

Theoretical predictions for solution growth at low accelerations are:

1. The flow will not be of the boundary-layer type. The perturbed region will extend into the solution for distances on the order of the crystal size.

2. Long times will be required for convection to influence the mass transfer and for steady state to be reached.

Several solute-solvent systems have been found which have a density only weakly dependent on composition. These are useful for simulation of low acceleration solution growth and dissolution because they yield Grashof ( $Gr$ ) numbers on earth of the same magnitude as for normal crystal growth systems in a space laboratory. Optical and photographic techniques have been developed for studying growth and dissolution. Preliminary experiments have revealed that:

1. High quality crystals can be grown from solution under low Grashof ( $Gr$ ) number conditions, as exemplified by thymol growing from ethyl carbonate solutions.

2. At low  $Gr$  the stream formed during dissolution mixes much more slowly with the bulk solution than at high  $Gr$ .

3. The convective flow pattern at low  $Gr$  is much less sensitive to perturbations than at high  $Gr$ .

The calculational portions of this program have ended, pending additional funding. The experiments will continue with present funds until December.

## I. INTRODUCTION

This program consisted of three parts:

1. Computer calculations of surface tension driven flow in floating zone melting at zero g.
2. Computer calculations of transient free convection about a suspended sphere at very low g.
3. Experimental simulation of solution crystal growth in a space environment.

Part 1 was initiated in late June 1973, Part 2 in August 1973 and Part 3 in December 1973. Without additional funding, Parts 1 and 2 have ended.

One of the most promising space processing applications is floating zone melting. On earth the crystal diameter that can be produced is limited by the size of the zone that can be supported by the surface tension of the melt in opposition to gravity. In space any size could be produced. For many materials the space vacuum could advantageously be utilized as an environment for the float zoning. While the absence of earth's gravity assures that buoyancy-driven free convection will be negligible in space, one must not assume that there will be no convection in the zone. Since the temperature will vary along the gas-melt surface of the zone, the surface tension will vary along the surface of the zone, normally increasing as one moves from



the center toward the solid. This surface tension gradient will develop a flow field, as the system tries to minimize its surface energy via movement of the melt surface from low surface tension regions to high surface tension regions. The question is, how vigorous is this flow and what influence does it have on the crystal growth? One cannot do experiments on earth because of interference with buoyancy effects. Even in space only limited experiments could be done on opaque materials such as silicon. However, the governing differential equations can be solved on earth to provide a fairly complete picture of surface-driven flow phenomenon. We have solved some of the interesting problems here.

Before beginning this program there was some concern on our part about the advisability of growing crystals from solution in space, because of the great tendency to occlude solution during growth. However, our experiments have shown that inclusion-free faceted crystals can be produced in a low-convection environment. Since there will be some acceleration in Spacelab, free convection will not be completely absent. The convection will probably not be steady state, however, because of the long transients predicted and the variation in acceleration in an orbiting laboratory. Our objective is to determine the convection patterns to be expected and their influence on crystal growth phenomena. Both simulation experiments and transport calculations have been performed. Solutions with a density nearly independent of composition are required for the experiments.

Each of the following three sections of this report covers one of the parts described above. These sections are independent of one another so that it is not necessary to read one section in order to understand another. Possible future research is discussed in the final section.

## II. SURFACE TENSION DRIVEN FLOW IN FLOATING ZONE MELTING AT ZERO G

(Chong E. Chang)

### Definition of Symbols

$a$	Radius of the molten zone, cm
$b$	Distance of the top surface of the solid from the center of the zone, cm
$c_p$	Specific heat, cal/g <sup>o</sup> K
$C$	Dimensionless impurity concentration in the liquid, defined by $m/m_t$
$C_{ct}$	Dimensionless impurity concentration in the feed crystal, defined by $m_{ct}/m_t$
$C_{i,b}$	Dimensionless impurity concentration in the liquid at the crystallizing interface, defined by $m_{i,b}/m_t$
$C_{i,t}$	Dimensionless impurity concentration in the liquid at the melting interface, defined by $m_{i,t}/m_t$
$D$	Binary molecular diffusion coefficient, cm <sup>2</sup> /sec
$g$	Acceleration, cm/sec <sup>2</sup>
$g_e$	Earth's gravitational field, 980 cm/sec <sup>2</sup>
$Gr_h$	Grashof number for heat transfer (~ ratio of the temperature difference buoyancy force to the viscous force) defined by $g\beta(T_o - T_m)a^3/\nu^2$
$Gr_m$	Grashof number for mass transfer (~ ratio of the composition buoyancy force to the viscous force) defined by $g\alpha m_t a^3/\nu^2$
$i$	Integer denoting grid station in axial direction, $i = 1, 2, 3, \dots$
$j$	Integer denoting grid station in radial direction, $j = 1, 2, 3, \dots$
$k$	Thermal conductivity, cal/cm sec <sup>o</sup> C

$k_o$	Interfacial distribution coefficient (ratio of the impurity concentration in the crystal to that in the liquid at the interface)
$l$	One half of the liquid zone length, cm
$m$	Impurity concentration in liquid, g/cm <sup>3</sup>
$m_t$	Impurity concentration the feed solid would have if it were melted, g/cm <sup>3</sup>
$m_{cb}$	Impurity concentration in the crystal, g/cm <sup>3</sup>
$m_{ct}$	Impurity concentration in the feed crystal, g/cm <sup>3</sup>
$m_{i,b}$	Impurity concentration in the liquid at the crystal-lizing interface, g/cm <sup>3</sup>
$m_{i,t}$	Impurity concentration in the liquid at the melting interface, g/cm <sup>3</sup>
$M'$	Dimensionless surface tension parameter at the free liquid surface (~ ratio of surface tension force to viscous force) defined by $\rho\sigma(T_o - T_m)a/\mu^2$
$Nu$	Nusselt number (dimensionless temperature gradient, or ratio of total heat transport to heat conduction) defined by $ \partial\theta/\partial z _{+l/a}$
$p$	Dynamic pressure in fluid, dyne/cm <sup>2</sup> , $P - p_o$
$p_o$	Static pressure in fluid, dyne/cm <sup>2</sup> , defined by $\rho_f g(l - z)$
$P$	Total pressure in fluid, dyne/cm <sup>2</sup>
$Pr$	Prandtl number, $\mu C_p/k$ (ratio of the momentum diffusivity to the thermal diffusivity)
$r$	Radial coordinate, measured from the center of the zone, cm
$R$	Dimensionless radial coordinate, measured from the center of the zone, $r/a$
$\Delta R$	Dimensionless radial distance between grid points;
$Sc$	Schmidt number (ratio of the momentum diffusivity to the molecular diffusion coefficient), $\mu/\rho D$

Sh	Sherwood number (dimensionless concentration gradient), defined by $ \partial C/\partial z _{+l/a}$
T	Temperature, $^{\circ}\text{K}$
$T_o$	Temperature of the middle of liquid zone at the periphery, $^{\circ}\text{K}$
$T_c$	Temperature of the surroundings, $^{\circ}\text{K}$
$T_m$	Interfacial temperature (melting point), $^{\circ}\text{K}$
$\Delta T$	Either $(T_o - T_m)$ if $\theta$ is defined by the Equation (A-19) or $(T_m - T_c)$ if $\theta$ is defined by the Equation (A-31), $^{\circ}\text{K}$
$v_c$	Zone travel rate, cm/sec
$v_r$	Radial velocity component of the fluid, cm/sec
$v_z$	Axial velocity component of the fluid, cm/sec
$V_c$	Dimensionless zone travel rate, $v_c a/v$
$V_r$	Dimensionless radial velocity component of the fluid, $v_r a/v$
$V_z$	Dimensionless axial velocity component of the fluid, $v_z a/v$
$V_{cf}$	Dimensionless interfacial flow rate, $V_c (\rho_c/\rho_f)$
z	Axial coordinate, measured from the center of the zone, cm
Z	Dimensionless axial coordinate, measured from the center of the zone, $z/a$
$\Delta Z$	Dimensionless axial distance between grid points
$\alpha$	$(\partial \rho/\partial m)_{T,P}/\rho$ ; volume expansion coefficient due to a concentration change in fluid, $1/(\text{g}/\text{cm}^3)$
$\beta$	$(\partial \rho/\partial T)_{m,P}/\rho$ ; volume expansion coefficient due to a temperature change in fluid, $1/^{\circ}\text{C}$
$\gamma$	Surface tension between melt and vapor, dyne/cm
$\epsilon_s$	Emissivity of thermal radiation

$\theta$	Dimensionless temperature, $(T-T_m)/\Delta T$
$\theta_c$	Dimensionless temperature of the surroundings, $(T_c-T_m)/\Delta T$
$\mu$	Viscosity of the fluid, g/cm sec
$\nu$	Kinematic viscosity, $\mu/\rho$ , cm <sup>2</sup> /sec
$\rho$	Density of the fluid, g/cm <sup>3</sup>
$\rho_c$	Density of the crystal, g/cm <sup>3</sup>
$\rho_f$	Density of the fluid at melting point, g/cm <sup>3</sup>
$\sigma$	Stefan-Boltzmann constant, $5.668 \times 10^{-5}$ erg/cm <sup>2</sup> sec °K <sup>4</sup>
$\sigma$	Temperature coefficient of the surface tension, $\partial\gamma/\partial T$ , dynes/cm °K
$\psi$	Dimensionless stream function, defined by Equations (A-25) and (A-26) in Appendix A.
$\omega$	Dimensionless vorticity, defined by Equations (A-21) and (A-27) in Appendix A.

#### A. Introduction

Floating zone melting (1) is a common method of growing single crystals, especially for high melting materials because the melt is not in contact with a crucible. Although free convection due to density variations will not occur at zero g, temperature variations along the free melt surface will cause surface tension variations which generate convection. Surface-driven flow is often called the "Marangoni effect".

We consider a liquid zone suspended between two cylindrical solids by its own surface tension, as in Figure 1. Both the solid and the liquid are surrounded by a gas or vacuum. The liquid zone is

generated by a power source, typically a radiant heater, an electron beam, or by induction from a high frequency coil. (Induction heating is generally considered too inefficient and bulky to be employed for space processing, although it is used extensively on earth for conductors.) The zone is made to move by slowly moving the heater,

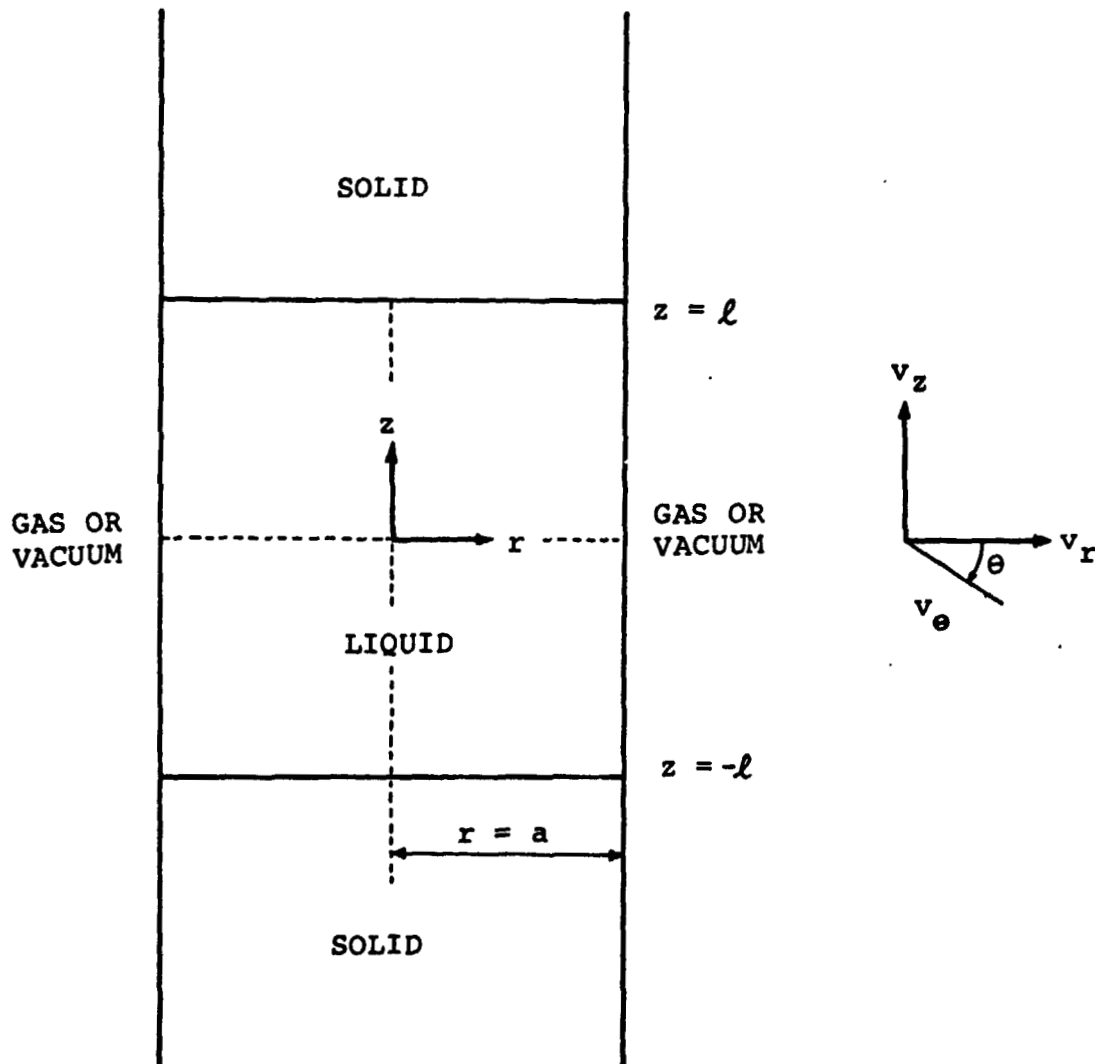


Figure 1. Floating Zone Melting, Geometry, Coordinate System and Fluid Velocity Components

resulting in continuous solidification at one liquid/solid interface and melting at the other. In order to determine the influence of surface driven flow on zero melting, the partial differential equations for momentum and heat transfer were considered. These are shown in the appendix. Solutions were obtained numerically using the computer for two situations--a parabolic temperature profile along the melt-vapor surface and for a ring heat source at the center of the zone. The parabolic profile corresponds approximately to radiant heating, and the ring source corresponds to electron beam heating. The mass transfer equation coupled with the computed flow fields were employed to find the impurity concentration fields in the melt and in the growing crystal at steady state. Most of the calculations were done for a 1 cm diameter silicon rod, although the results are expressed in dimensionless form so that they also represent other possibilities.

#### B. Model

The coordinate system and geometry are shown schematically in Figure 1. The change in modes of heating can be easily taken into account by simply changing the thermal boundary conditions. Since we consider only steady state, the Eulerian specification of the flow field seems to be convenient. That is, the interfaces and heater are taken to be fixed so that material continuously moves through the zone and the heater. This is equivalent to suction at the freezing interface and blowing at the melting interface (4).



Assumptions used in the analysis are as follows:

- a) Axisymmetrical flow; i.e., no angular components. (Violated if crystal rotated or if flow is not steady.)
- b) Incompressible liquid. (Variation of  $\rho$  negligible.)
- c) Constant properties of the liquid zone, i.e.,  $\rho$ ,  $\mu$ ,  $k$ ,  $D$ ,  $c_p$ ,  $\epsilon$ , all constant.
- d) Planar liquid/solid interfaces.
- e) Shape of the liquid zone is circular cylinder.
- f) Symmetrical heating of the zone.
- g) Negligible viscous dissipation (low Mach number).
- h) Steady state.
- i) Growth and melting interface kinetics are sufficiently rapid that the liquid/solid interfaces are at the melting point of the material.
- j) Constant distribution coefficient  $k_0$ .

The mass conservation, Navier-Stokes, mass transfer equations, and boundary conditions are given in Appendix A, along with a description of the methods of solution. Silicon was taken as a model material for numerical calculation of flow, temperature, and impurity (dopant) concentration fields. For silicon, the melting point is  $1410^\circ\text{C}$ , the Prandtl number is 0.023, the Schmidt number is about 5,  $M'/a(T_0 - T_m) = \rho\sigma/\mu^2$  is 14,000, and the emissivity is assumed to be 0.3 for both the melt and the solid.

Results of the calculations are summarized in Table I.

TABLE I. SUMMARY OF THE DEPENDENCE OF STREAMLINES ON SURFACE TENSION PARAMETER

$M' = \rho \sigma (T_o - T_m) a / \mu^2$ ,    PRANTL NUMBER  $Pr = \mu c_p / k$ ,  
 FREEZING RATE  $v_c$ , AND GRASHOF NUMBER  $Gr_h = g \beta (T_o - T_m) a^3 / \nu^2$   
 FOR AN ASPECT RATIO  $(a/l)$  OF ONE

NO	M'	Gr <sub>h</sub>	v <sub>c</sub> (cm/hr)	Pr	Grid Points Used	Maximum Dimensionless Velocity Component of Fluid and its Location	Maximum Vorticity and its Location	Vortex Centers, Location and Direction of Rotation				Vortex Symmetrical about
								(+ for clockwise (-) for counterclockwise				
								1st	2nd	3rd	4th	
Heating Method: Parabolic T Profile												
1	35	0	0	0.023	11x11	V =5.8 Z=0.7 R=1	ω=212 Z=1 R=0.9	(-) Z=0.65 R=0.81				R and Z axis
2	350	0	0	0.023	11x11	V =62.3 Z=0.7 R=1	ω=2,352 Z=1 R=0.9	(-) Z=0.7 R=0.83				R and Z axis
3	3,500	0	0	0.023	21x21	V =219 Z=0.85 R=1	ω=15,510 Z=1 R=0.9	(-) Z=0.86 R=0.79	(+ Z=0.34 R=0.50			R and Z axis
4	7,000	0	0	0.023	41x41	V =275 Z=0.9 R=1	ω=28,850 Z=1 R=0.95	(-) Z=0.88 R=0.92	(+) Z=0.63 R=0.72	(-) Z=0.65 R=0.52	(+) Z=0.62 R=0.35	R and Z axis
Heating Method: Ring Heat Source												
5	350	0	0	0.023	11x11	V =77 Z=0 R=0.9	ω=2,402 Z=0.1 R=0.9	(-) Z=0.1 R=0.9	(-) Z=0.48 R=0.79			R and Z axis

(Continued)

TABLE I. (Continued)

No	M'	Gr <sub>h</sub>	v <sub>c</sub> (cm/hr)	Pr	Grid Points Used	Maximum Dimensionless Velocity Component of Fluid and its Location	Maximum Vorticity and its Location	Vortex Centers, Location and Direction of Rotation				Vortex Symmetrical about
								(-) for counterclockwise				
								1st	2nd	3rd	4th	
Heating Method: Ring Heat Source												
6	350	0	1 to 5	0.023	11x11	Almost the same as the case of No. 5						
7	350	0	1	0.30	11x11		V <sub>r</sub> = 67 Z = 0 R = 0.9	ω = 2,091 Z = 0.1 R = 0.9	(-) Z = 0.1 R = 0.9	(-) Z = 0.7 R = 0.8	R and Z axis	
8	350	0	1	2.0	11x11	V <sub>r</sub> = 92 Z = 0 R = 0.9	ω = 3,192 Z = 0.1 R = 0.9	(-) Z = 0.1 R = 0.9	(-) Z = 0.9 R = 0.88	R and Z axis		
9	35	0	0	0.023	11x11	V <sub>r</sub> = 9.7 Z = 0 R = 0.9	ω = 265 Z = 0.1 R = 0.9	(-) Z = 0.1 R = 0.89		R and Z axis		
10	35	0	10	0.023	11x11	V <sub>r</sub> = 9.6 Z = 0 R = 0.9	ω = 266 Z = 0.1 R = 0.9	(-) Z = 0.1 R = 0.9	(+) Z = -0.1 R = 0.9	Z axis		

(Continued)

TABLE I. (Continued)

No	M'	Gr <sub>h</sub>	v <sub>c</sub> (cm/hr)	Pr	Grid Points Used	Maximum Dimensionless Velocity Component Of Fluid and its Location	Maximum Vorticity and its Location	Vortex Centers, Location and Direction of Rotation				Vortex Symmetrical about		
								(-) for counterclockwise (+) for clockwise						
								1st	2nd	3rd	4th			
Heating Method: Ring Heat Source														
11	35	0	30	0.023	11x11	V <sub>r</sub> =9.7 Z=0  R=0.9	ω=266 Z=0.1  R=0.9	(-) Z=0.1 R=0.9 (+) Z=-0.3 R=0.7					Z axis	
12	35	0	50	0.023	11x11	V <sub>r</sub> =9.7 Z=0  R=0.9	ω=328 Z=1.0  R=0.9	(-) Z=0.1 R=0.9 (+) Z=-0.34 R=0.62					Z axis	
13	35	0	70	0.023	11x11	V <sub>r</sub> =9.7 Z=0  R=0.9	ω=432 Z=1  R=0.9	(-) Z=0.1 R=0.9 (+) Z=-0.37 R=0.56					Z axis	

(Continued)

TABLE I. (Continued)

No	M'	$Gr_h$	$v_c$ (cm/hr)	Pr	Grid Points Used	Maximum Dimensionless Velocity Component of Fluid and its Location	Maximum Vorticity and its Location	Vortex Centers, Location and Direction of Rotation (+) for clockwise (-) for counterclockwise				Vortex Symmetrical about
								1st	2nd	3rd	4th	
Heating Method: Ring Heat Source												
14	350	77.5*	1	0.023	11x11	Almost the same as No. 5						
15	350	775**	1	0.023	11x11	$V_r = 78$ $Z = 0$	$\omega = 2,374$ $Z = 0.1$	(-) $Z = 0.1$ $R = 0.9$	(-) $Z = 0.3$ $R = 0.77$			Z axis
						$R = 0.9$	$R = 0.9$	(+) $Z = -0.1$ $R = 0.9$	(+) $Z = -0.6$ $R = 0.9$			Z axis

\*  $1 g_e$ \*\*  $10 g_e$

### C. Streamlines for a Parabolic Temperature Profile at the Free Melt Surface (Radiation Heating)

For simplicity, a parabolic temperature profile along the melt surface was assumed for our initial calculations. This enabled us to solve the momentum equations without simultaneously solving the heat transfer equations. A parabolic profile, with a maximum at the center, seems reasonable for radiant heating. The dimensionless surface tension parameter  $M'$  increases as the radius of the zone  $a$  and the temperature variation along the melt surface increases. In Figures 2 through 5, the streamlines for parabolic temperature profiles are shown to illustrate the effect of increased values of  $M'$  (35, 350, 3500 and 7000). Donut-shaped vortex cells were formed. With  $M' = 35$  and 350 only two cells are generated, and the centers of the vortices move closer toward the liquid/solid interfaces as  $M'$  increases, as shown in Figures 2 and 3. With  $M' = 3500$ , however, which corresponds to a condition of  $a = 0.5$  cm and  $(T_o - T_m) = 0.5^\circ\text{C}$  for silicon, secondary vortex cells were induced behind the primary vortex, as shown in Figure 4. As the value of  $M'$  was further increased up to 7000, third and fourth vortices were produced, as shown in Figure 5. These multiple vortices are probably indicative of oscillations and incipient turbulence, which cannot be calculated in a steady state analysis. Oscillations are frequently found with free convection in enclosed cavities between laminar and fully turbulent flow. The maximum velocities for 1 cm diameter silicon with  $(T_o - T_m) = 1.0^\circ\text{C}$  are calculated to be 2 cm/sec.

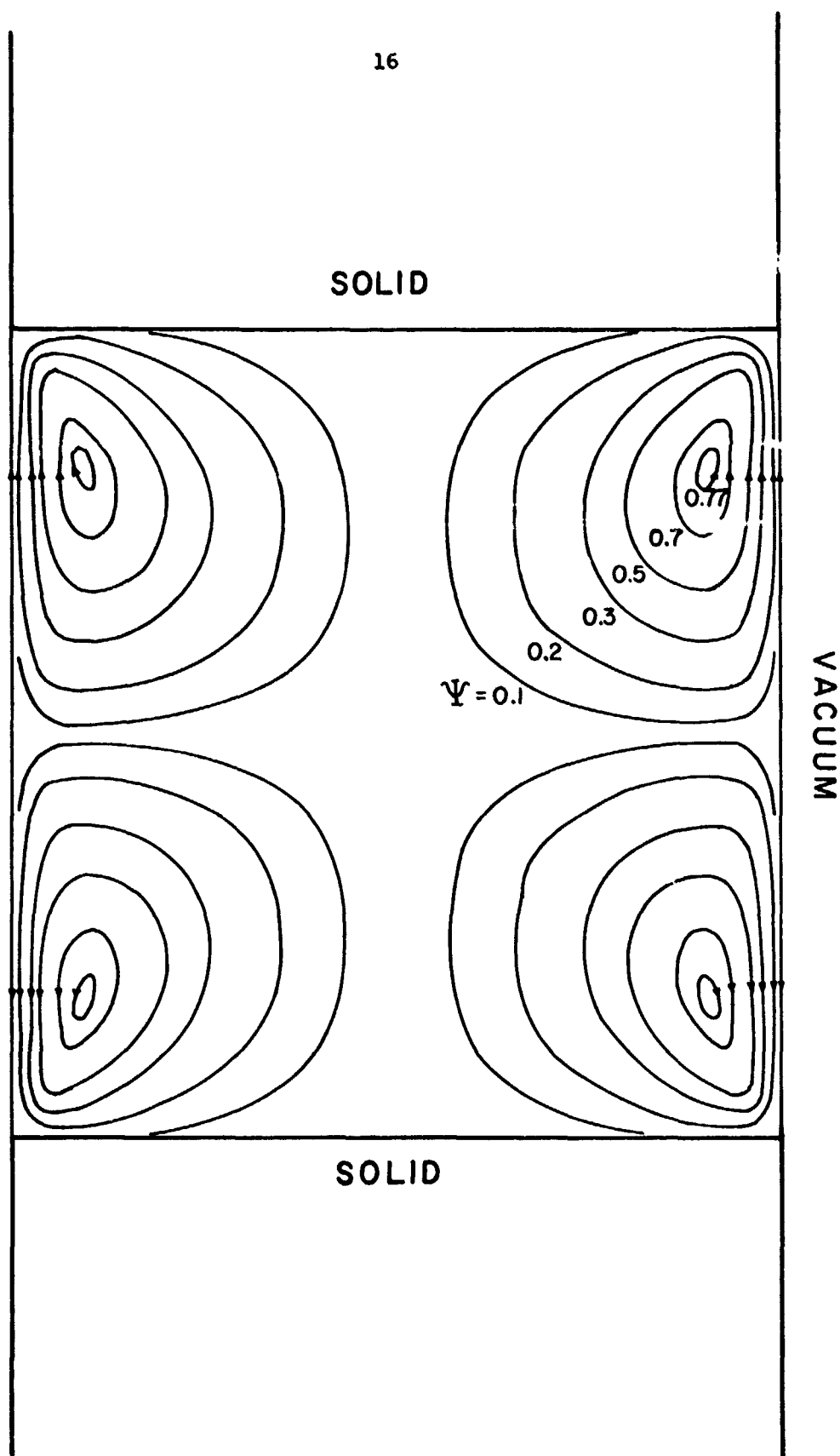


Figure 2. Computed dimensionless streamlines  $\psi$  for surface driven flow in a floating zone at zero gravity with a parabolic temperature profile on the free liquid surface with  $M' = 35$  and  $v_c = 0$ . This would be expected, for example, for silicon with  $(T_o - T_m) = 0.005^\circ\text{C}$  and  $a = 0.5$  cm.

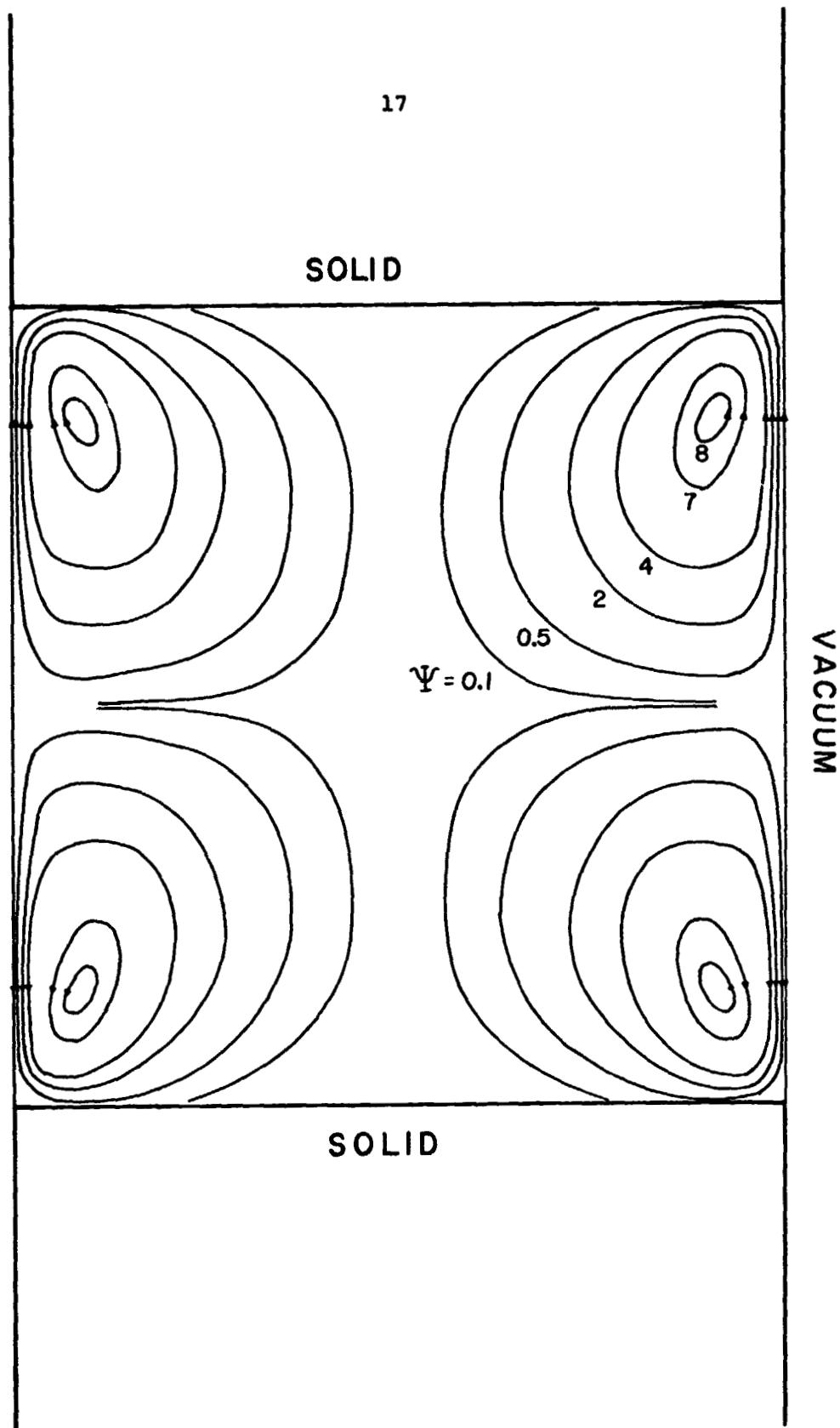


Figure 3. Computed dimensionless streamlines  $\psi$  for surface tension driven flow in a floating zone at zero gravity with a parabolic temperature profile on the free liquid surface with  $M' = 350$  and  $v_c = 0$ . For silicon with  $(T_o - T_m) = 0.05^\circ\text{C}$  and  $a = 0.5$  cm.



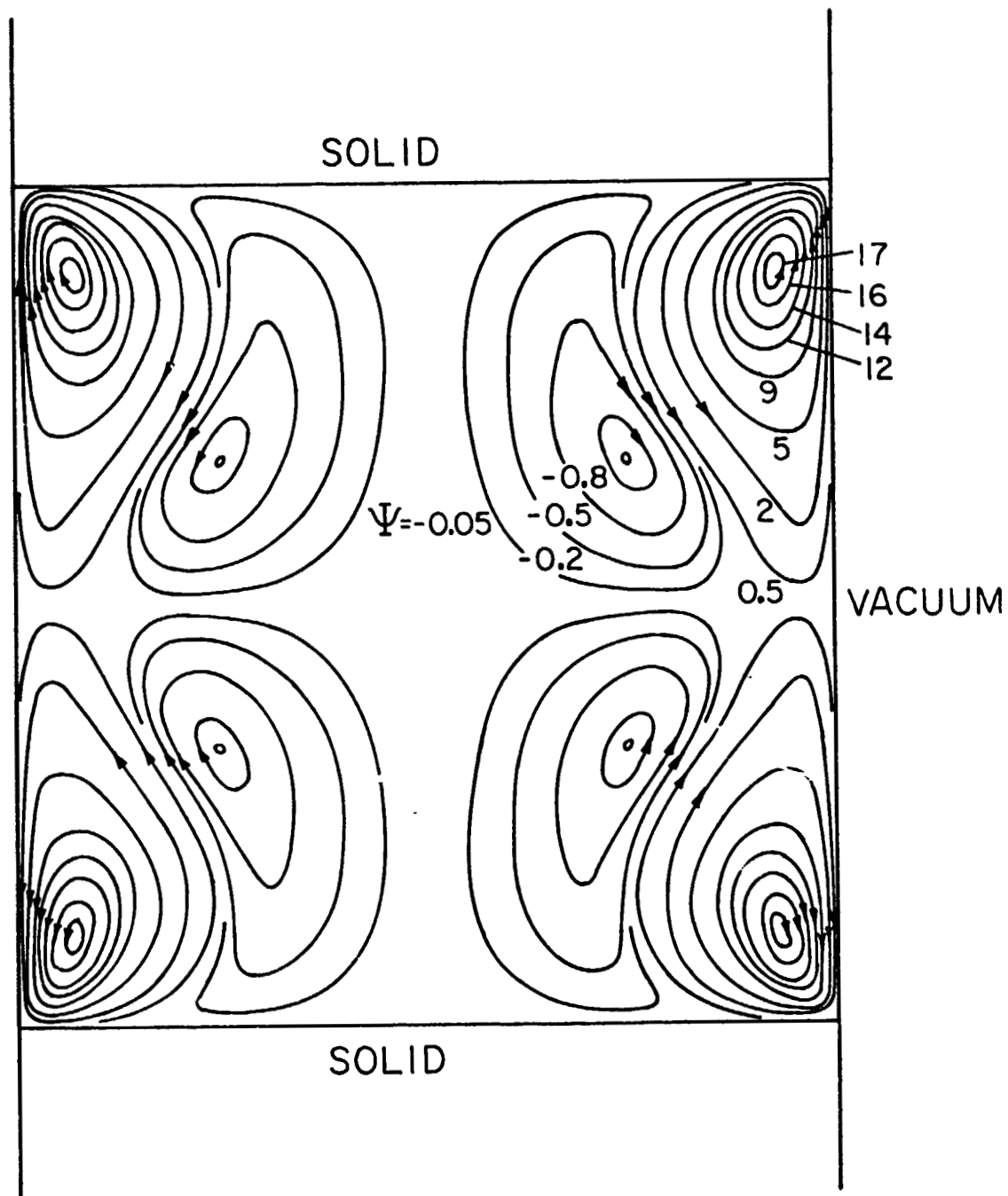


Figure 4. Computed dimensionless streamlines  $\psi$  for surface tension driven flow in a floating zone at zero gravity with a parabolic temperature profile on the free liquid surface with  $M' = 3500$  and  $v_c = 0$ . Silicon with  $(T_o - T_m) = 0.5^\circ\text{C}$  and  $a = 0.5$  cm.

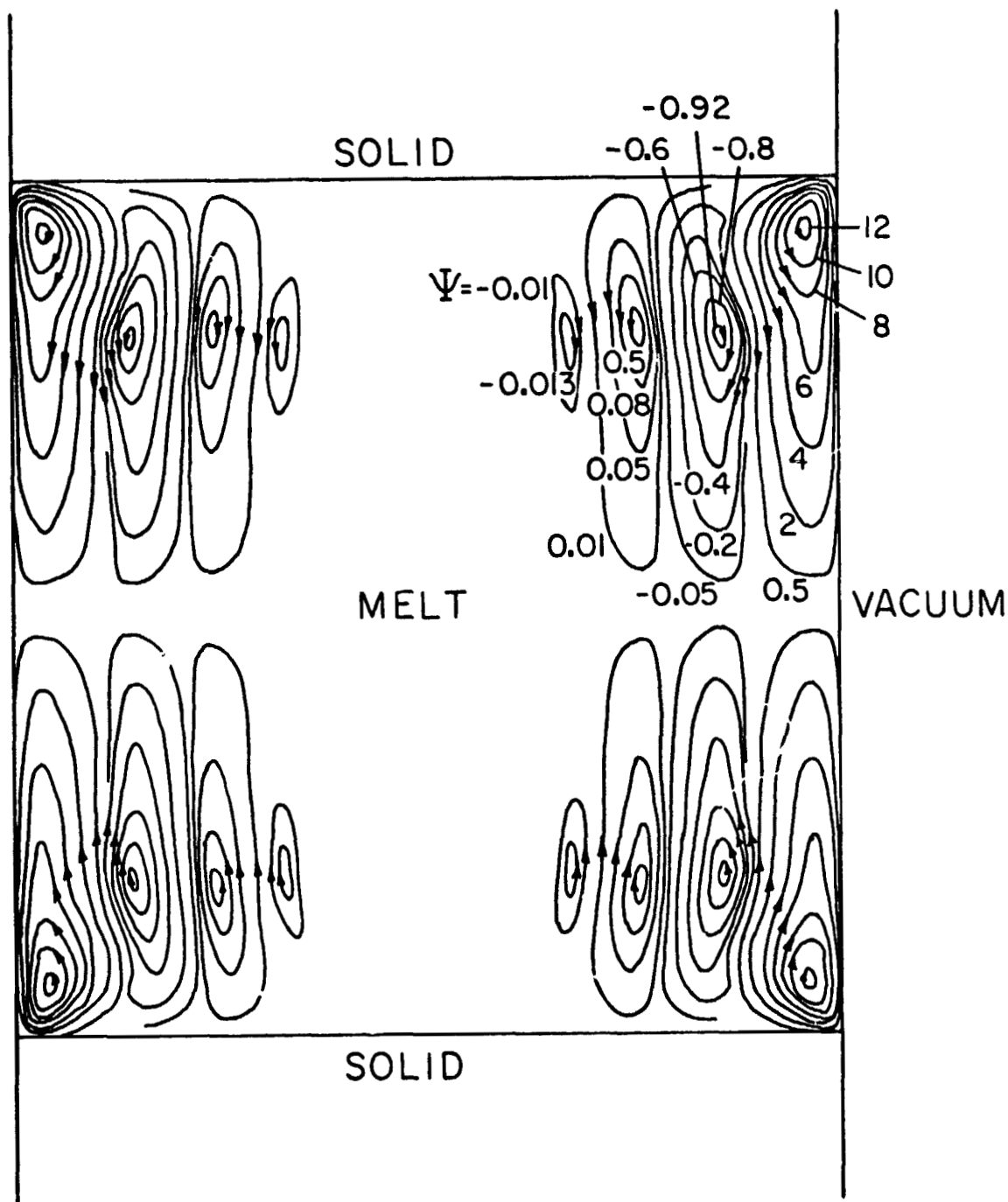


Figure 5. Computed dimensionless streamlines  $\psi$  for surface tension driven flow in a floating zone at zero gravity, with a parabolic temperature profile on the free liquid surface with  $M' = 7000$  and  $v_c = 0$ . Silicon with  $(T_o - T_m) = 1.0^\circ\text{C}$  and  $a = 0.5$  cm.

D. Fluid Flow Coupled with Heat Transfer  
(Electron Beam Heating)

Although a parabolic temperature profile at the free liquid surface may be a reasonable approximation for radiation heating, only a complete heat transfer analysis coupled with flow calculations would provide us with exact temperature profiles. Electron beam heating is commonly used in floating zone melting and was taken as our heating mode. Rather than specify the power input, the circumferential temperature  $T_0$  at the center of the zone was specified for convenience in analysis. The procedure used to solve the coupled heat-momentum transport problem was as follows:

- 1) The temperature field for conduction was computed by neglecting convective heat transfer.
- 2) The surface temperature profile from 1) was utilized to calculate the first approximate solution of fluid flow.
- 3) The temperature field was recalculated using the flow fields from 2).
- 4) Steps 2) and 3) were repeated until the temperature and the fluid flow fields no longer changed appreciably.

The resulting streamlines with  $M' = 35$  are drawn in Figure 6 in which we took values for silicon with the surroundings at the melting point, i.e., the heat shielding about the zone is extremely effective. While this does not correspond exactly with reality, it does show the correct features. Comparing with Figure 2, we see that the vortex centers are shifted nearer to the heat source from the liquid/solid interfaces. This is because the steepest temperature

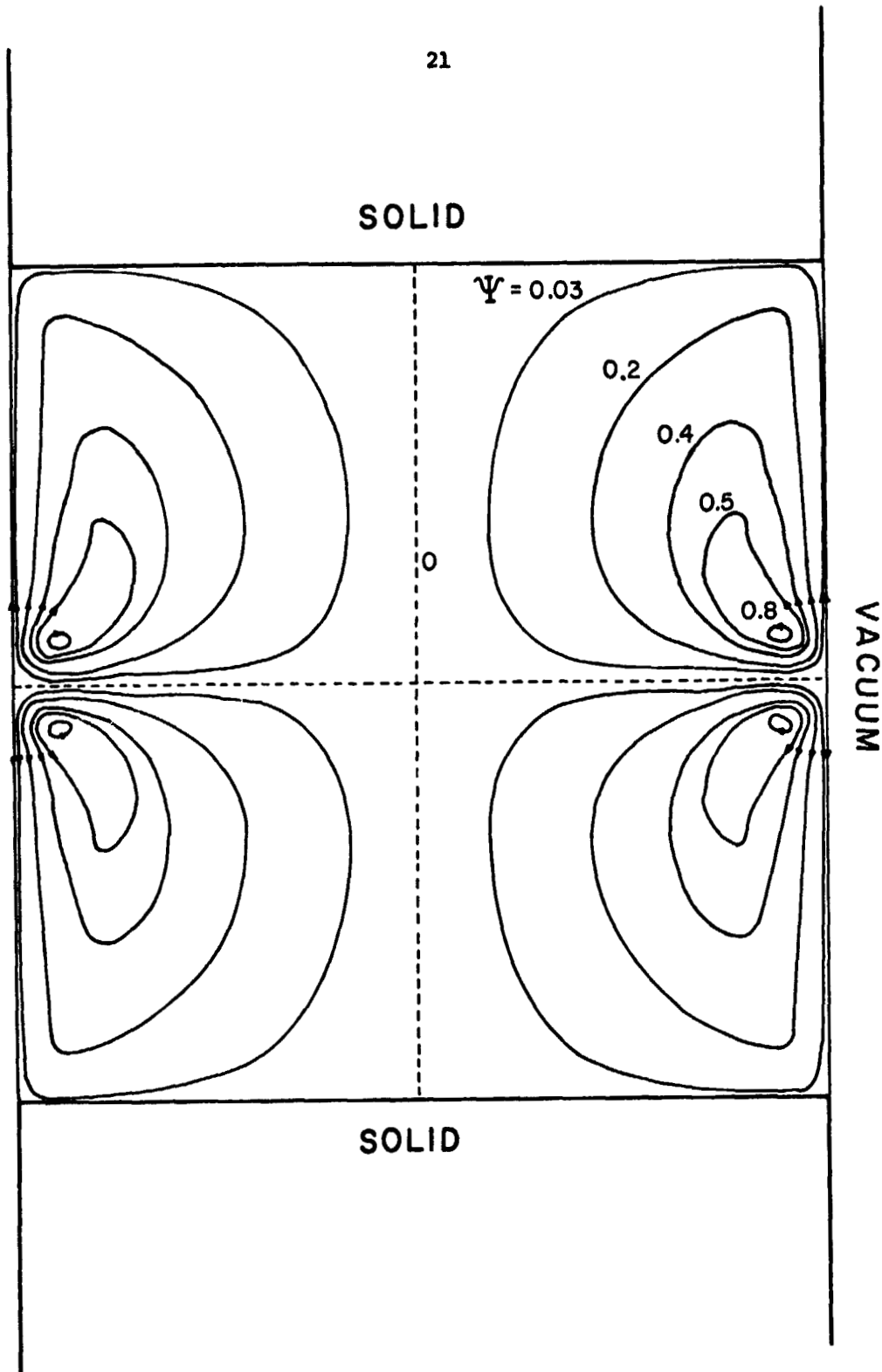


Figure 6. Computed dimensionless streamlines  $\psi$  for surface tension driven flow in a floating zone at zero gravity from the computed temperature fields for electron beam heating of silicon with  $(T_0 - T_m) = 0.005^\circ\text{C}$ ,  $T_c = T_m$ ,  $\epsilon_s = 0.3$ ,  $a = 0.5$  cm,  $M' = 35$ ,  $Pr = 0.023$ , and  $v_c = 0$ .

gradient is at the center of the zone. Further increasing  $M'$  up to 350, by increasing  $(T_o - T_m)$  with other conditions kept constant, resulted in the streamlines and isotherms shown in Figure 7. The maximum velocity for silicon was 0.55 cm/sec. Comparing the temperature fields with surface tension driven flow for  $M' = 350$  with those for pure conduction, there was no significant change except for a slight one near the center of the zone, as shown in Figure 8. This indicates that conduction is much greater than convective heat transfer as would be expected for the small Prandtl number for silicon. (Prandtl number is a measure of the degree to which convection influences heat transfer.) The vorticity fields for  $M' = 350$  as in Figure 7 are shown in Figure 9. The maximum vorticity and its location for various conditions are also summarized in Table I.

#### E. Influence of Prandtl Number

The Prandtl number was increased from 0.023 to 0.3 and 2.0 by increasing the specific heat, and keeping the viscosity and the thermal conductivity of the melt constant. As the Prandtl number increases, the temperature gradients along the free liquid surface (for fixed  $T_o - T_m$ ) increase near the heat source and also near the liquid/solid interfaces, but significantly decrease inbetween, as illustrated in Figure 10. Since the convective heat transfer becomes more significant as a result of increasing the Prandtl number, the isotherms are increasingly distorted from those of pure conduction. This, in turn, causes changes in the flow field. For example, the center of the vortex

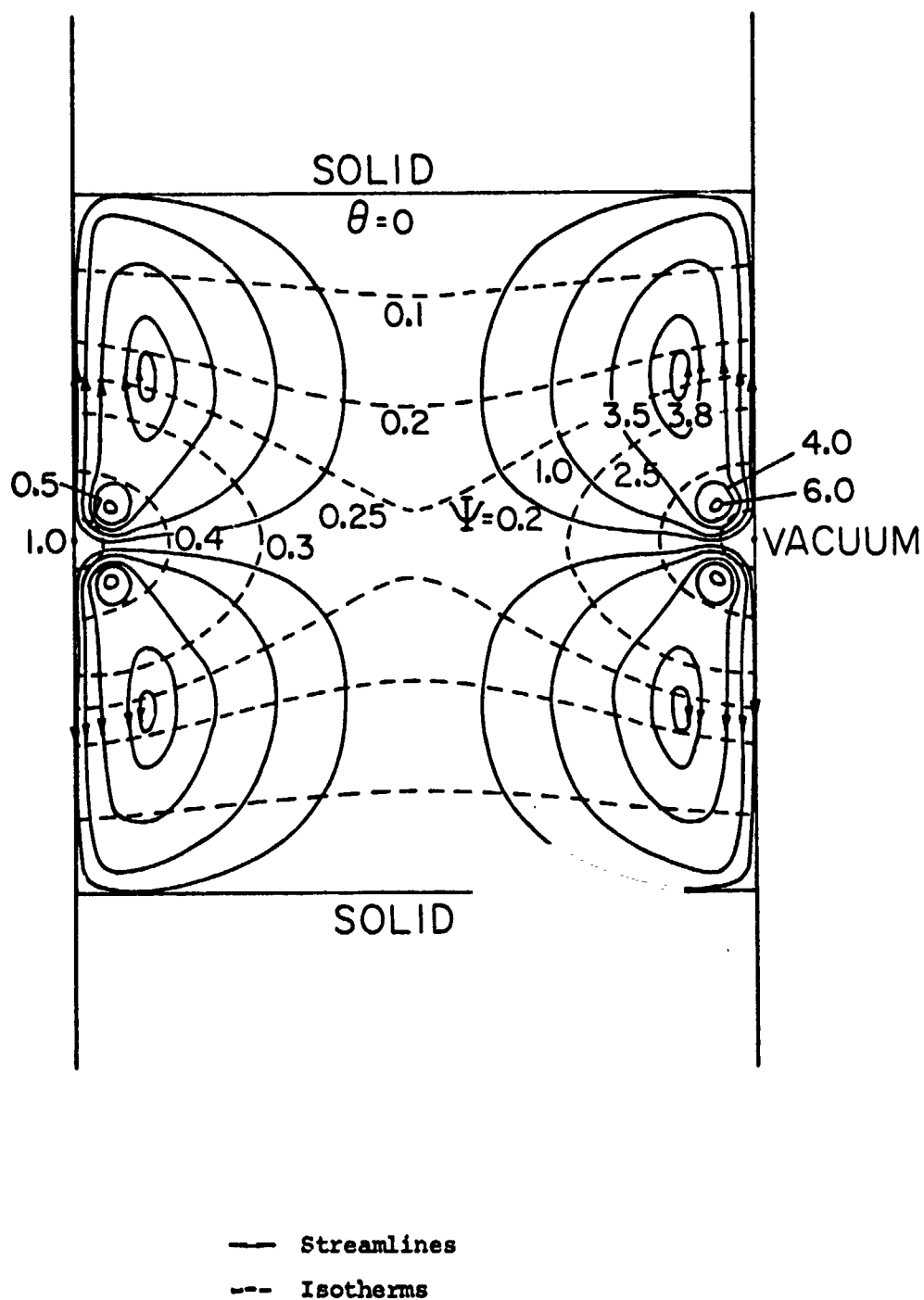


Figure 7. Computer isotherms  $\theta$  and streamlines  $\psi$  for surface tension driven flow in floating zone at zero gravity from the computed temperature fields for electron beam heating of silicon with  $(T_0 - T_m) = 0.05^\circ\text{C}$ ,  $T_c = T_m$ ,  $\epsilon_s = 0.3$ ,  $a = 0.5$  cm,  $M' = 350$ ,  $Pr = 0.023$ ,  $v_c = 0$  and  $\theta = (T - T_m)/(T_0 - T_m)$ .

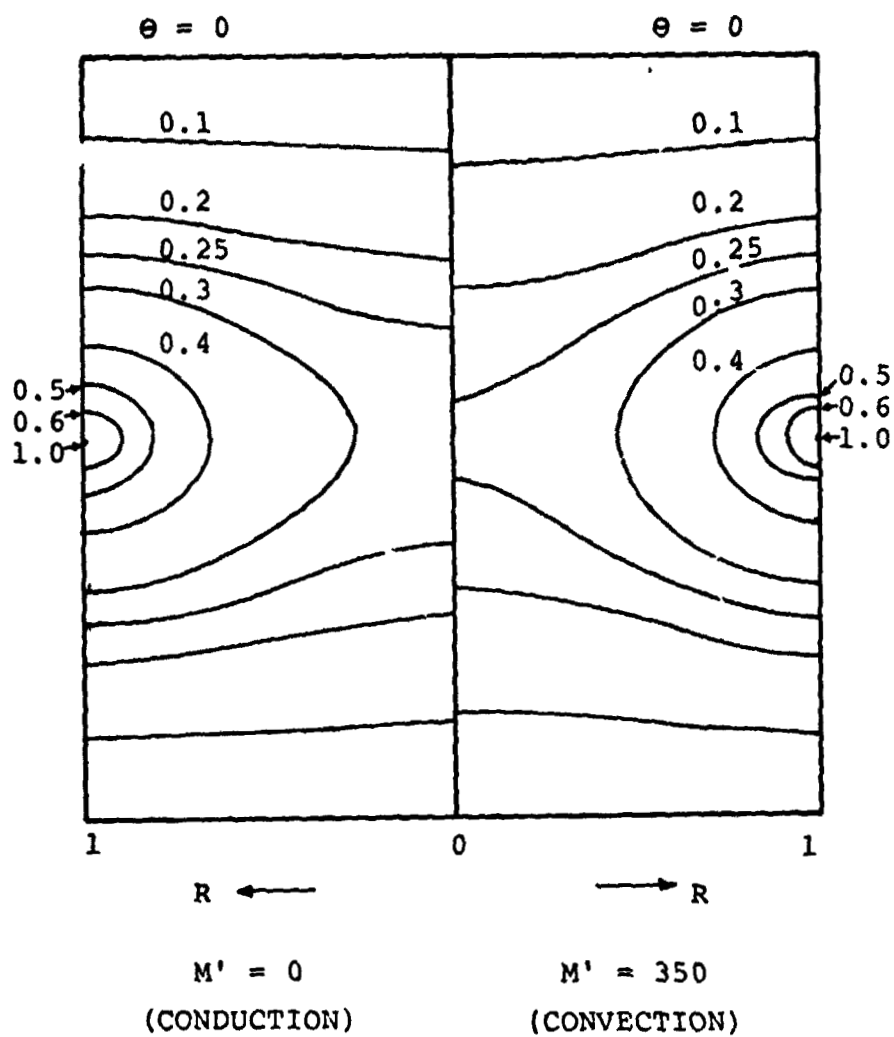


Figure 8. Comparison of isotherms  $\theta = (T - T_m) / (T_o - T_m)$  without convection and with convection for  $M' = 350$  (see Figure 7 for the flow field).

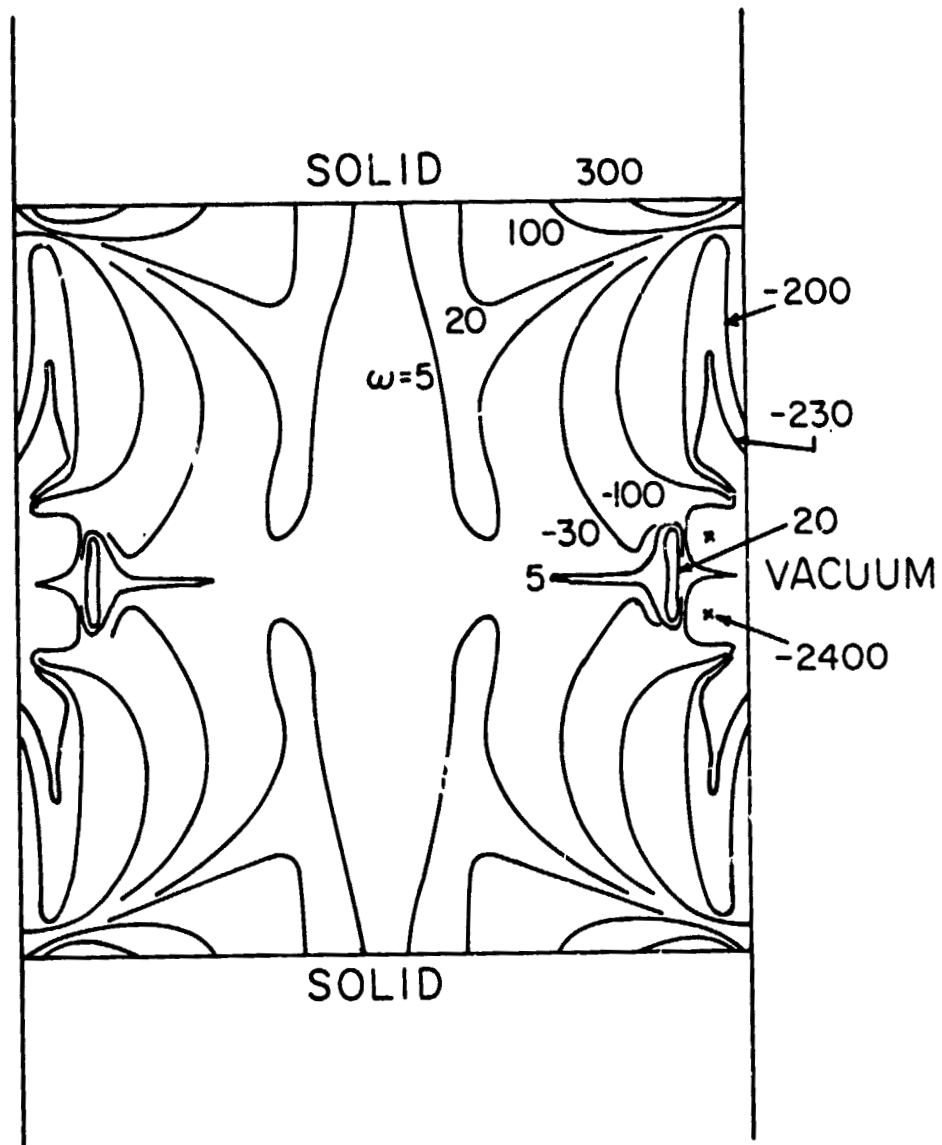


Figure 9. Dimensionless vorticity field  $\omega$  corresponding to the streamline field shown in Figure 7.



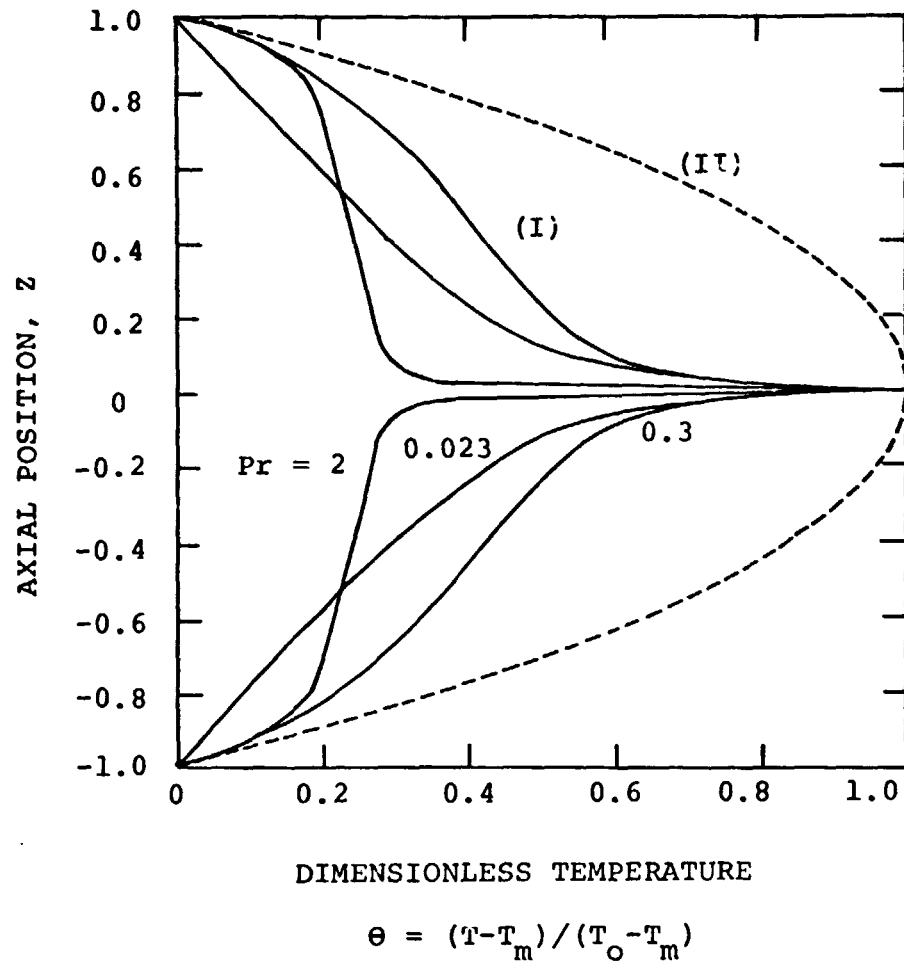


Figure 10. Axial dimensionless temperature profiles at the free liquid surface; (I) as solved from the electron beam beam heat transfer analysis coupled with the convection field for  $M' = 350$ ; (II) assumed parabolic.

cell near the liquid/solid interface shifts closer to the interface as the Prandtl number increases, as shown in Figures 11 and 12.

#### F. Influence of Zone Travel on Hydrodynamics

The effect of zone motion on the flow field was found to be negligible in all of our calculated streamlines for zone travel rates of up to 5 cm/hour in silicon. However, the effect becomes significant when the zone travel rate becomes comparable with the velocity of surface-driven flow.

The flow field shown in Figure 6 for  $M' = 35$  (our weakest flow) is taken as a model case in order to show the influence of zone travel on hydrodynamics in the floating zone. The maximum velocity of the melt for  $M' = 35$  is 0.07 cm/sec (or 250 cm/hour), and the average velocity is about 70 cm/hour. In Figures 13 through 16, the streamlines in floating zone melting of silicon at zero g are shown for freezing rates, 10, 30, 50, and 70 cm/hour with  $M' = 35$  ( $T_o - T_m = 0.005^\circ\text{C}$  for our silicon example). The lower vortex cell floats away from the bottom interface and its size is reduced as the zone travel rate increases. Thus, the flow patterns with zone motion are quite different from those with no motion when the zone travel rate is comparable with the surface driven flow.

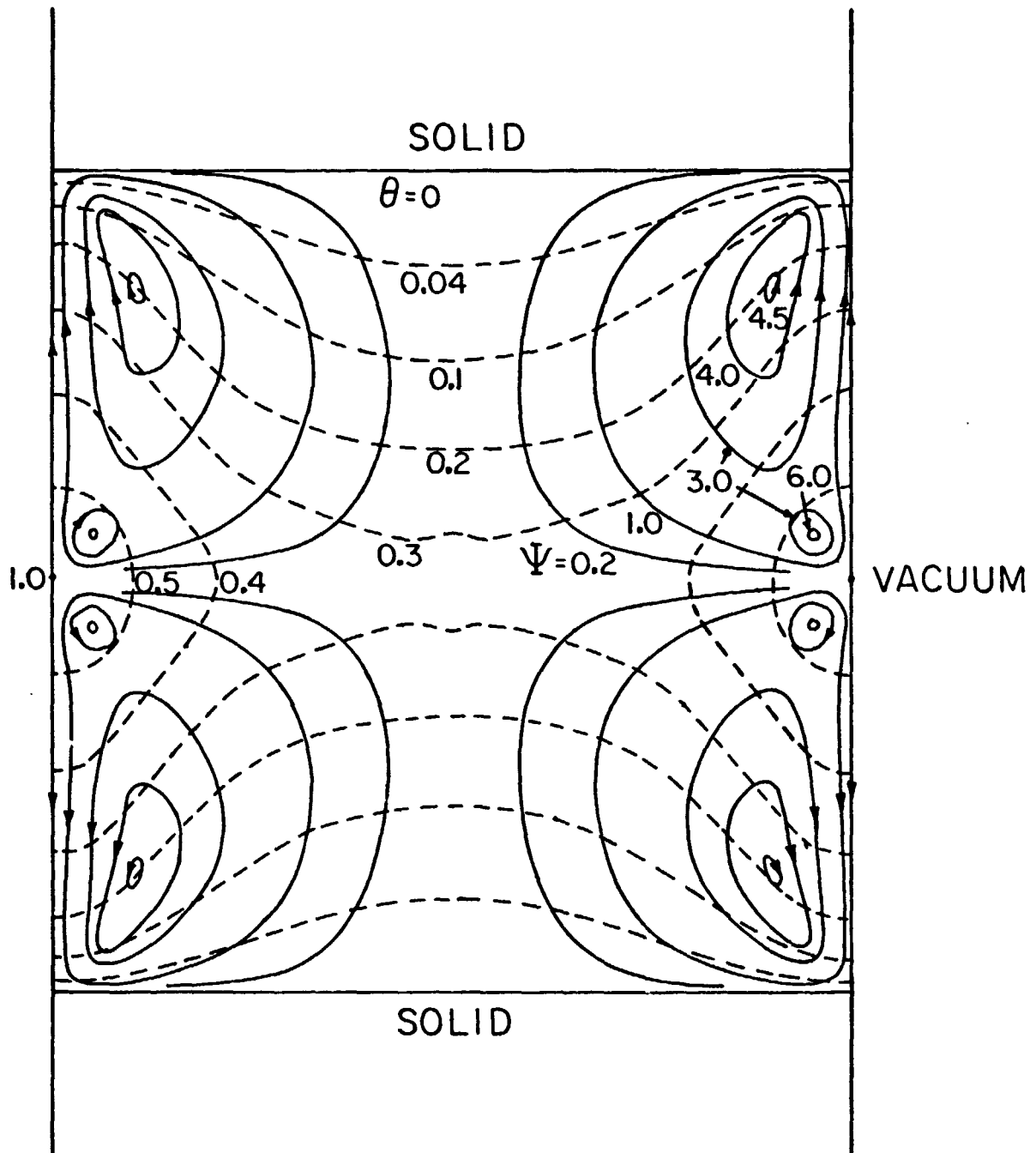


Figure 11. Computed isotherm  $\theta$  and streamlines  $\psi$  for surface tension driven flow in a floating zone at zero gravity from the computed temperature fields for electron beam heating, with the same conditions as in Figure 7, except  $Pr = 0.3$

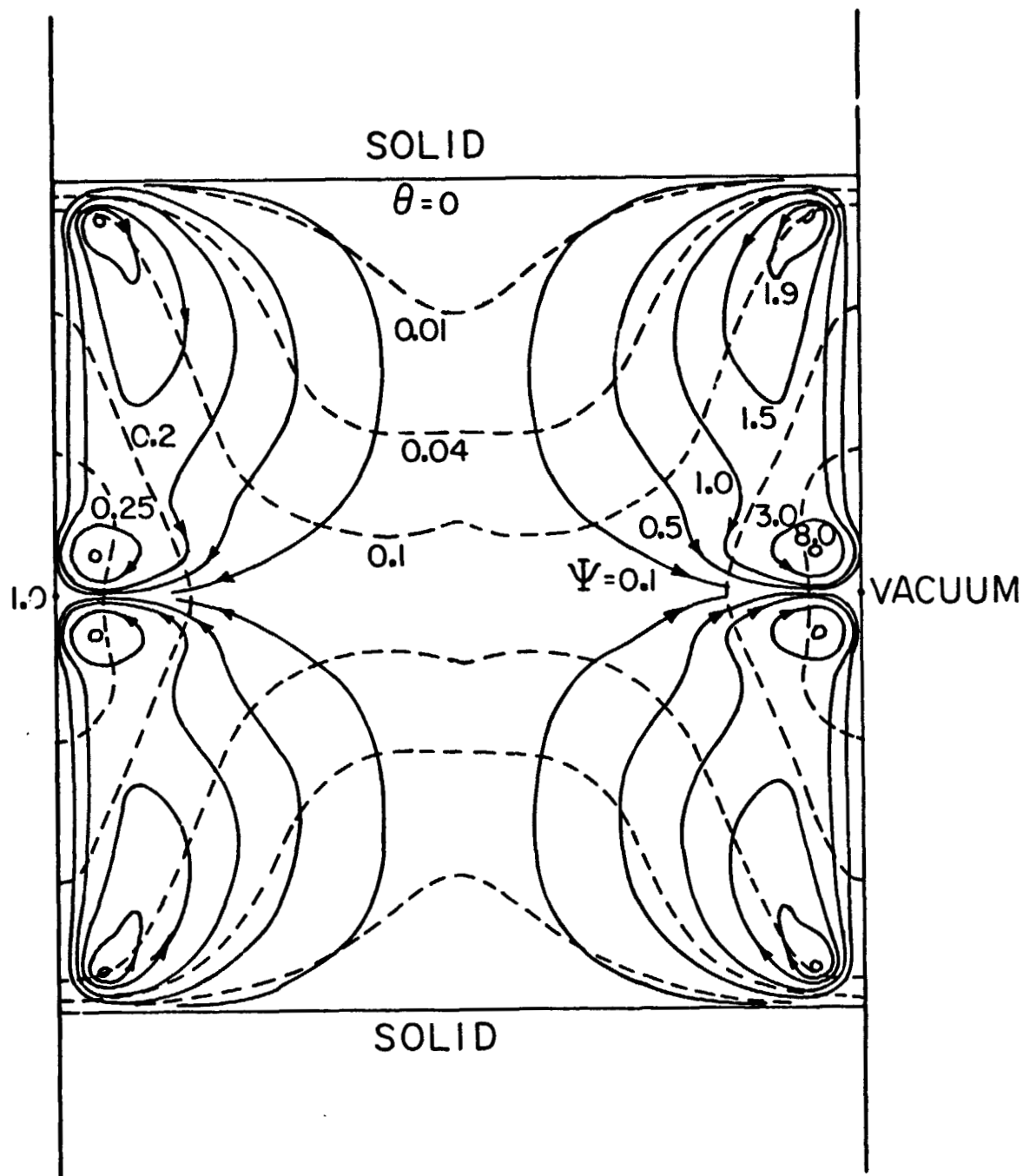


Figure 12. Computed isotherms  $\theta$  and streamlines  $\psi$  for surface tension driven flow in a floating zone at zero gravity from the temperature fields computed for electron beam heating with the same conditions as in Figure 7, except  $Pr = 2$ .

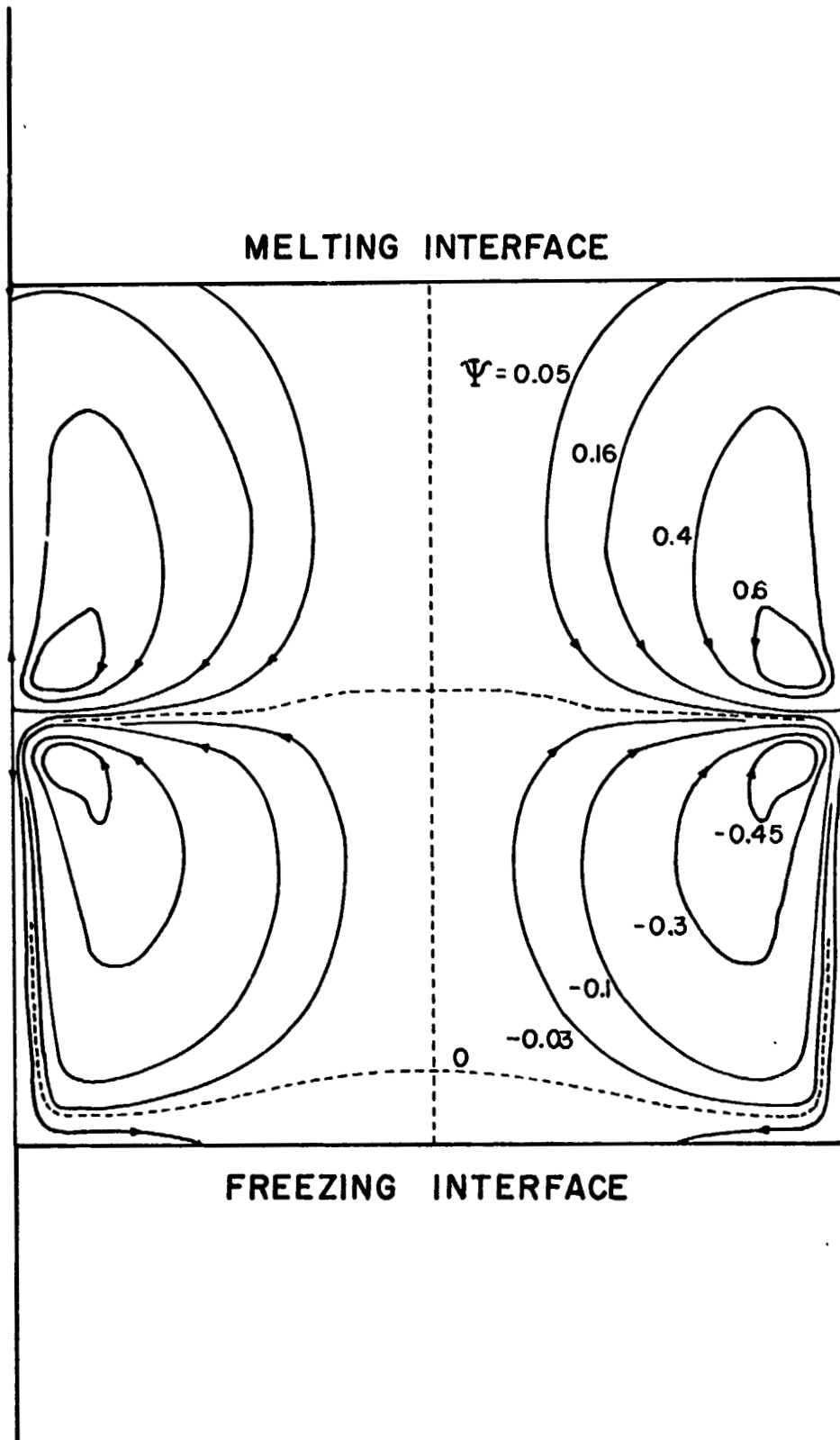


Figure 13. Computed streamlines  $\psi$  for surface tension driven flow in a floating zone at a zone travel rate of 10 cm/hour under the conditions of Figure 6.

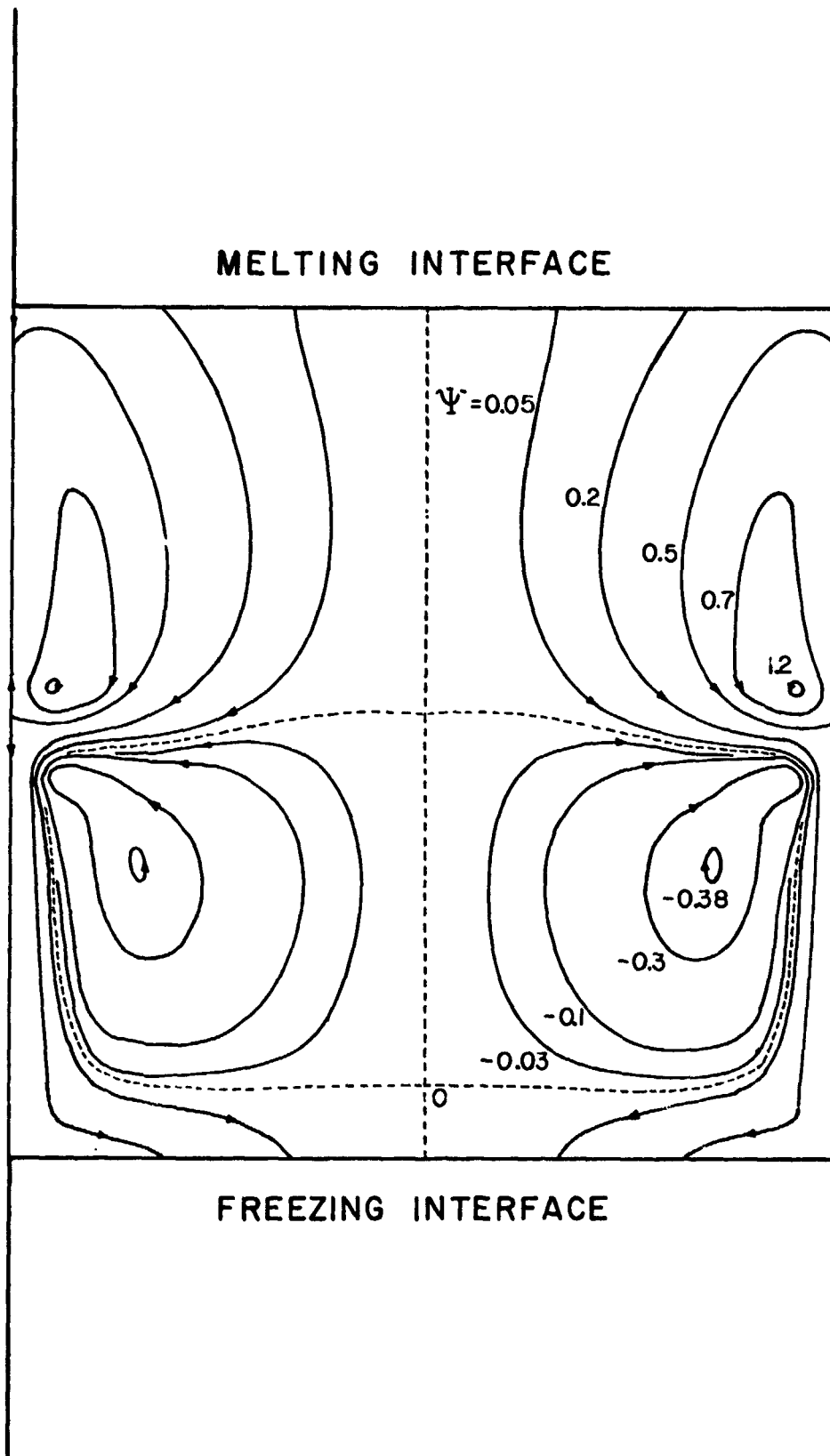


Figure 14. Computed streamlines  $\psi$  for surface tension driven flow in a floating zone at a zone travel rate of 30 cm/hour under the conditions of Figure 6.

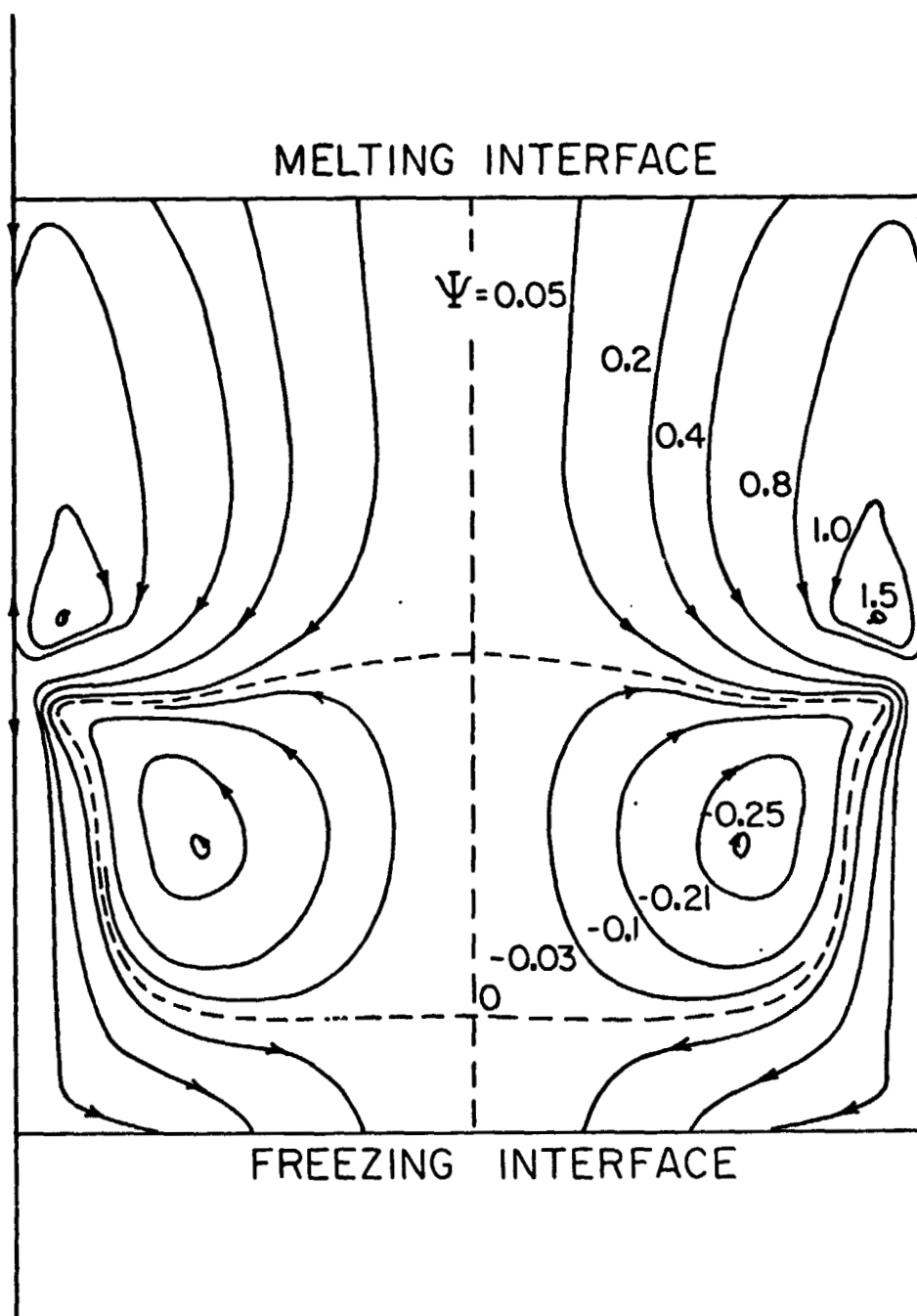


Figure 15. Computed streamlines  $\psi$  for surface tension driven flow in a floating zone at a zone travel rate of 50 cm/hour under the conditions of Figure 6.

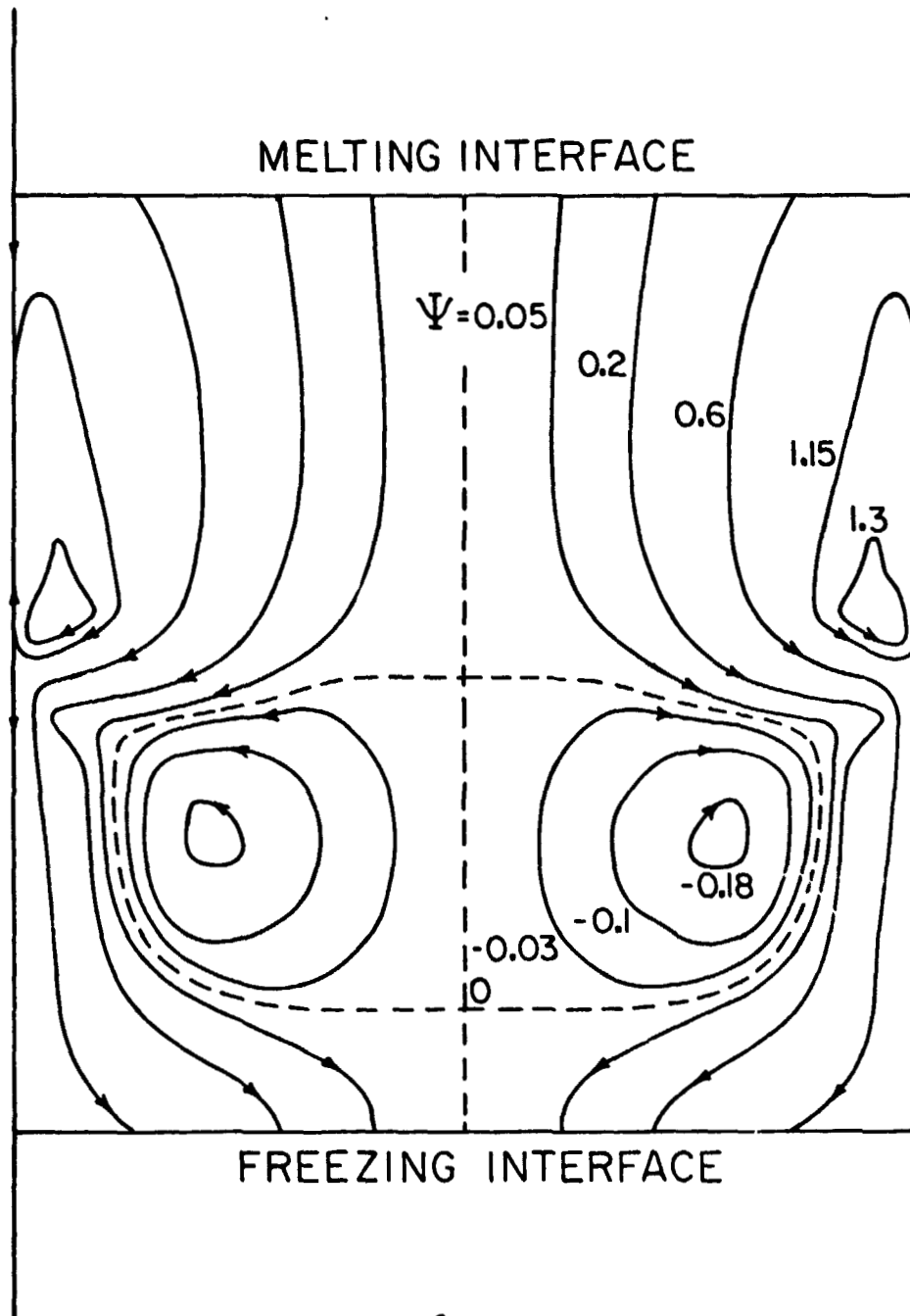


Figure 16. Computed streamlines  $\psi$  for surface tension driven flow in a floating zone at a zone travel rate of 70 cm/hour under the conditions of Figure 6.



### G. Impurity Segregation

Steady state\* impurity concentration fields in the melt were calculated by introducing the convection fields for  $M' = 350$  with zone motion. The values used in the present computations are:  $Sc = 5.0$ ,  $\rho_c = 2.28 \text{ g/cm}^3$ ,  $\rho_f = 2.54 \text{ g/cm}^3$ ,  $k_o = 0.1$ ,  $a = 0.5 \text{ cm}$ , and  $D = 7.6 \times 10^{-4} \text{ cm}^2/\text{sec}$ , which are typical for silicon with aluminum or indium impurity (2). The dimensionless impurity concentration fields,  $C = m/m_t$ , at steady state are shown in Figure 17 for a freezing rate  $v_c$  of 1 cm/hour ( $V_c = 0.0366$ ) and in Figure 18 for  $v_c$  of 5 cm/hour ( $V_c = 0.183$ ). The concentration fields follow somewhat the patterns of the convective flow fields, which implies that the convective mass transfer is large compared with the molecular diffusion. This is, of course, to be expected from the relatively high Schmidt number for silicon. The dimensionless impurity concentration profiles in the axial direction at  $R = 0, 0.5$  and  $1.0$  are plotted in Figure 19 for freezing rates of 1 cm/hour and 5 cm/hour. The magnitude of the mass transfer resistance is indicated by the rate of change of concentration with distance. Note that it is higher at the center of the zone because of the poor mixing between the top and bottom cells. This is to be contrasted with boundary-layer flow in which the mass transfer resistance is concentrated near solid/liquid interfaces.

---

\* When zone melting is initiated the impurity concentration in the melt increases (for  $k_o < 1$ ) until the same average concentration is freezing out of the melt as is being fed into the melt at the other interface. It takes several zone lengths of zone movement with convective mixing in the zone until this steady state is reached.

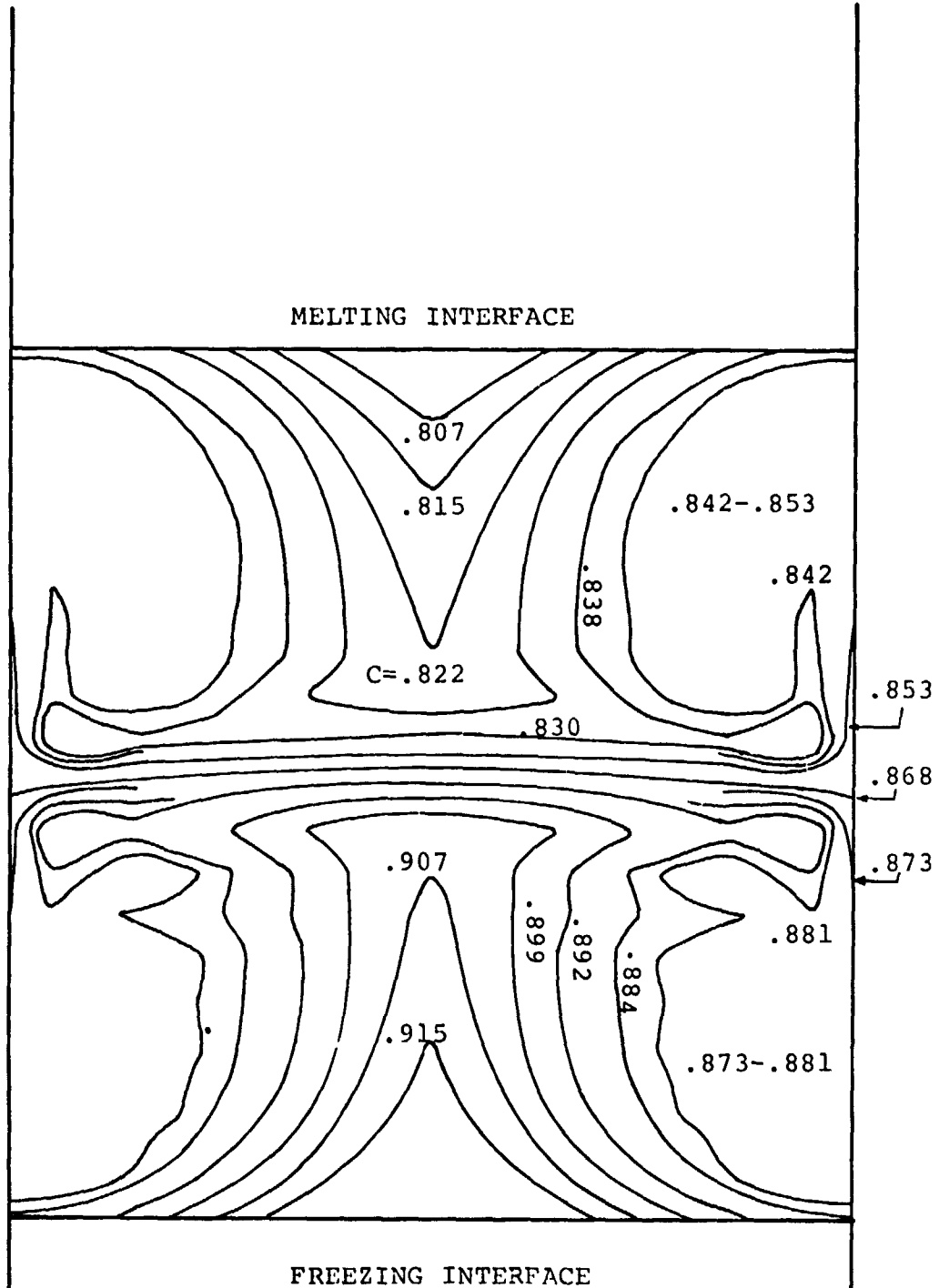
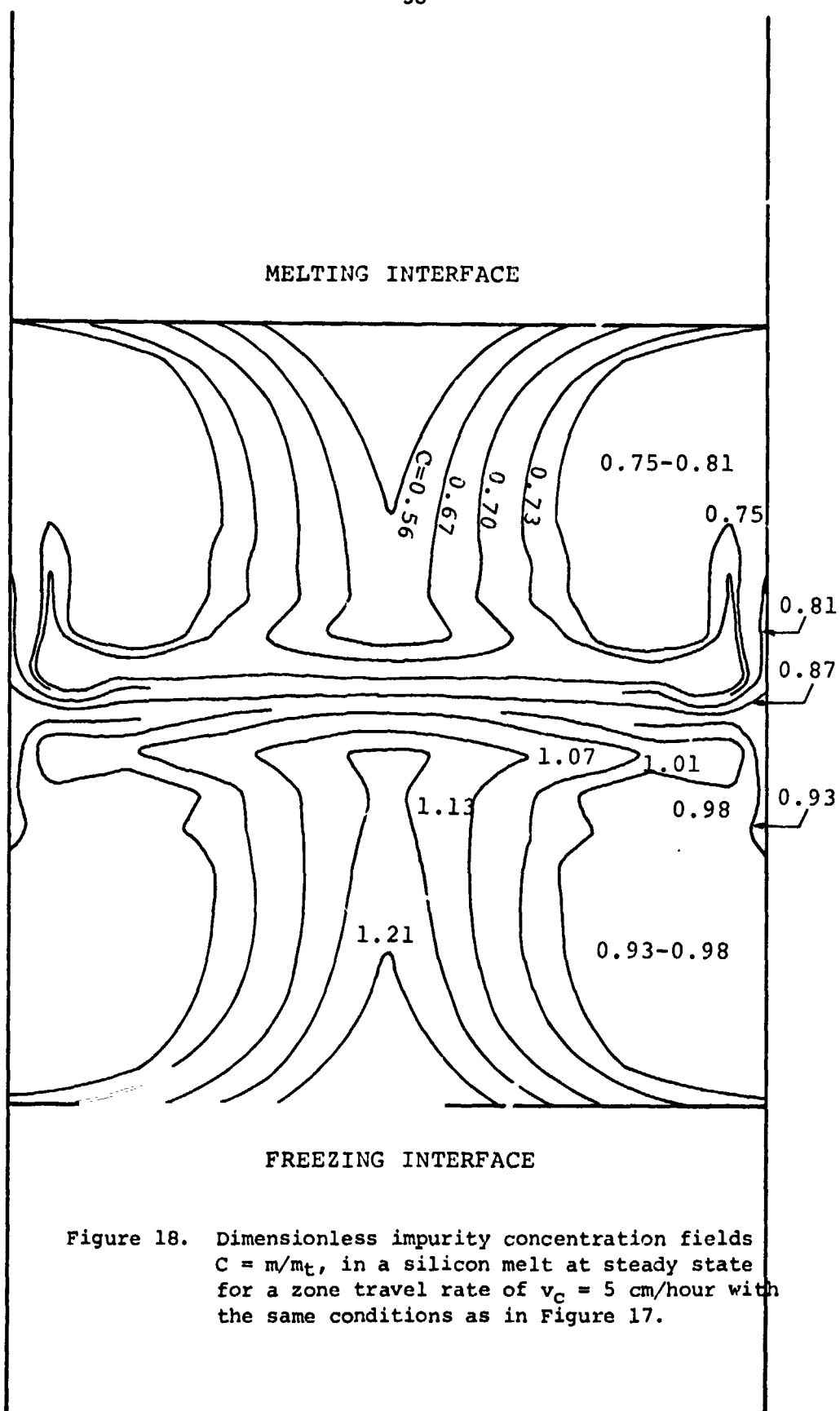


Figure 17. Steady state dimensionless impurity concentration fields,  $C = m/m_c$ , in a silicon melt for a zone travel rate of  $v_c = 1$  cm/hour with  $a = 0.5$  cm,  $M' = 350$ ,  $Pr = 0.023$ ,  $Sc = 5.0$ ,  $k_o = 0.1$ , and  $D = 7.6 \times 10^{-4}$  cm<sup>2</sup>/sec.



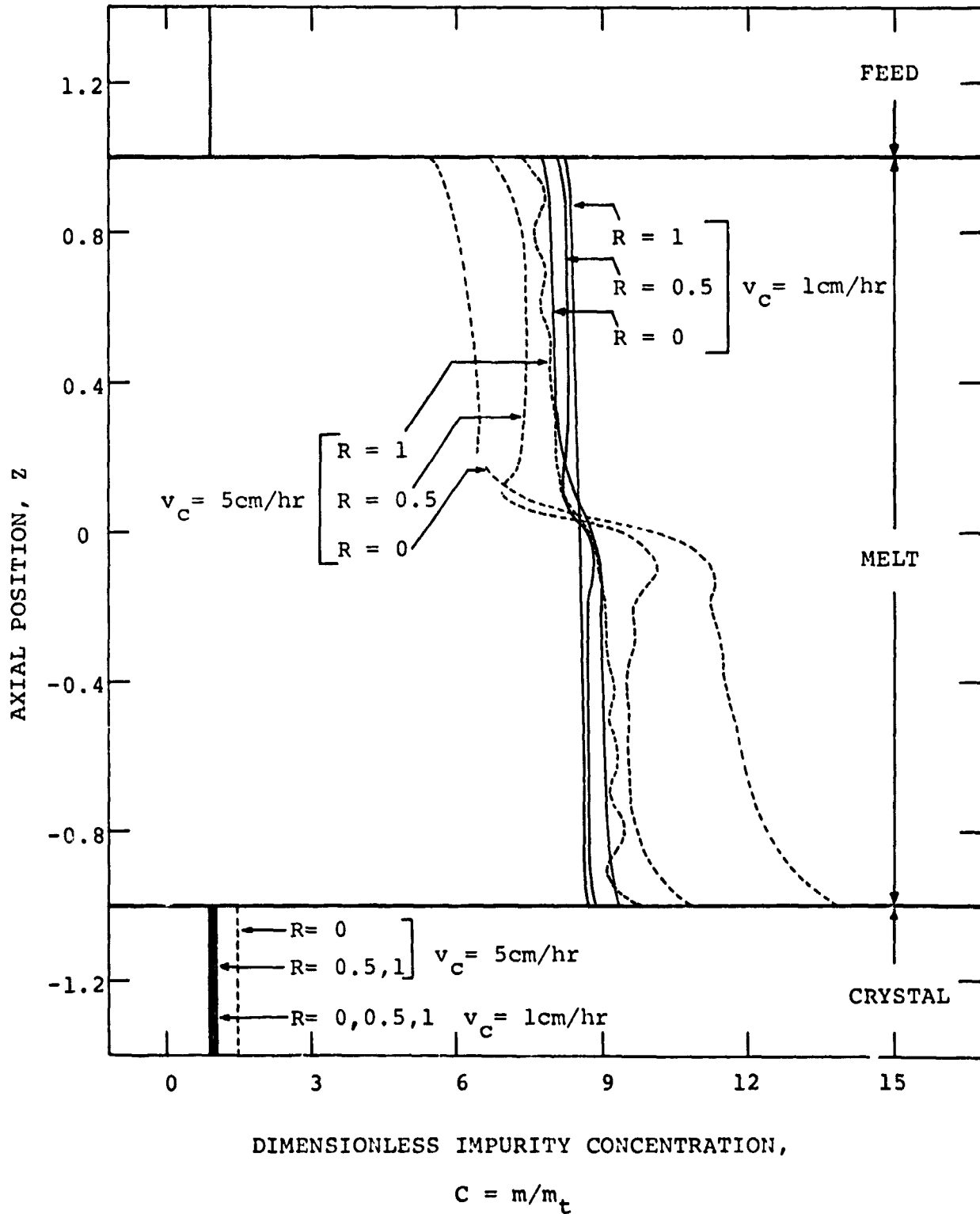


Figure 19. The calculated dimensionless impurity concentration profiles in the axial direction at  $R = 0, 0.5$ , and  $1.0$  under the same conditions as Figures 17 and 18.

The impurity concentration in the growing crystal was calculated by multiplying the concentration in the melt at the freezing interface by the interfacial distribution coefficient,  $k_0$ . The result is shown in Figure 20. For  $k_0 = 0.1$ , the convection in the zone with  $M' = 350$  leads to a 10% radial variation in the impurity concentration in the resultant crystal at a freezing rate of 1 cm/hour and a 40% radial variation at a freezing rate of 5 cm/hour. Note that 5 cm/hour is a typical crystal growth rate for silicon.

#### H. Constitutional Supercooling

The criteria for constitutional supercooling indicates that it is favored by a decreased temperature gradient and by an increased interfacial concentration gradient. The Nusselt number  $Nu$  corresponds to a dimensionless temperature gradient and the Sherwood number  $Sh$  corresponds to a dimensionless concentration gradient, defined as follows:

$$Nu = \left| \frac{\partial \theta}{\partial z} \right|_{+l/a} \quad (1)$$

$$Sh = \left| \frac{\partial C}{\partial z} \right|_{+l/a} \quad (2)$$

From Figures 7, 17 and 18, Nusselt numbers and Sherwood numbers were calculated and are shown in Figure 21. Constitutional supercooling at the freezing interface is more likely at the center of the crystal than at the periphery since the Sherwood number is higher at the

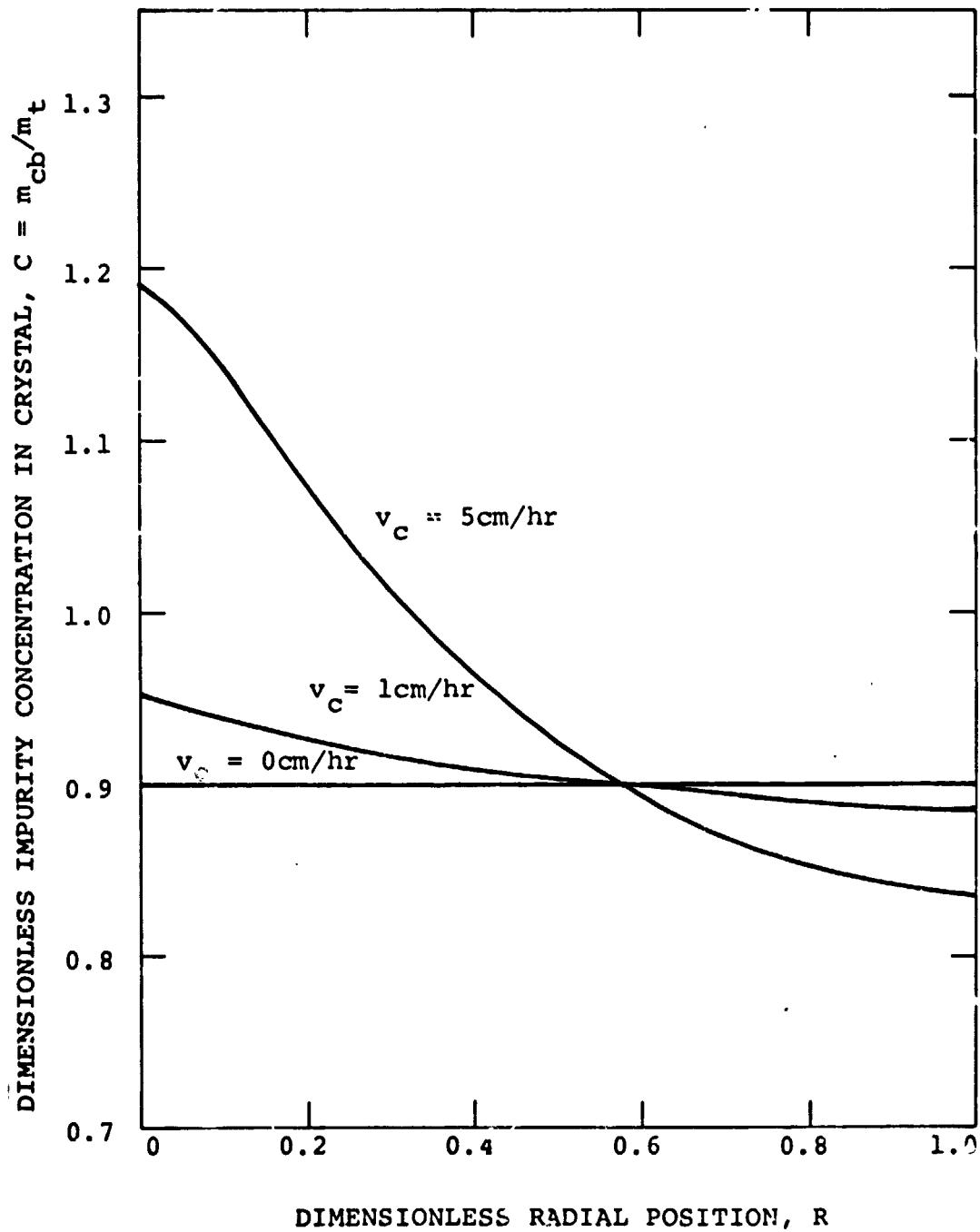


Figure 20. Radial impurity concentration profiles in the crystal at steady freezing rates of 0, 1, and 5 cm/hour calculated from the interfacial concentrations in Figures 17 and 18 for an interfacial distribution coefficient of  $k_0 = 0.1$

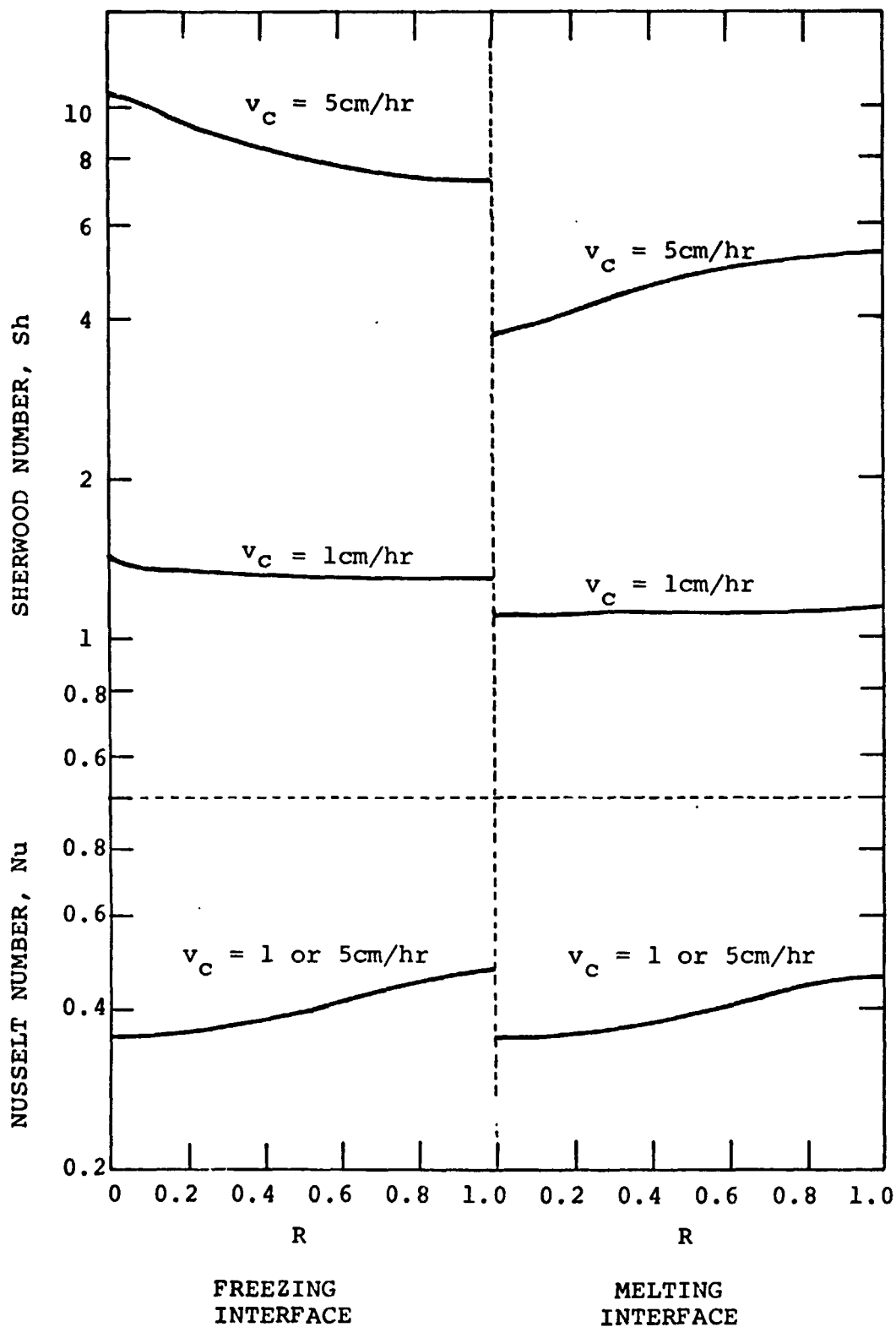


Figure 21. Radial variation of dimensionless temperature gradient (Nusselt number) and impurity concentration gradient (Sherwood number) at the melt/solid interfaces calculated from Figures 7, 17 and 18.

center while the Nusselt number is lower at the center. This tendency becomes more pronounced as the freezing rate increases since the radial variation of interfacial impurity concentration gradient as well as absolute interfacial concentration gradient increases, as shown in Figure 21. We have found previously that the preferred location for interfacial breakdown is strongly influenced by convection (3,4).

#### I. Influence of Gravity on Flow

In a vertical silicon melt with  $M' = 350$  ( $T_o - T_m = 0.05^\circ\text{C}$  for our silicon example), we found that at  $1 g_e$  ( $980 \text{ cm/sec}^2$ ) the flow and temperature fields in the floating zone do not change appreciably from those at zero  $g$ . When the acceleration is increased to  $10 g_e$ , the lower vortex contracts while the upper one is expanded, particularly at the center of the zone where the flow field is relatively weak. This is shown in Figure 22 and may be compared with Figure 7 at zero  $g$ . This means that surface driven flow predominates even on earth for many materials for radiant and electron beam heating. It may even be important when induction heating is employed and may account for some of the compositional inhomogeneities observed.

#### J. Influence of Thermal Environment on Isotherms

The previous results on streamlines were based on low heat flux conditions accomplished by increasing the temperature of the surroundings sufficiently or by effective heat shielding. In addition the solid phase was not included in the heat transfer analysis. In order



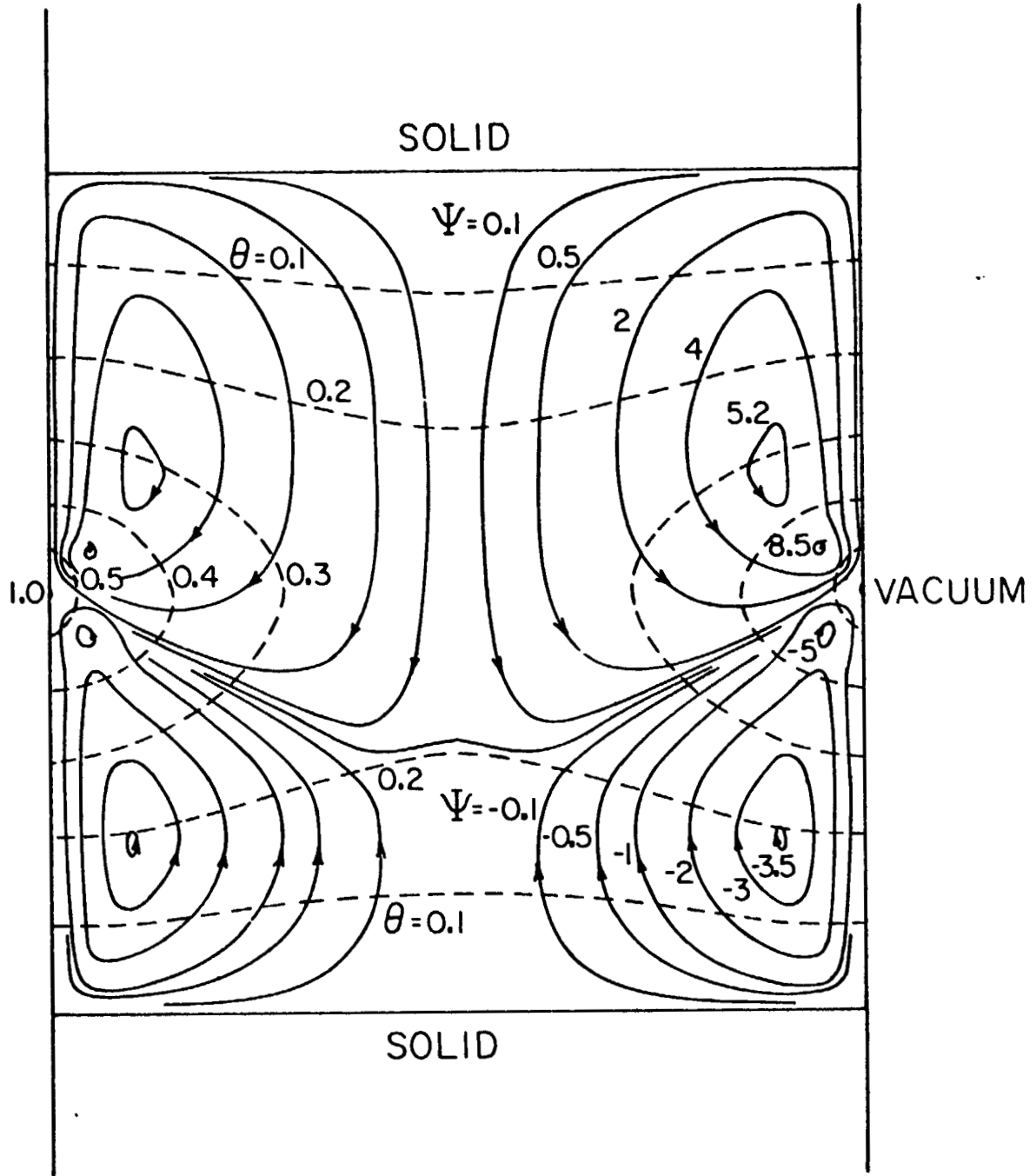


Figure 22. Computed streamlines and isotherms for combined surface driven and buoyancy driven flow with  $g = 10 g_e = 9800 \text{ cm/sec}^2$ . Other conditions are the same as Figure 7.

to see how much difference this makes, pure conduction analyses were made. A low ambient temperature (i.e.,  $T_c = 23^\circ\text{C}$ ) was used. Three different thermal boundary conditions at the end of the ingot were also investigated. Three possible conditions were considered; that is, radiation, insulation and rapid heat transfer from the end to the surroundings. For electron-beam heating, the heat flux varied substantially depending on the thermal boundary conditions. The required power supply computed from the temperature gradients is 236, 228 and 492 watts for the case of radiation, insulation and infinite heat transfer coefficient at the top surface, respectively. This result is found to be close to Donald's (5) experimental result (198 watts) for electron-beam floating zone melting of 1 cm diameter silicon. In spite of the changes in heat flux, the isotherms in the zone vary little when the length of the solid ingots is the same as that of the zone, as shown in Figures 23 through 25. This was also true with a reduced length of solid, as shown in Figure 26. More significantly, isotherms in the zone with high heat fluxes are not very different from those with very low heat fluxes.

#### K. Influence of Materials Parameters

Inspection of the governing differential equations in Appendix A shows that the parameter which determines the vigor of the surface driven convection is  $M' = \rho\sigma(T_o - T_m)a/\mu^2$ . The temperature difference  $(T_o - T_m)$  along the melt surface increases as the melting point increases and as the thermal conductivity decreases, as well as with decreasing

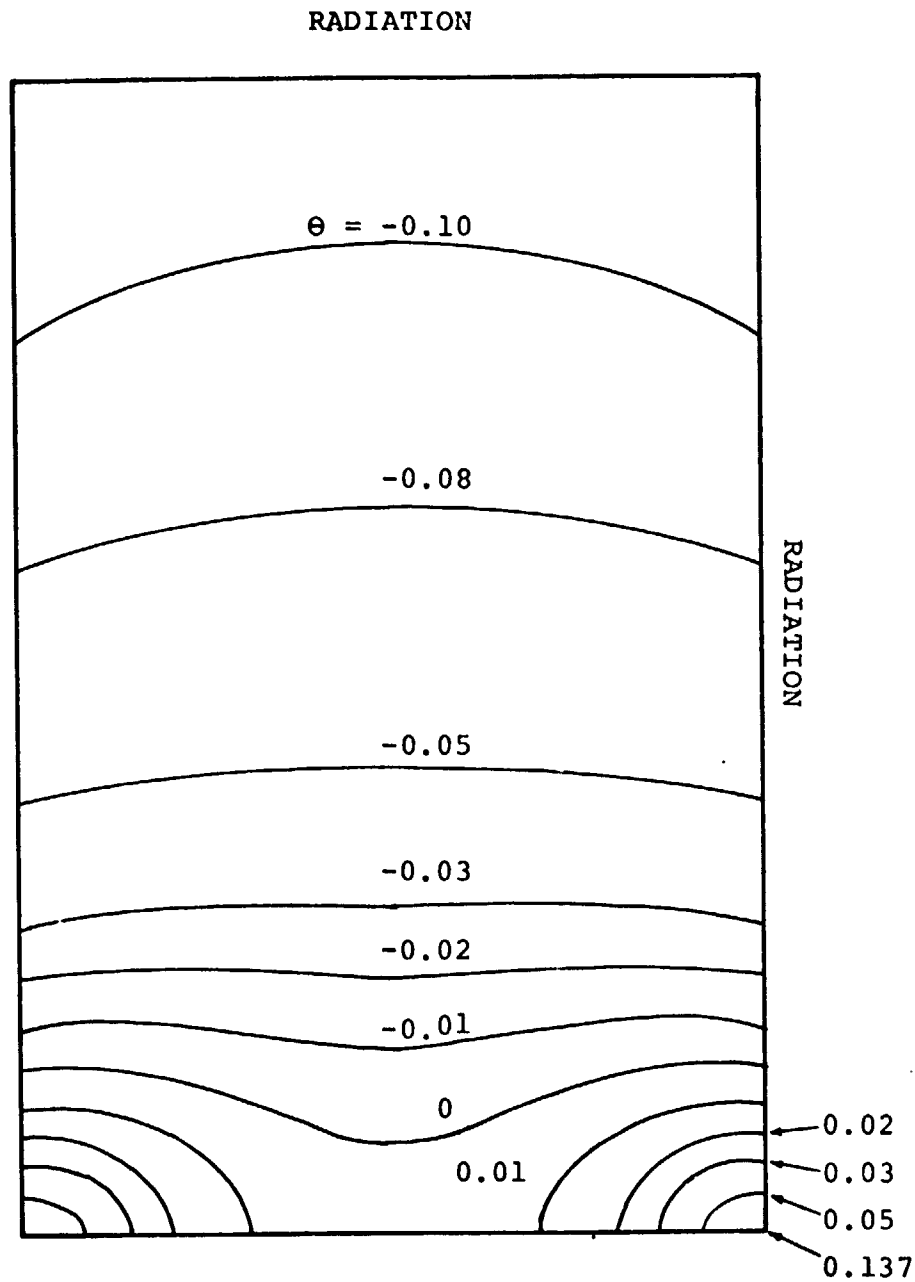


Figure 23. Computed isotherms,  $\theta = (T - T_m) / (T_m - T_c)$ , in the ingot above the center of the zone with  $T_o = 1600^\circ\text{C}$ ,  $T_c = 23^\circ\text{C}$ ,  $T_m = 1410^\circ\text{C}$ ,  $a = 0.5$  cm,  $Pr = 0.023$  and  $\epsilon_s = 0.3$ . Thermal radiation boundary condition used at the end of the solid.

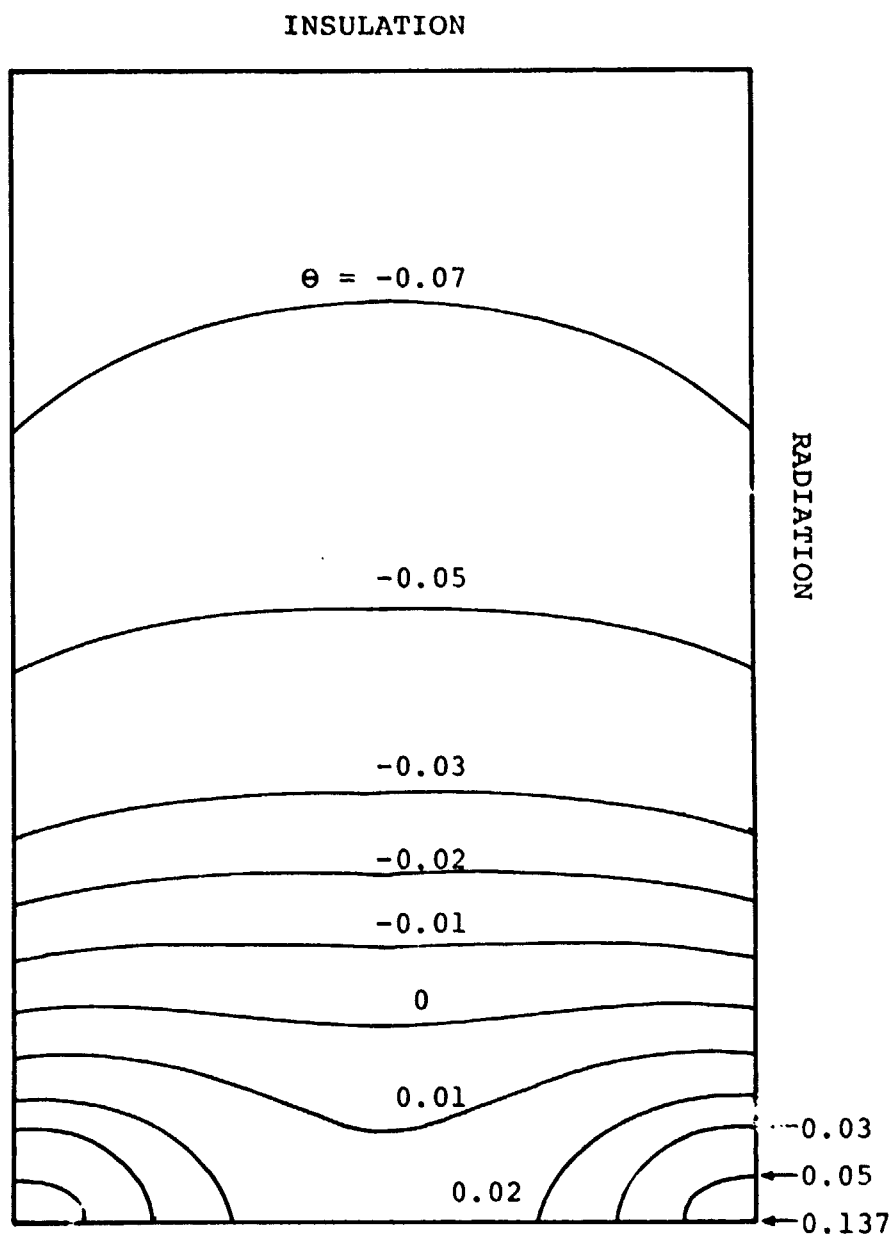


Figure 24. Computed isotherms,  $\theta = (T - T_m) / (T_m - T_c)$ , in the ingot above the zone center with the same conditions as in Figure 23, except an insulation boundary condition at the end of the solid.  $T_o - T_m = 190^\circ \text{C}$ .

INFINITE  
HEAT TRANSFER

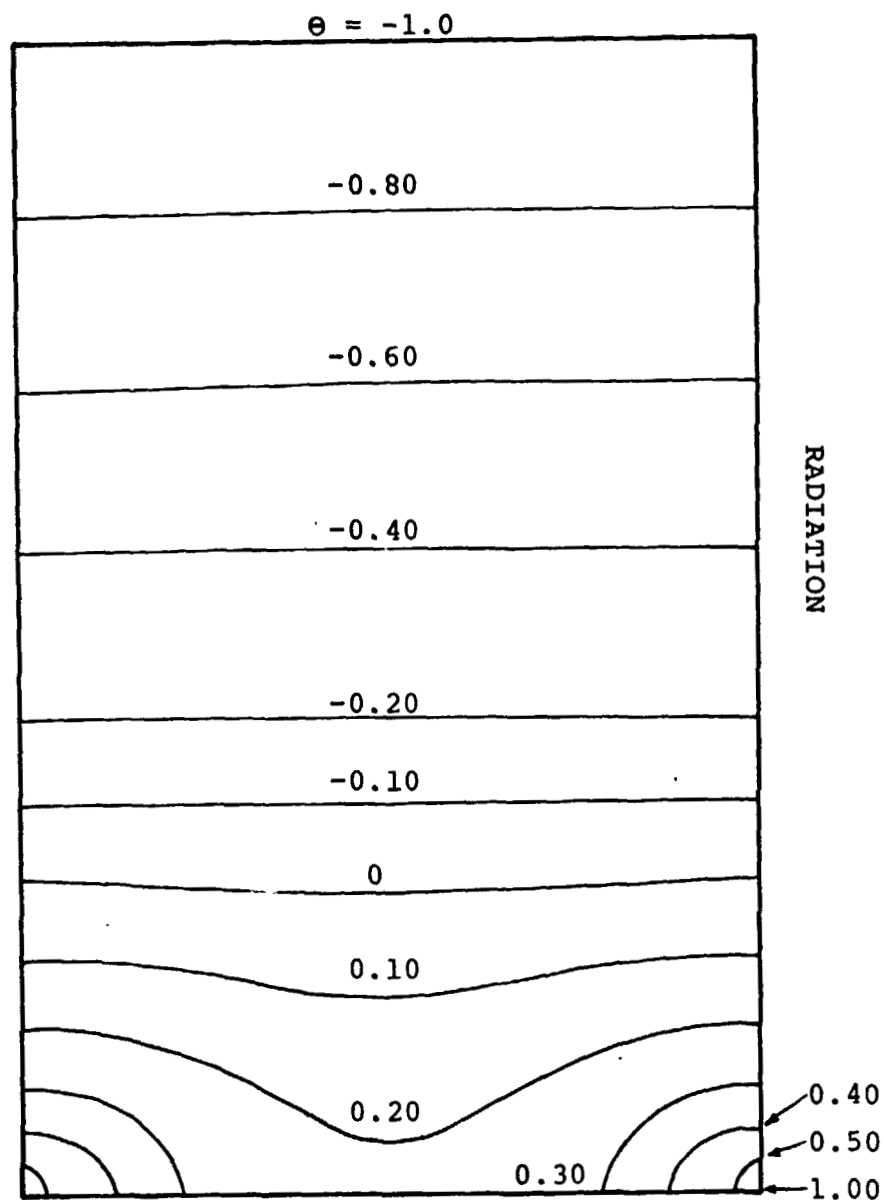


Figure 25. Computed isotherms,  $\theta = (T - T_m) / (T_m - T_c)$ , in the ingot above the zone center with the same conditions as in Figure 23, except  $T_o = 2800^\circ\text{C}$  and the heat transfer is very rapid at the end of the solid.  $T_o - T_m = 1390^\circ\text{C}$ .

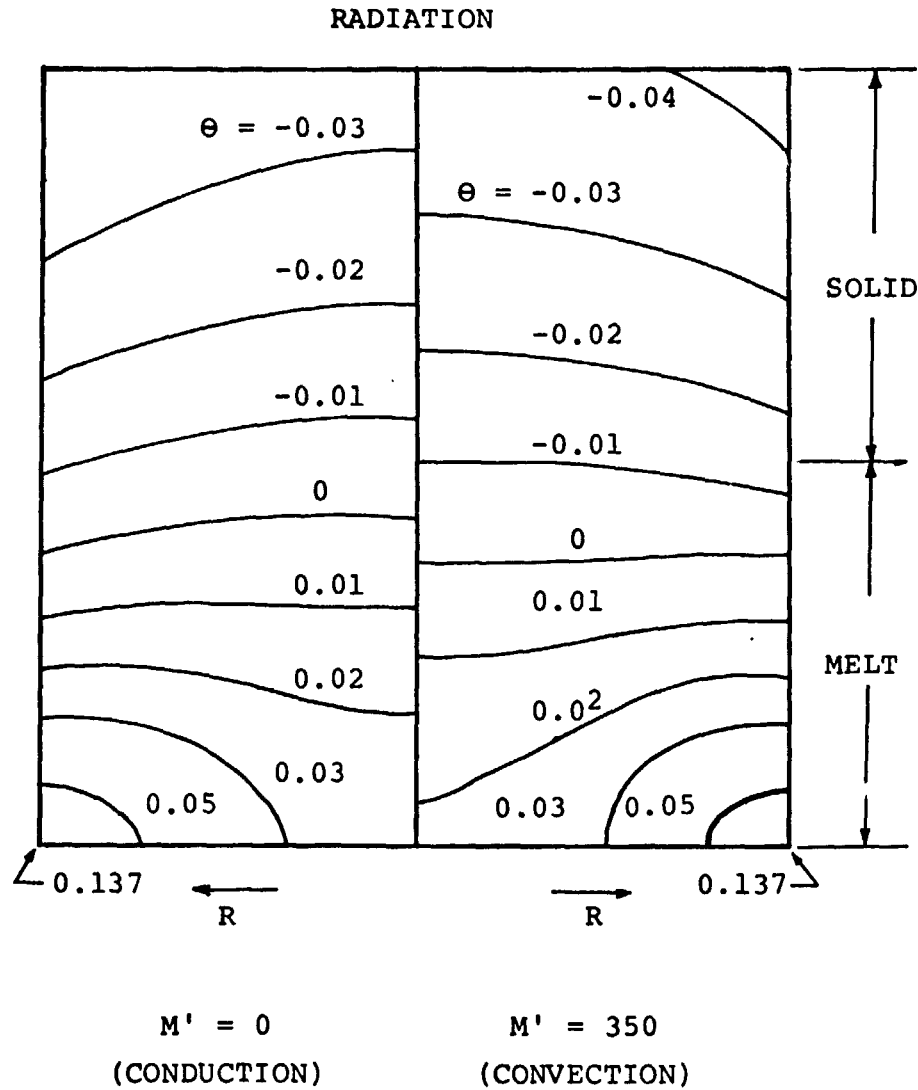


Figure 26. Computed isotherms,  $\theta = (T - T_m) / (T_m - T_c)$ , in the solid and the liquid above the zone center with the same conditions as in Figure 23. The left half of the figure is for pure conduction, and the right half is with the convection shown in Figure 3.

heat shielding. Unfortunately we are unable at this time to express this quantitatively, although our computer programs are capable of estimating any particular case. If we remove  $(T_o - T_m)a$  from  $M'$  we are left with the material parameters  $\rho\sigma/\mu^2$ . Values for selected materials are shown in Table II, from which it is seen that our test material, silicon, is one of the materials more sensitive to temperature variations. The parameter which expresses the sensitivity of segregation to flow conditions is the Schmidt number  $Sc$ . Note that  $Sc$  is lowest for silicon among all of the materials in Table II. While general conclusions are difficult, it seems clear that surface tension driven flow will manifest itself in nearly all materials with a free melt surface subjected to a temperature gradient.

TABLE II. SOME PROPERTIES OF LIQUIDS NEAR MELTING POINT

Material	$\gamma$ dyne/cm	$\sigma = -\partial\gamma/\partial T$ dyne/cm °C	$\rho$ g/cm <sup>3</sup>	$\mu$ c.p.	$k$ cal/cm °C sec	$C_p'$ cal/g °C	$D \times 10^{-4}$ cm <sup>2</sup> /sec	$Pr = \frac{C_p \mu}{k}$	$Sc = \frac{\mu}{\rho D}$	*
Water	73	0.16	1.0	1.00	0.0014	1.00	0.1	7.3	1,000	1,600
Benzene	29	0.13	0.9	0.91	0.0004	0.40	0.1	9.3	1,010	1,410
Naphthalene	29	0.15	0.98	0.98	0.00029	0.40	0.1	14.0	1,000	1,480
Na	202	0.10	0.81	0.69	0.20	0.35	0.4	0.012	210	1,600
Cu	1,300	0.31	7.9	3.33	0.41	0.13	0.5	0.011	84	2,210
Fe	1,880	0.43	7.0	2.25	0.043	0.18	1.4	0.094	23	5,930
Si	720	0.43	2.5	0.88	0.077	0.20	7.0	0.023	5	14,000
Ge	650	0.60	5.6	0.75	0.043	0.09	1.3	0.016	10	59,500
Ga	718	0.10	6.2	1.90	0.067	0.10	0.2	0.028	150	1,730
GaAs	530	0.25	5.7	1.77	0.20	0.08	1.2	0.007	26	4,550
NaCl	114	0.071	1.54	1.30	0.0095	0.20	1.0	0.27	84	640
KCl	96	0.072	1.51	1.42	0.0095	0.20	1.0	0.30	94	540
Al <sub>2</sub> O <sub>3</sub>	700	0.06	3.05	2.72	0.024	0.30	2.2	0.34	40	865

\*  $M' / (T_o - T_m) a$



### III. TRANSIENT FREE CONVECTION AT LOW G ABOUT A SUSPENDED CRYSTAL

(Chong K. Kim)

#### Definition of Symbols

a	Radius of sphere, cm
d	Diameter of sphere (= 2a), cm
D/Dt	Substantial derivative. Rate of change as one moves along with fluid $= \frac{\partial}{\partial t} + u_x \frac{\partial}{\partial x} + u_y \frac{\partial}{\partial y} + u_z \frac{\partial}{\partial z}$ in cartesian coordinates
g	Acceleration, cm/sec <sup>2</sup>
g <sub>e</sub>	Earth's gravitational acceleration, 980 cm/sec <sup>2</sup>
Gr	Grashof number $\frac{d^3 g \alpha \Delta W}{\nu^2} \sim \frac{\text{buoyancy force}}{\text{inertial force}}$
K	Mass transfer coefficient, cm/sec
p	Pressure of the fluid, dynes/cm <sup>2</sup>
p'	Pressure due to fluid motion, dynes/cm <sup>2</sup>
P	Dimensionless pressure, $p'a^2/\rho\nu^2$
r	Radial distance from the center of the sphere, cm
R	Dimensionless radial distance, r/a
Ra	Rayleigh number, GrSc
Sc	Schmidt number $\frac{\nu}{D} \approx \frac{\text{momentum diffusivity}}{\text{molecular diffusivity}}$
Sh	Sherwood number, dimensionless composition gradient, $Kd/D =  \partial\phi/\partial R _1$
t	Time, seconds

$u$	Radial velocity, cm/sec
$U$	Dimensionless radial velocity, $ua/v$
$v$	Velocity in angular direction, cm/sec
$V$	Dimensionless radial velocity, $va/v$
$x, y, z$	Coordinates in rectangular system
$w$	Mass fraction of solute
$\alpha$	Concentration densification coefficient
$\theta$	Angle from negative of accelerational vector
$\mu$	Viscosity of fluid, g/cm sec
$\nu$	Kinematic viscosity, $\mu/\rho$ , $\text{cm}^2/\text{sec}$
$\rho$	Density of the fluid, $\text{g/cm}^3$
$\tau$	Dimensionless time, $t\nu/a^2$
$\phi$	Azimuthal angle
$\Phi$	Dimensionless concentration, $W-W_\infty/W_0-W_\infty$
$\psi$	Dimensionless stream function (Eq. B-8)
$\omega$	Dimensionless vorticity (Eqs. B-8 and B-11)

#### Subscripts

$o$	Surface condition
$\infty$	Initial condition
$e$	Earth condition
$\theta$	Angular
$i, j, m$	Arbitrary integer
$r$	Radial

- T     Constant temperature condition  
 $\phi$     Azimuthal angular

#### A. Introduction

The object of this project was to elucidate the nature of the convection about a suspended crystal growing from a solution in a spacecraft environment. The small fluctuating accelerations will give rise to transient free convection currents. There have been very few studies of steady state free convection at very low Grashof numbers, and none have been done on transients. (Grashof number is roughly equivalent to the ratio of buoyancy to viscous forces.)

#### B. Model

For simplicity, our attention was devoted to mass transfer about a sphere suspended in a solution. The following assumptions were employed:

- a) Two-dimensional flow, i.e., no azimuthal flow.
- b) Constant properties ( $\rho$ ,  $D$ ,  $\mu$ )
- c) Low gravity ( $g = 10^{-3} g_e \sim 10^{-6} g_e$ )
- d) Influence of rate of change of crystal size was neglected.

The partial differential equations and boundary conditions for flow and for mass transfer are shown in Appendix B. Finite difference methods were used on the computer. Although the results are expressed in dimensionless form, it is helpful to think in terms of a concrete example. We considered a 1 cm diameter KCl sphere growing from water at 25°C with a supersaturation of 0.1 mole/l at  $g = 1.25 \times 10^{-4} g_e =$

0.122 cm/sec<sup>2</sup>. The pertinent parameters are  $d = 1$  cm,  $W = W_0 - W_\infty = -0.0075$ ,  $\rho = 1.18$  g/cm<sup>3</sup>,  $\mu \approx 0.01$  g/cm sec,  $\alpha = (\partial\rho/\partial W)_T/0 = 0.616$  and  $D = 1.8 \times 10^{-5}$  cm<sup>2</sup>/sec. These yield  $Sc = \nu/D = 465$ ,  $Gr = |d^3 g \alpha \Delta W / \nu^2| = 7.9$ , and  $Ra = 3670$ . The boundary-layer approximation is expected to be valid only for  $Ra > 10^4$  (6). In other words, the perturbed region in the solution is expected to be on the order of the same size as the growing crystal.

### C. Convection-Free Mass Transfer (Diffusion)

Before studying mass transfer with convection, it is interesting to first look at the diffusion problem. We consider a sphere in an infinite body of solution at zero  $g$ . The pertinent differential equation is:

$$\frac{\partial \phi}{\partial \tau} = \frac{1}{\nu/D} \left[ \frac{\partial^2 \phi}{\partial R^2} + \frac{2}{R} \frac{\partial \phi}{\partial R} \right] \quad (3)$$

with boundary conditions:

$$\begin{aligned} \text{at } \tau = 0, \quad \phi &= 0 \\ \text{at } R = 1, \quad \phi &= 1 \\ \text{at } R = \infty, \quad \phi &= 0 \end{aligned}$$

The solution to this is:

$$\phi = \frac{1}{R} \operatorname{erfc} \frac{R-1}{2\sqrt{\tau/(\nu/D)}} = \frac{1}{R} \operatorname{erfc} \frac{R-1}{2\sqrt{Dt/a^2}} \quad (4)$$

This is plotted in Figure 27. The Sherwood number is

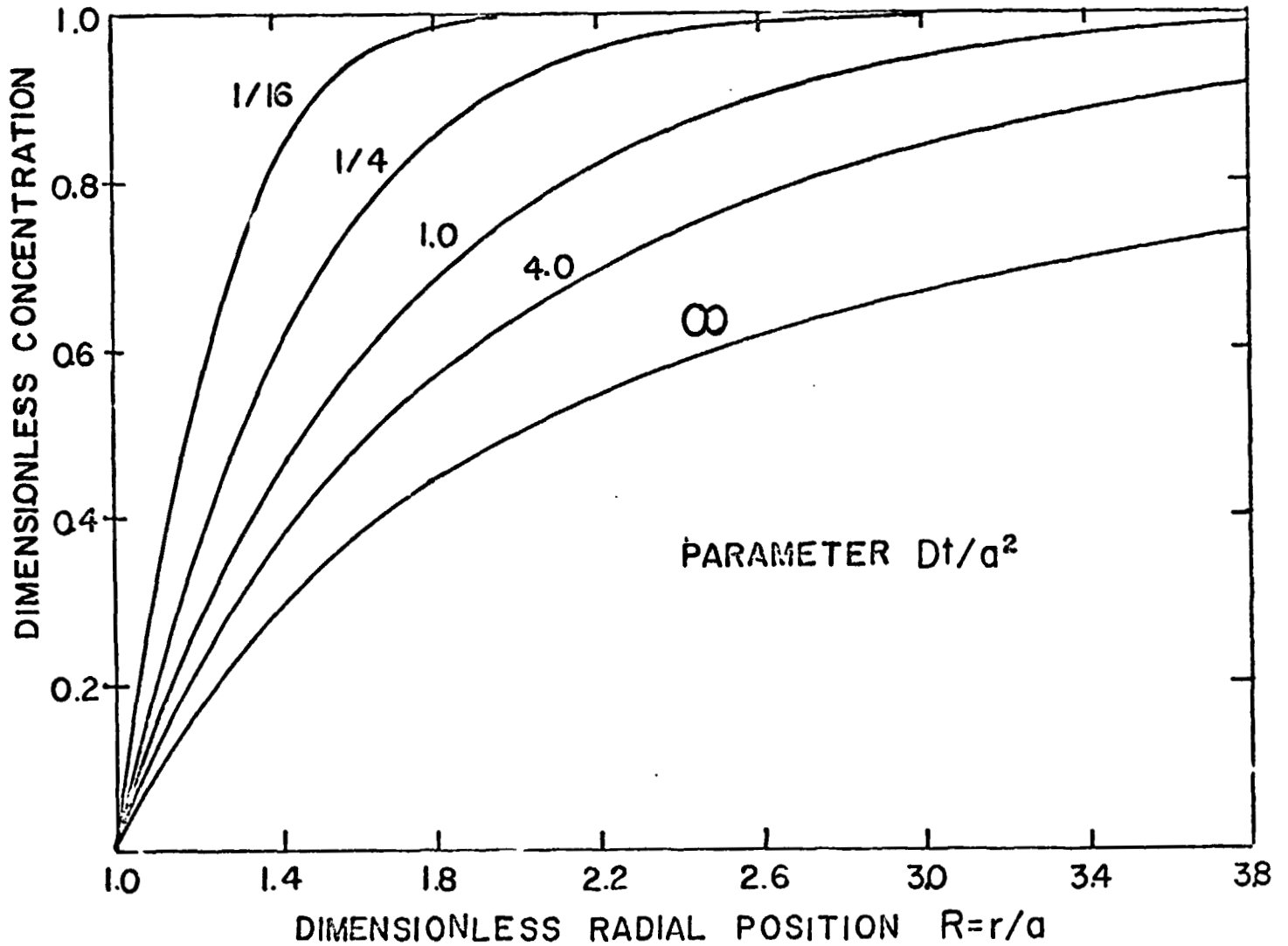


Figure 27. Concentration profiles for diffusion without convection from sphere of radius  $a$  into infinite fluid. Dimensionless concentration is  $1 - \phi = (w - w_0)/(w_\infty - w_0)$ . Plotted from Eq. (4).

$$\begin{aligned}
 Sh &= \frac{-2Ka}{D} \\
 &= -2 \left( \frac{\partial \phi}{\partial R} \right)_{R=1} = 2 \left[ 1 + \frac{1}{\sqrt{\pi Dt/a^2}} \right], \quad (5)
 \end{aligned}$$

which is plotted in Figure 28. From these figures it is seen that to reach steady state requires  $Dt/a^2 \sim 5$ , or for our example parameters,  $t \sim 69,600 \text{ sec} = 19.3 \text{ hour}$ . This is to be compared with Siegel's (7) predictions based on transient boundary-layer equations for  $Sc \gg 1$ . He estimated that the time to reach steady state with convection on a vertical flat plate is  $5.24 (0.952 + Sc)^{1/2} |g\alpha\Delta W|^{-1/2} d^{1/2} = 4760 \text{ sec} = 1.32 \text{ hours}$  for our example. The time over which the above solution for pure diffusion should be valid was estimated to be  $1.80 (1.5 + Sc)^{1/2} (g\alpha\Delta W)^{-1/2} d^{1/2} = 1640 \text{ sec} = 17 \text{ min}$ .

#### D. Convective Mass Transfer

In order to reduce the computation time and to approximate a realistic geometry, a spherical boundary at ten times the sphere radius was chosen. The fluid velocity and the concentration gradient at the boundary were set equal to zero. Unfortunately computations were not carried on sufficiently long for the convection to appreciably influence the mass transfer. As shown in Figures 29 through 34, the calculations did show development of a circular roll cell, similar in appearance to a smoke ring. This agrees with the steady state results calculated by Suriano, Yang and Donlon (8) for a heated vertical plate

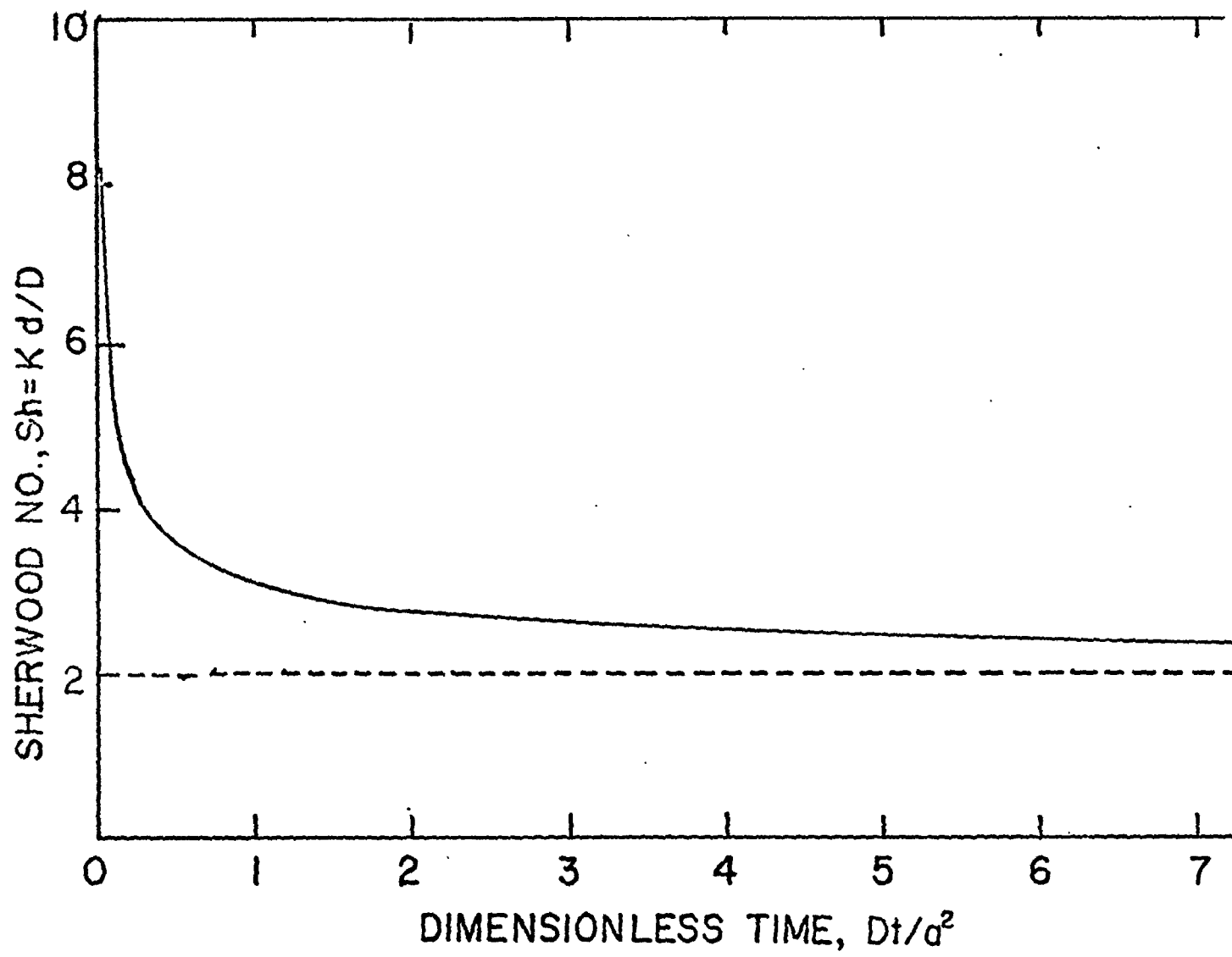


Figure 28. Sherwood number for transient convectionless diffusion from a sphere

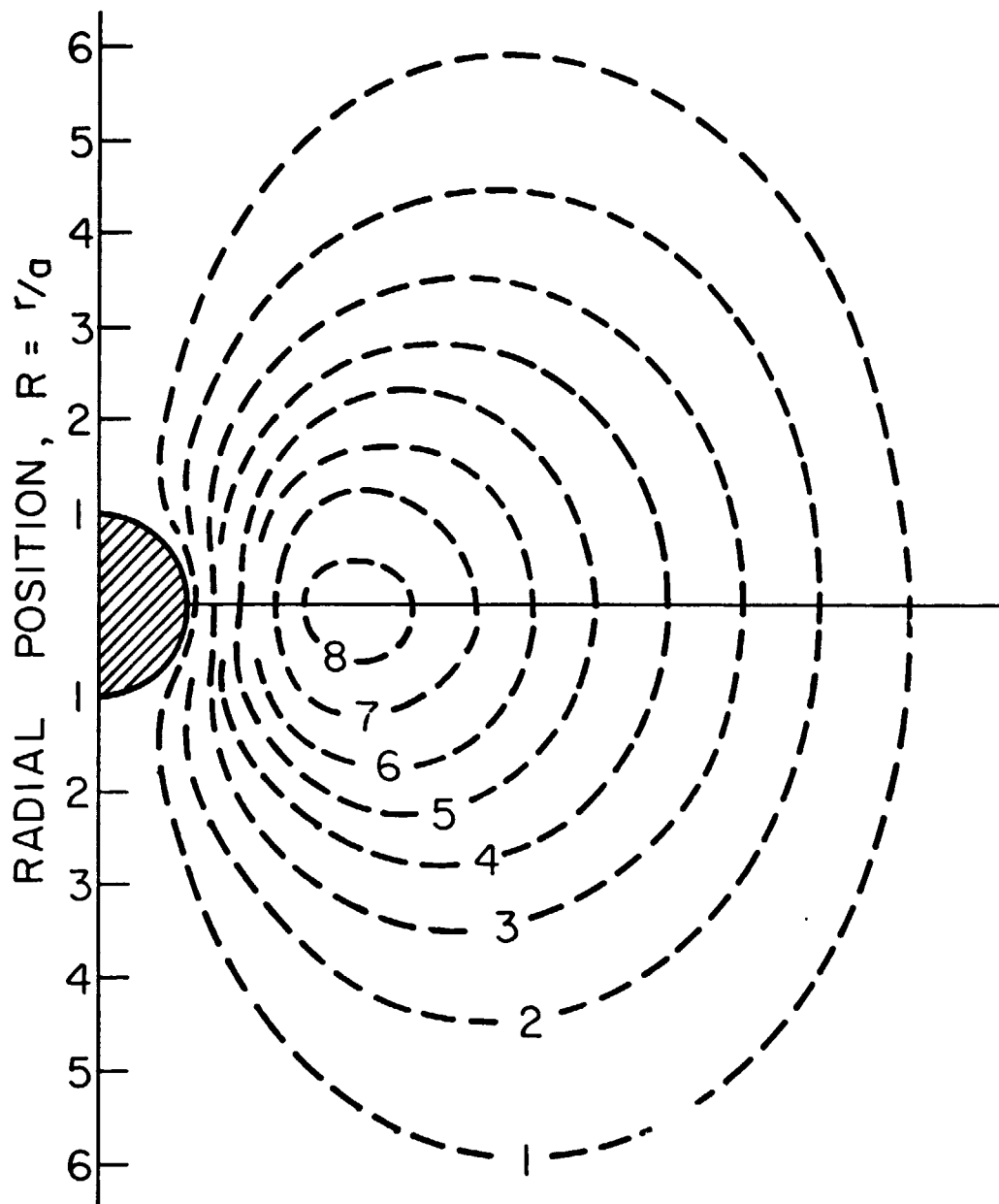


Figure 29. Streamlines at  $\tau = 1.24$  for  $Gr = 7.9$  and  $Sc = 465$  about a growing sphere. Values on curves are  $10^3 \psi$ . For 1 cm diameter sphere and dilute aqueous solution corresponds to 31 seconds after beginning of growth.



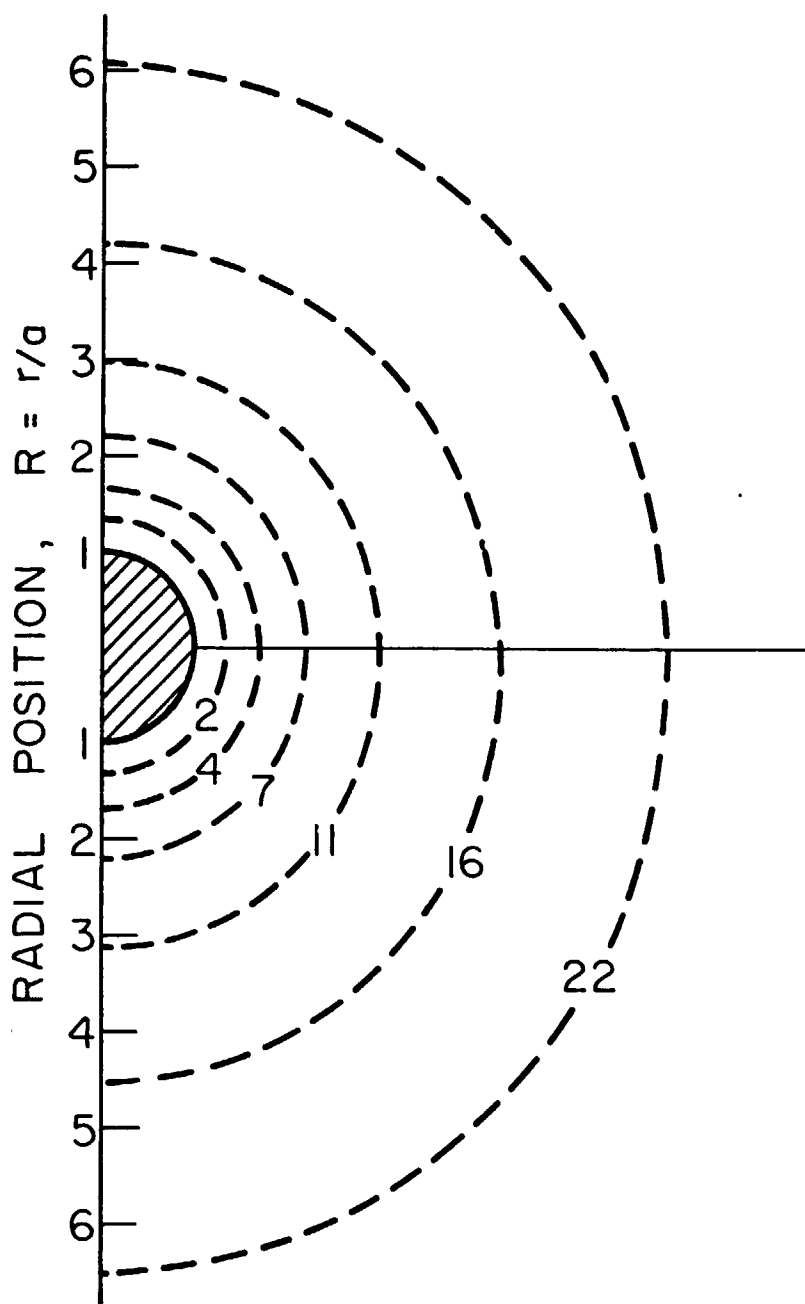


Figure 30. Constant concentration curves at  $\tau = 1.24$ . Values on curves are  $-\log \phi$ .

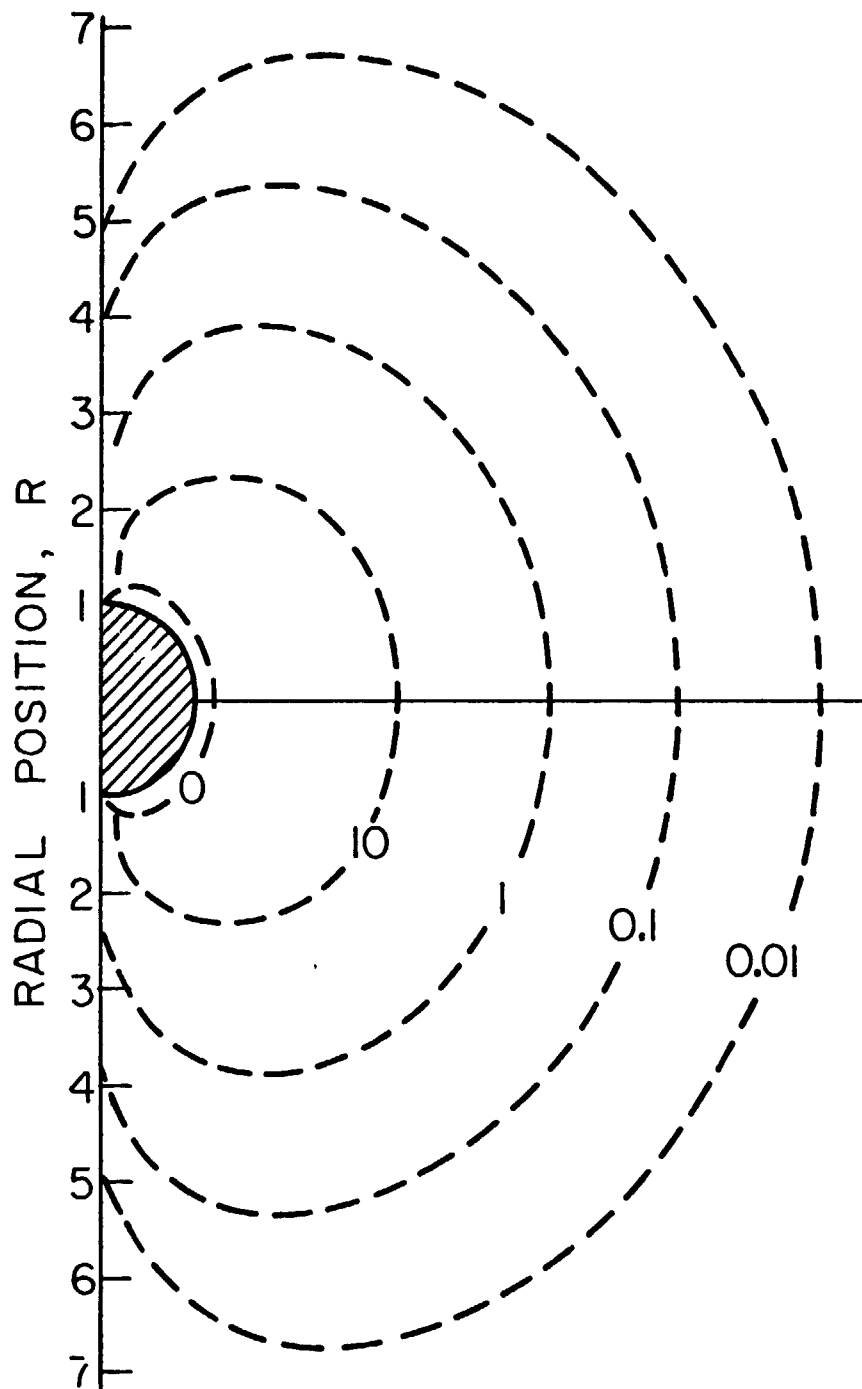


Figure 31. Constant vorticity curves at  $\tau = 1.24$ . Values on curves are  $10^4 \omega$

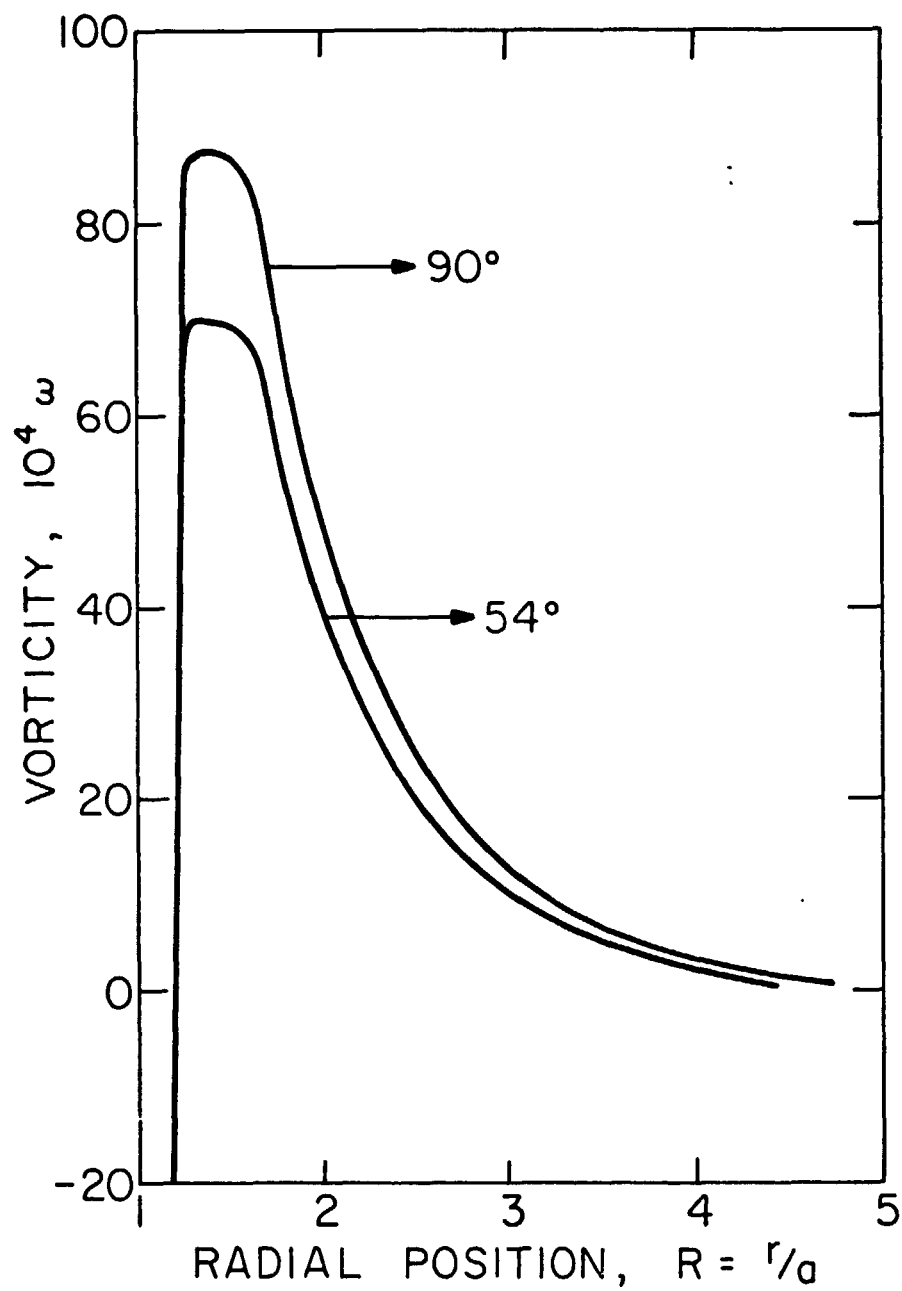


Figure 32. Vorticity as a function of radial position at  $54^\circ$  and  $90^\circ$  from vertical for  $\tau = 1.24$ .

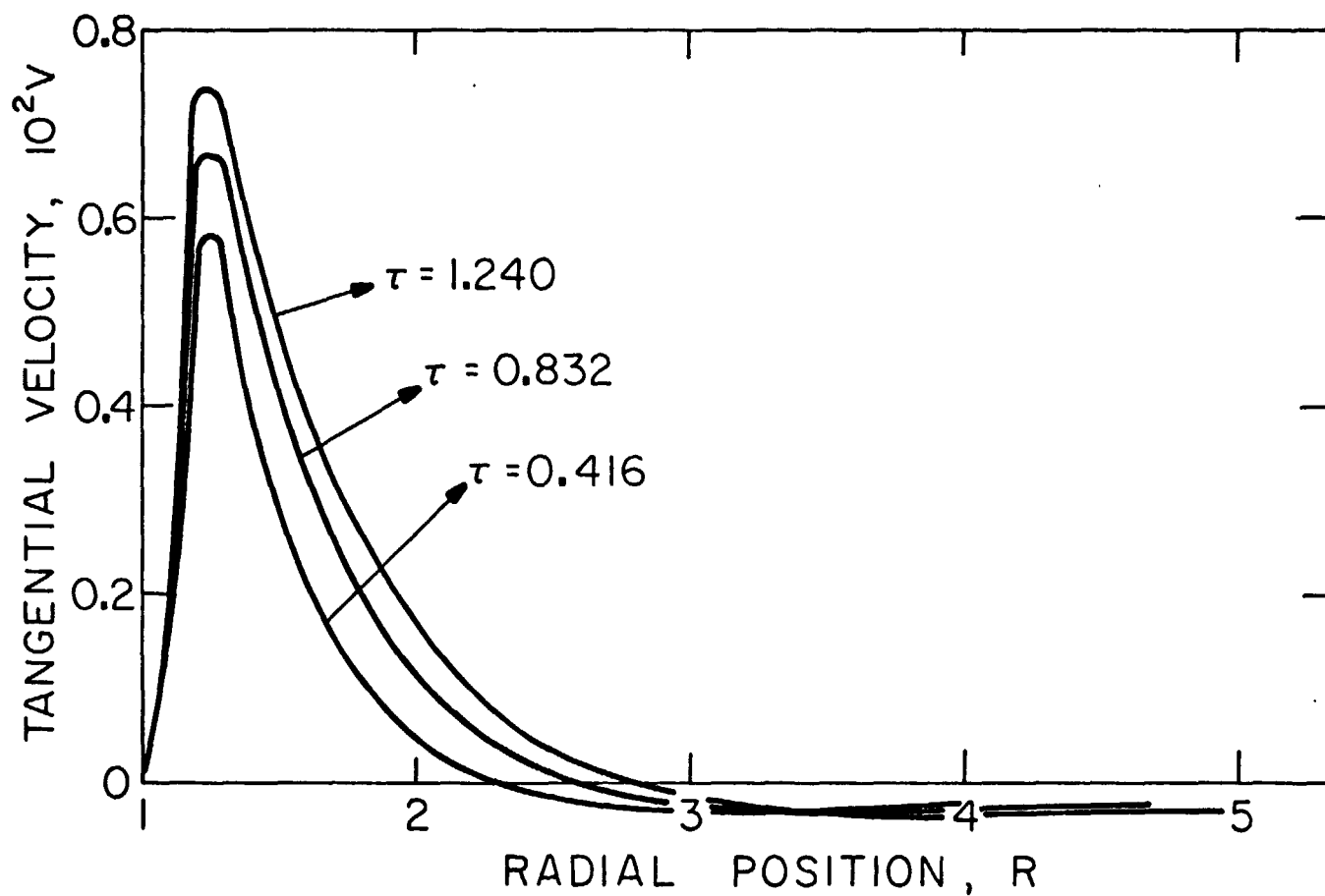


Figure 33. Tangential velocity at  $\theta = 90^\circ$  as a function of radial position for three times. For 1 cm diameter sphere and a dilute aqueous solution a value of  $V = 0.01$  corresponds to about 0.002 mm/second = 7.2 mm/hour.

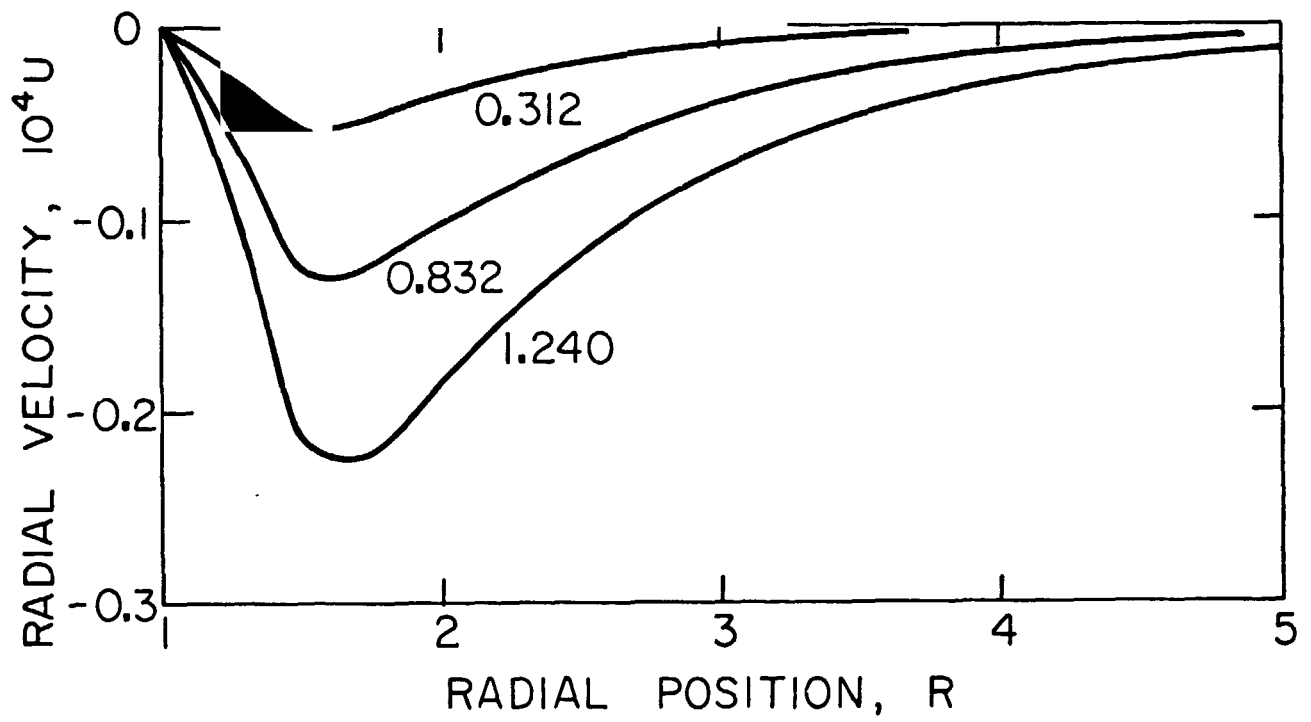


Figure 34. Radial velocity at  $\theta = 90^\circ$  at three times.

with a Prandtl number\* of 10 and Grashof numbers of 0.5 and 1.0, and by Hassain and Gebhart (9) for a heated sphere with a Prandtl number near 1 and Grashof numbers of up to 0.7.

---

\*The Prandtl number plays the role in heat transfer that the Schmidt number plays in mass transfer.

#### IV. EXPERIMENTAL SIMULATION OF CRYSTALLIZATION IN A LOW G SPACECRAFT ENVIRONMENT

(P. J. Shlichta and P. S. Chen)

##### Definition of Symbols

$C_c$	Solute molar concentration in crystal, moles/cm <sup>3</sup>
$C_p$	Heat capacity of solution, erg/g <sup>o</sup> K
$D$	Solute diffusion coefficient in solution, cm <sup>2</sup> /sec
$g$	Acceleration, cm/sec <sup>2</sup>
$g_e$	Earth's gravitational acceleration, 980 cm/sec <sup>2</sup>
$Gr_h$	Grashof number for temperature differences, $L^3 (\partial\rho/\partial T) (T_o - T_\infty) g / \rho v^2$
$Gr_m$	Grashof number for composition differences, $L^3 (\partial\rho/\partial W) (W_o - W_\infty) g / \rho v^2$
$h$	Heat transfer coefficient between crystal and bulk solution, erg/cm sec <sup>o</sup> K
$\Delta H_c$	Heat of crystallization, erg/g
$k$	Thermal conductivity of solution, erg/cm sec <sup>o</sup> K
$K$	Mass transfer coefficient, cm/sec
$L$	Width or diameter of crystal, cm
$M_A$	Molecular weight of solute, g/mole
$(n_A)_o$	Mass flux of solute into crystal, g/cm <sup>2</sup> sec
$(n_B)_o$	Mass flux of solvent into crystal, g/cm <sup>2</sup> sec
$Nu$	Nusselt number, $hL/k$ . Also, dimensionless temperature gradient at crystal surface.
$Pr$	Prandtl number, $\nu\rho C_p/k$
$s$	Parameter dependent on $(Sc/Pr)$ , from Ref. (11).
$Sc$	Schmidt number, $\nu/D$ .

Sh	Sherwood number, $KL/D$ . Also, dimensionless concentration gradient at crystal surface.
T	Temperature, $^{\circ}K$ .
$V_c$	Linear crystal growth rate, cm/sec.
$W_o$	Mass fraction solute at surface of crystal.
$W_{\infty}$	Mass fraction solute initially in bulk solution.
$\alpha$	$(\partial\rho/\partial W)/\rho$
$\beta$	$(\partial\rho/\partial T)/\rho$
$\nu$	Kinematic viscosity, $cm^2/sec$ .
$\rho$	Density of solution, $g/cm^3$
$\rho_c$	Density of crystal, $g/cm^3$
$\Delta\rho_W$	Change in density due to composition change, $g/cm^3$
$\Delta\rho_T$	Change in density due to temperature change, $g/cm^3$

#### A. Purpose and Scope

The objectives of this portion of the program are a) verification of the theoretical predictions of Section III by observation of the growth (or dissolution) rate and convection around suspended crystals or polycrystalline spheres at low Grashof numbers, and b) observation of crystal growth phenomena at low Grashof numbers for the purpose of predicting the feasibility, advantages, and problems of growing crystals in a spacecraft environment, with particular emphasis on the effect of convection and/or accelerational transients on the formation of crystal defects.



These goals are to be accomplished by the study of so-called low-gravity-simulation (LGS) systems--solute-solvent pairs in which the heat of crystallization and the change of density with concentration are both small. We had previously demonstrated that for a given crystal size and growth rate, LGS systems crystallize at 1 g much as normal solution systems would crystallize in a spacecraft environment (10). These systems are being studied by the use of schlieren and other optical techniques to observe the steady-state and transient convection patterns around growing or dissolving crystals and the change of size (or weight) of these crystals as a function of time. Some attention may also be given to the correlation between the convective history and the location of defects in the grown crystal.

The objectives may be restated as the following specific tasks.

- 1) Search for, verification, and characterization of LGS systems.
- 2) Development and refinement of optical apparatus and experimental techniques.
- 3) Observation of the dissolution and growth of polycrystalline spheres, immersed in a uniform static solution, by measurement of size and/or weight change versus time, time lag for onset of convection, and qualitative steady-state convection pattern.
- 4) Extension of 3) to include mapping of flow velocity and concentration gradient patterns as a function of time.
- 5) Repetition of 3) and 4) using single-crystal spheres, with special attention to the flow perturbations arising as the growing crystal changes from a spherical to a faceted shape.

6) Experiments similar to 3) and 4) in which the suspended sphere is replaced by a large flat plate.

7) Qualitative observations of the flow pattern around a suspended growing faceted crystal with special attention to the possible development of spontaneous transients and their correlation with the development of crystal defects.

8) Extension of some or all of the above to include Grashof-number transients, induced by accelerational or forced-convection pulses.

9) Low Grashof-number crystal growth under steady-state forced convection.

It is expected that during the present contract activities will be confined to tasks 1), 2), 3), 4) and possibly 7).

#### B. Low-Gravity-Simulation Systems

The principal effect of gravity upon crystallization is the development of free convection currents around the growing crystal. The process of crystallization can change the density of the surrounding fluid in two ways:

a) by removing solute from the fluid, thereby changing the latter's composition, and

b) by absorbing or emitting heat into the fluid, thereby changing its temperature.

For either or both of these reasons, the density of the surrounding fluid is, in almost all cases, reduced and a rising convection current is established around the growing crystal.

The most commonly used index of the degree of free convection in a system is the Grashof number, which is the ratio between the buoyant and viscous forces in a system. If we consider only composition differences, the Grashof number can be defined as:

$$Gr_m = \frac{L^3 \left( \frac{\partial \rho}{\partial W} \right) (W_o - W_\infty) g}{\rho \nu^2} \quad (6)$$

where

$L$  = the "characteristic length" of the system, here assumed to be the diameter of the sphere or crystal.

$\partial \rho / \partial W$  = the change of solution density with concentration (solute mass fraction) in the vicinity of saturation.

$W_o$  = the solution concentration (solute mass fraction) at the surface of the crystal, assumed to be equal to the saturation concentration.

$W_\infty$  = the bulk solution concentration.

$g$  = gravitational (or centrifugal) acceleration

$\rho$  = the density of the solution

$\nu$  = the kinematic viscosity (viscosity/density) of the solution.

It is obvious that, all quantities except  $g$  being held constant, the transfer of a crystallizing system from the earth's surface to a spacecraft environment has the effect of reducing the system's Grashof number by several orders of magnitude. It is also evident that alternatively one might reduce the Grashof number--and therefore, hopefully, simulate spacecraft-environment crystallization--by

- a) reducing the size of the system (L),
- b) reducing the supersaturation ( $W_{\infty} - W_0$ ) and, therefore, the growth rate,
- c) increasing the viscosity ( $\nu$ ), or
- d) decreasing  $\partial\rho/\partial W$ .

From a purely fluid-mechanics viewpoint, all of these changes would be equivalent. Unfortunately, the process of crystallization involves several size-dependent parameters, such as growth step height and the ratio of surface energy to bulk energy, so that microscopic crystallization at  $1 g_e$  is probably not a valid simulation of macroscopic low-gravity crystallization. Crystallization also involves supersaturation-dependent phenomena, such as growth step nucleation and surface diffusion, so that the extremely slow growth of crystals at very low supersaturations is a questionable simulation of faster growth at low-gravity. Finally, order-of-magnitude increases in viscosity cannot be effected without substantial amounts of macromolecular additives which, as the sad history of attempts to grow crystals from gels attests, create problems of their own. Therefore, it would appear that most reliable simulation of low-gravity crystallization would be attained by using solution systems in which the change of density with solute concentration approaches zero.

We have thus far neglected temperature differences, for which the Grashof number is defined as

$$Gr_h = \frac{L^3 \left( \frac{\partial \rho}{\partial T} \right) (T_0 - T_{\infty}) g}{\rho \nu^2} \quad (7)$$

in which  $\partial\rho/\partial T$  is the change of solution density with temperature and  $T_0$  and  $T_\infty$  are the temperatures at the growth interface and in the bulk solution. We can estimate the relative driving forces of heat- and mass-transfer by examining very slow transport from a planar surface. At steady state the rate of latent heat liberation,  $V_c \rho_c \Delta H_c$ , must be equal to the heat flux back into the solution,  $h(T_0 - T_\infty)$ , where  $V_c$  is the linear crystal growth rate,  $\rho_c$  is the density of the crystal, and  $h = kNu/L$  is the heat transfer coefficient. The growth rate in turn is given by

$$V_c C_c = K \frac{\rho_f}{M_A} \frac{W_\infty - W_0}{1 - W_0 \left[ (n_A + n_B)/n_A \right]_0} \quad (8)$$

where  $C_c$  is the molar solute concentration in the crystal,  $K = DSh/L$  is the mass transfer coefficient without interfacial flow,  $\rho_f$  is the density of the fluid,  $M_A$  is the molecular weight of the solute, and  $(n_A)_0$  and  $(n_B)_0$  are the mass fluxes of solute and solvent into the crystal from the solution. For a solvent-free crystal,  $C_c = \rho_c/M_A$  and  $(n_B)_0 = 0$ . Inserting Eq. (8) into the steady state heat balance we obtain for a solvent-free crystal

$$h(T_0 - T_\infty) = V_c \rho_c \Delta H_c = K \rho_f \Delta H_c (W_\infty - W_0)/(1 - W_0) \quad (9)$$

The ratio of the density change due to the compositional change to that due to the temperature change is therefore,

$$\frac{\Delta \rho_w}{\Delta \rho_T} = \frac{\alpha (W_o - W_\infty)}{\beta (T_o - T_\infty)} = \frac{Gr_m}{Gr_h} = \frac{\alpha}{\beta} \frac{h(1-W_o)}{k \rho_f \Delta H_c} \quad (10)$$

From Ref. (11) we note that

$$Sh = Nu/s \approx Nu/0.737 (Pr/Sc)^{1/3}, \quad (11)$$

and this with the definition of Sh and Nu gives

$$\begin{aligned} \frac{h}{K} = \frac{k}{D} &\approx \rho_f C_p \frac{Sc}{Pr} (0.737) \left( \frac{Pr}{Sc} \right)^{1/3} \\ &= 0.737 \rho_f C_p (Sc/Pr)^{2/3} \end{aligned} \quad (12)$$

Substituting this into Eq. (10) we obtain

$$\frac{Gr_m}{Gr_h} = 0.737 \frac{\alpha}{\beta} \frac{C_p}{\Delta H_c} \left( \frac{Sc}{Pr} \right)^{2/3} (1-W_o) \quad (13)$$

Taking  $C_p = 1 \text{ cal/g}^\circ\text{C}$  and  $(Sc/Pr) = 140$ , we obtain for  $(CH_3)_4NCl/H_2O$  (a typical LGS system with a  $\Delta H$  of  $2.4 \text{ cal/g}$ )  $Gr_m/Gr_h \approx 270$ , showing that the density change due to thermal effects is negligible. However, the ratio of the driving forces due to compositional and thermal effects is, from Eq. (13) and Ref. (11),

$$\begin{aligned} \frac{sGr_m}{Gr_h} &\approx (0.544) \frac{\alpha}{\beta} \left( \frac{Sc}{Pr} \right)^{1/3} \frac{C_p}{\Delta H_c} (1-W_o) \\ &\approx 38 \text{ for } (CH_3)_4NCl/H_2O. \end{aligned} \quad (14)$$

Therefore, although the Grashof number for the temperature difference is estimated to be much less than the Grashof number for the composition difference, it might have some adverse effect on the simulation of extremely low-gravity crystallizations. It is therefore desirable to choose LGS systems for which  $\Delta H_c$  is as small as possible. Also it is obvious that the simulation of growth from melt at low-gravity is unfeasible, since the  $\Delta H$  of melting is always considerable.

Preliminary experiments, reported elsewhere (10), disclosed that the tetramethylammonium chloride/water system, because of its extremely low  $\partial\rho/\partial W$ , low  $\Delta H$ , and high viscosity, appeared to be a valid LGS system. Unfortunately, its extreme hygroscopicity and tendency toward dendritic growth made further research with this system unattractive.

Accordingly, at the beginning of the present contract, a literature search was initiated to find other LGS systems, using the following criteria:

1. The change of solution density with increasing solute concentration, in the vicinity of saturation, must be as close as possible to zero. This is equivalent to requiring that the density of the solvent equal the density of the dissolved solute and is approximately equivalent to requiring that the solvent and solid solute have the same density. Accordingly, the latter requirement was used in searching for candidate solute-solvent pairs.

2. The system must have a low heat of crystallization. It is still not certain how strict this requirement must be.

3. The system must yield good equidimensional single crystals. (Our early fears--that all LGS systems would tend toward dendritic crystallization--were rapidly dispelled.)

4. The solute must melt well above room temperature and have a low vapor pressure.

5. The solvent must boil far above room temperature and have the lowest possible vapor pressure, so as to minimize the likelihood of evaporative nucleation at the surface of the solution.

6. Both solvent and solute must be stable and substantially nontoxic with regard to prolonged exposure to vapor and occasional skin contact.

7. The room-temperature solubility should be greater than about 0.05 weight fraction, to permit reasonable growth rates, and less than about 0.20 to facilitate comparison with theory. Also, solubility should increase with temperature, so as to facilitate the preparation of supersaturated solutions.

8. Ideally, the solvent should be a variable mixture of two chemically similar compounds of slightly different density, such as  $H_2O-D_2O$ . This permits the variation of  $\partial\rho/\partial W$ , so that the Grashof number of the system can be "tuned" to zero or very low values.

9. The system should possess one or more of the following characteristics to facilitate measurement of the convection and/or solute concentration around the growing crystal:

a) A strong variation of index of refraction with concentration so as to permit observation by schlieren methods.



b) A "window" in the visible region wherein the solvent is transparent and the solute moderately absorbent ( $\alpha \approx 0.1 \text{ cm}^{-1}$ ) so as to permit absorption spectrophotometry.

c) Electrical conductivity and electrolyzability, so that convection can be visualized by the generation of minute hydrogen bubbles (12).

10. Both solvent and solute should be readily available and reasonably inexpensive.

A previous search--which eventually uncovered the tetramethylammonium chloride/water system--was believed to have exhausted the likelihood of finding a water-soluble inorganic salt with a density near 1.0. Therefore, the present search was confined to organic solutes and solvents. This was also advantageous since the heat of crystallization is usually small in organic systems. There is, unfortunately, no published tabulation of organic compounds according to density. Therefore, our search commenced with the compilation of such a tabulation from standard organic compendia (13,14). This compilation (Table III) is by no means complete or systematic, since on the one hand we first considered standard solvents and solutes which were known to crystallize well, and on the other hand we rejected any compound which failed to satisfy criteria 3), 4) or 5) by having an unsuitable melting point, boiling point, or crystal habit. (Many solutes, for example, were rejected because they were known to crystallize as needles.) This phase of the search is by no means complete and it will eventually be resumed.

TABLE III. SUITABLE SOLVENTS AND SOLUTES TABULATED ACCORDING TO DENSITY

Solvent	Density (g/cm <sup>3</sup> )	Solute
	0.70	
		ether
	0.75	
		dodecane
allylamide, n-butyl ether		
acetonitrile		
methanol, ethanol, acetone	0.80	
(sec)-butyl alcohol, allylether, acrylonitrile		
kerosene		
acetal		
	0.85	
allyl alcohol, (sec)-butyl benzene		
p-tert-butyl-toluene, toluene		
benzene		
2-butoxyethanol, ethyl acetate, xylene	0.90	acenaphthylene
allyl-chloride, 2-butoxyethyl acetate		
benzyl-ethyl-ether, 2-amino-1-butanol	0.95	
butyric acid		
ethyl carbonate, acetylacetone, acetonylacetone		camphor
		thymol

(continued)

TABLE III. (Continued)

Solvent	Density (g/cm <sup>3</sup> )	Solute
water, anisole	1.00	
carbitol acetate		borneol, methyl-hydroxylamine
2-aminoethanol		
acetophenone, m-cresol		
benzaldehyde, benzyl alcohol, acetic acid	1.05	
benzyl acetate		
acrylic acid, aniline acetate		phenol
benzyl formate	1.10	
acetyl chloride, acetaldol		
benzyl benzoate, anise alcohol, p-anisoaldehyde		benzophenone
		1-naphthylamine, 2-naphthylamine
	1.15	
		acetamide
		naphthalene
		acenaphthene
	1.20	
		acetamilide, allylthionrean
	1.25	cinnamic acid
glycerin		anthracene
1-bromobutaml		

(continued)

TABLE III. (Continued)

Solvent	Density (g/cm <sup>3</sup> )	Solute
carbon-disulfide	1.30	
		benzamilide, benzoquinone
1-bromo-1-butane		
1-bromo-2-butane		
	1.35	benzamide

Table III was then inspected for possible solute-solvent pairs which were tentatively accepted or rejected on the basis of toxicity, availability and solubility. When solubility data was unavailable, it was estimated on the basis of chemical similarity or analogy to known solubilities. Table IV lists some representative rejected systems together with the reasons for their rejection. Table V lists the systems which, after the first round of screening, appeared to be worth further study. Three of these candidate systems were then checked for solubility and for variation of density with concentration. A Westphal balance was used for the latter measurement. Known weights of solute and solvents were combined in varying proportions to provide a set of solutions of different concentrations. Solubility was estimated by adding small known weights of solute until apparent saturation was reached.

Density measurements for the first three candidate systems are shown in Figure 35. It will be noted that, of these, the thymol/ethyl carbonate system has a  $\partial\rho/\partial W$  of almost exactly zero. Moreover, the  $\partial\rho/\partial W$  of the other two systems is low enough to make them also potential candidates for low-Grashof-number investigations.

The crystallization form of these systems was investigated by preparing saturated solutions at elevated temperatures (e.g., 50°C) and then letting them cool slowly. The camphor crystallized out from ethyl carbonate solution as needles. Both thymol systems produced clear euhedral crystals up to 2 mm in diameter.

TABLE IV. UNACCEPTABLE LGS SYSTEMS AND REASONS FOR REJECTION

phenol:water - toxicity

citric acid:CCl<sub>4</sub> - toxicity and probable low solubility

borneol:3-butanoic acid - stench of solvent

benzoic acid:glycerin - poor crystal form and low solubility

terebic acid:butyl alcohol - unavailability of solute

acenaphthalene:O-xylene - poor crystal form (needles)

acenaphthalene:ethyl carbonate - poor crystal form (needles)

acrylic acid:aniline acetate - very low M.P. and instability

camphene:M-xylene - low M.P. of solute

TABLE V. POSSIBLE ACCEPTABLE LGS SYSTEMS

thymol:ethyl carbonate

thymol:acetylacetone

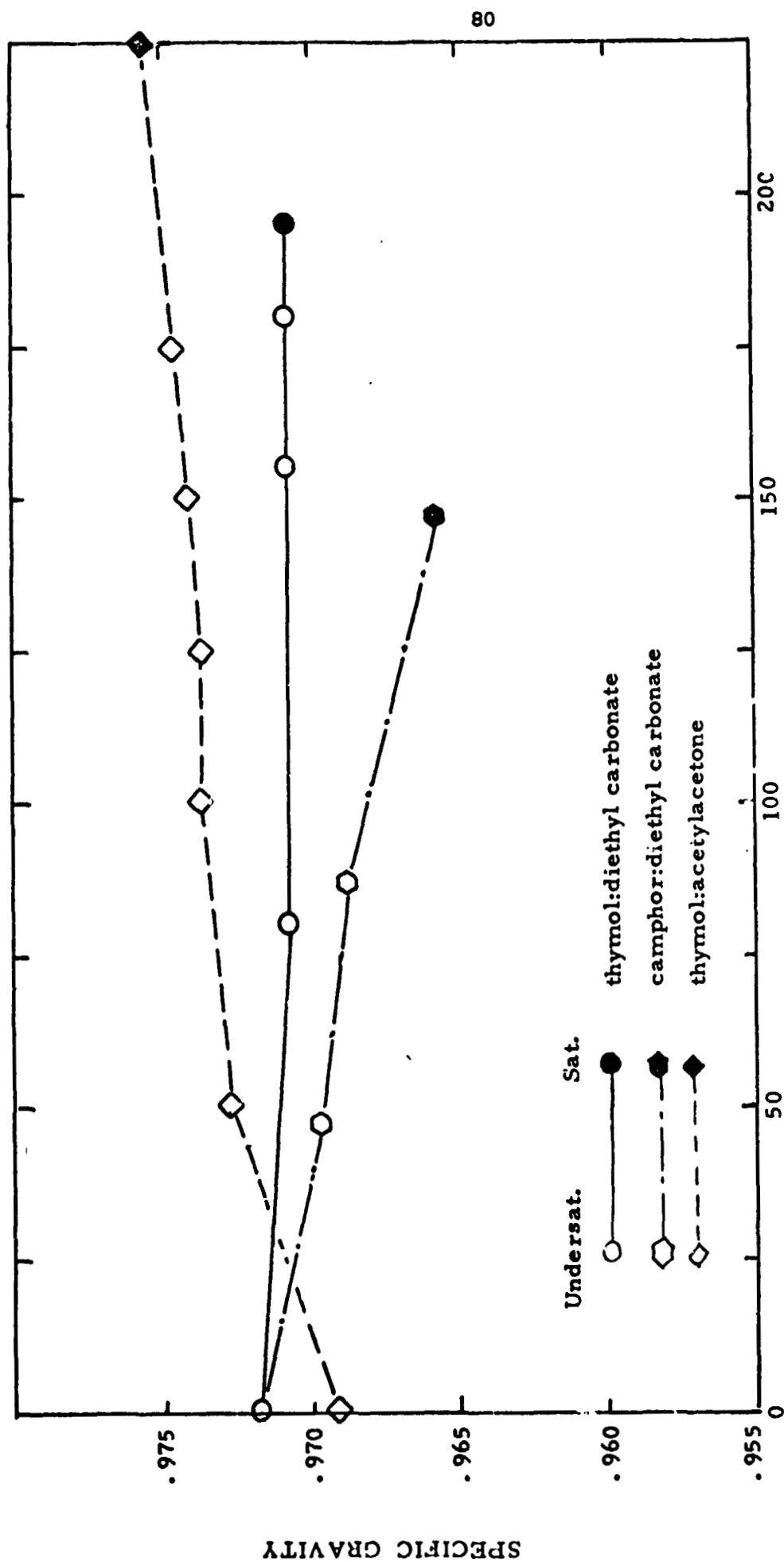
camphor:ethyl carbonate

borneol:anisole

borneol:carbitol acetate

$\beta$ -naphthylamine:benzyl acetate

methyl hydroxylamine:water (despite low M.P.)



CONCENTRATION, GRAMS PER 100 GRAMS SOLVENT

Figure 35. Density versus concentration of 3 cardate LGS systems

Therefore, despite their high solubility, which makes comparison with transport theory more difficult, and despite the rather high vapor pressure and potential low-level toxicity of the solvents, the thymol/diethyl carbonate and thymol/acetylacetone systems appear to be potentially suitable LGS systems. Thus far, growth and dissolution have been studied only in the thymol/diethyl carbonate system. The results of these tests will be discussed below.

#### C. Preparation and Characterization of Solutions

In order to calculate the Grashof number for a given crystallization it is necessary to know the density, viscosity, solubility, and change of density with concentration for the system at the temperature and concentration of crystallization. When the experiment involves a solution prior to or during crystallization, or when the possibility of convection due to heat transfer is considered, it is also necessary to know the density and solubility as a function of temperature. In addition, it is useful to know the index of refraction of the solution as a function of concentration and temperature. Refractive index measurements provide a rapid means of determining solution concentration and an easy method of determining solubility. Accordingly, the density, viscosity, and index of refraction of thymol/diethyl carbonate solutions are being determined as a function of concentration and temperature. The index of refraction (Figure 36) is determined by means of a Bausch and Lomb Abbé refractometer. The refractive index measurements are good to at least three significant



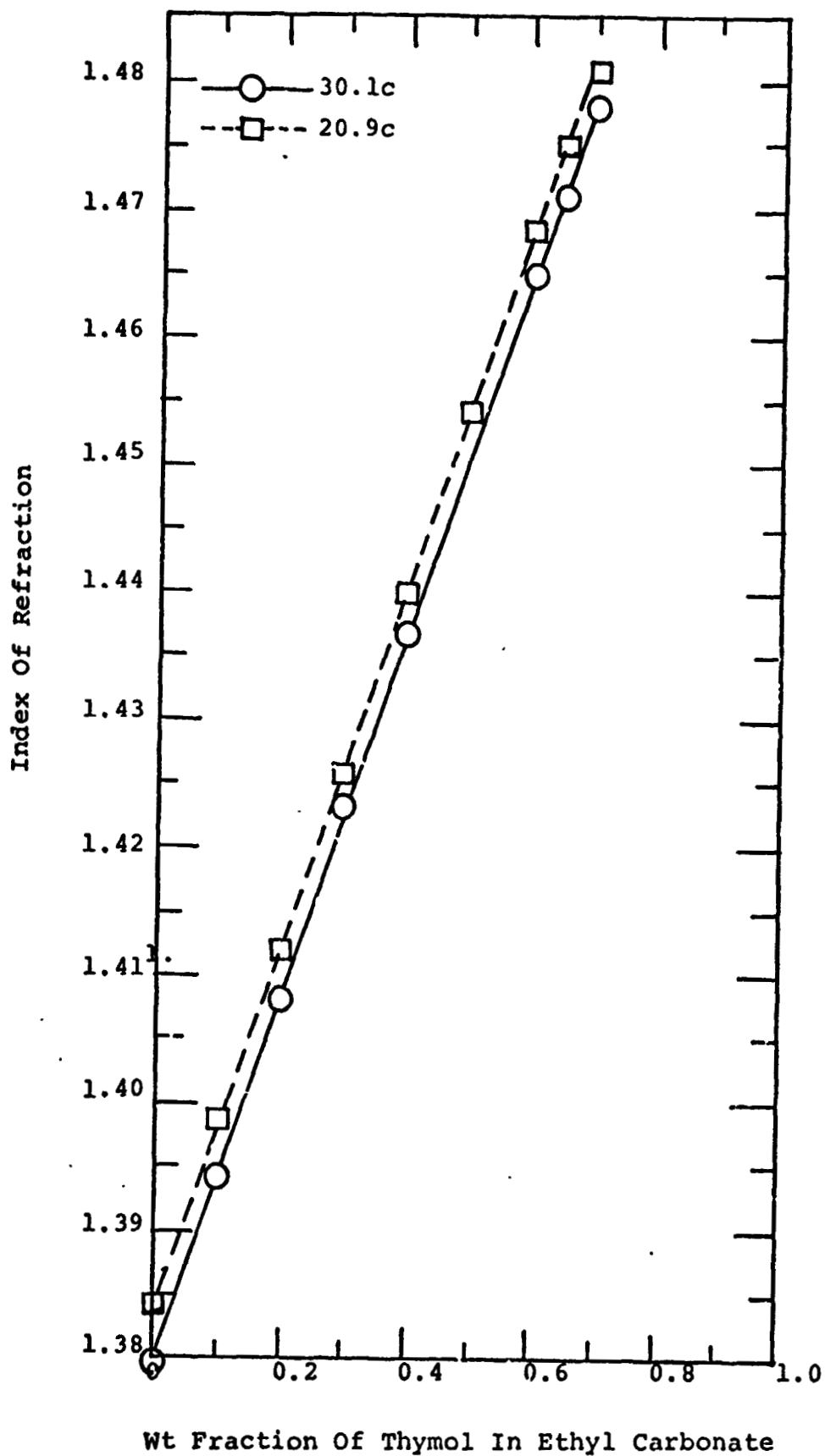


Figure 36. Index of refraction of thymol-diethyl carbonate solutions

figures. It will be noted that there is an appreciable increase in index of refraction with concentration, so that the system is shown to comply with criterion (9a). The viscosity (Figure 37) as measured by a U-tube capillary viscosimeter, depends strongly on both concentration and temperature. Attempts to measure density by using a Westphal-balance sinker on a precision microbalance led to unaccountably erratic results and these measurements were repeated using a pycnometer (Figure 38). At present, the solubility of this system is being determined as a function of temperature by equilibrating solutions with excess solute, determining the resultant index of refraction, and then extrapolating the data in Figure 36 to determine the saturation concentration. In making these measurements, as in the preparation of solutions for the first growth experiments, a difficulty was noted which is peculiar to LGS systems and which would also be encountered in spacecraft experiments. Normally, solutions are saturated by first dissolving as much solute as possible at a higher temperature and then cooling the solution to the final temperature where, in the presence of a few seed crystals of solute, excess solute crystallizes out. In ordinary solutions, the process of crystallization causes sufficient convection to mix the solution, so that storage at constant temperature for a few days to a week, with only occasional stirring or shaking, is sufficient to insure equilibration. In LGS systems, however, free convection is almost negligible and equilibration can be achieved only by stirring or shaking the solution continuously. This precaution is also necessary

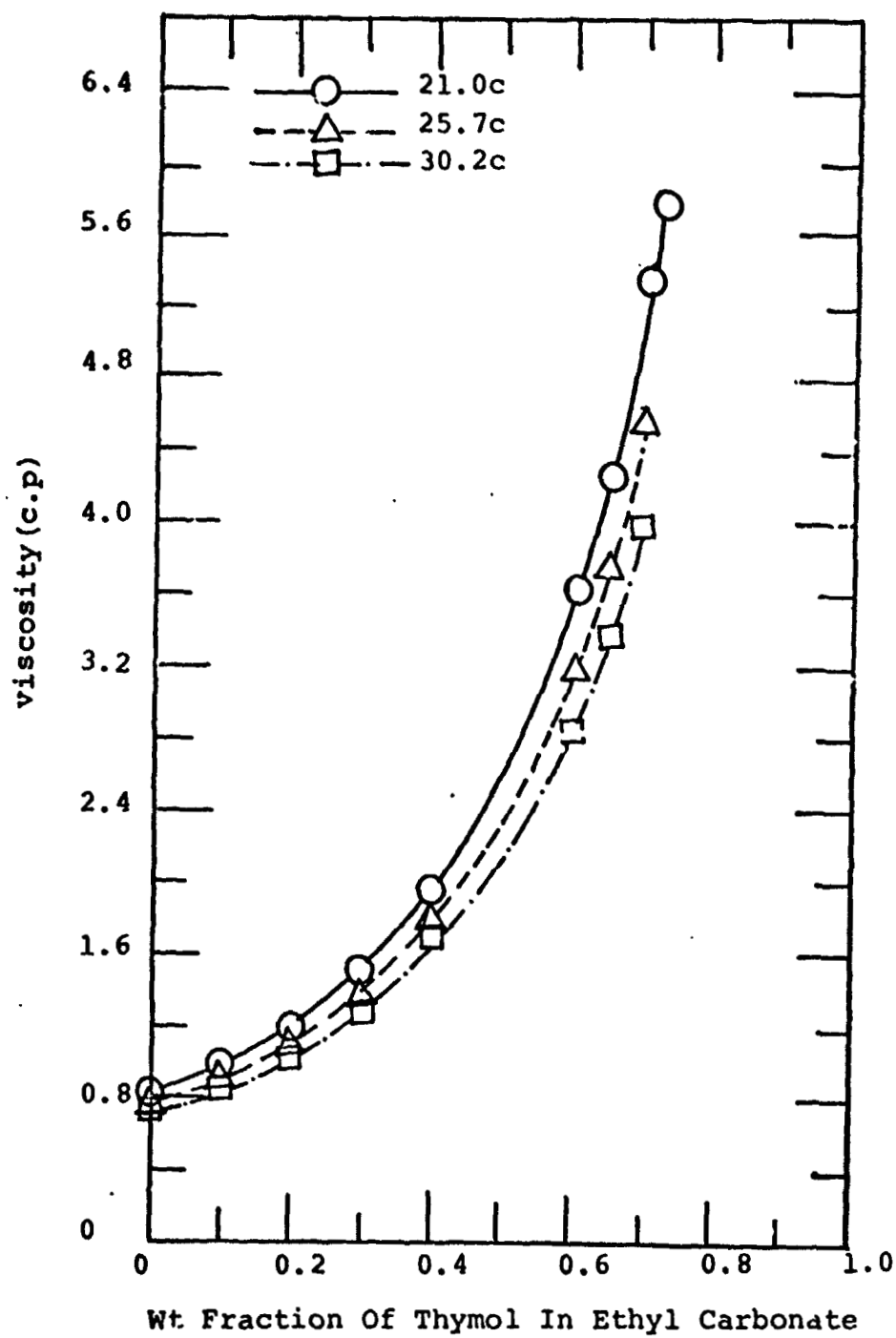


Figure 37. Viscosity of thymol-diethyl carbonate solutions at 21.0°C, 25.7°C, and 30.2°C.

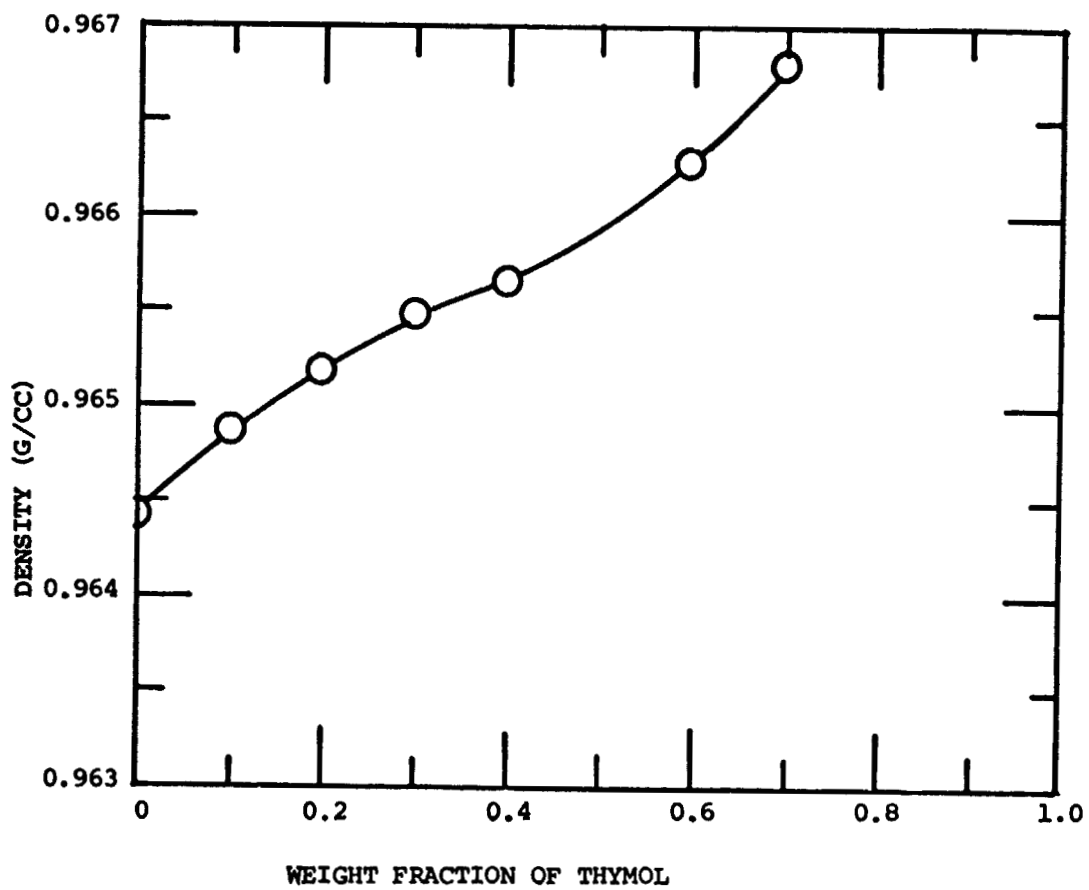


Figure 38. Density of thymol-diethyl carbonate solutions at 23.5°C

when determining the heat of solution, a measurement which is now being carried out on the thymol/diethyl carbonate system.

#### D. Preparation of Crystals and Polycrystalline Spheres

Thus far, the procurement of single crystals has presented no problem. Cubic cleavages of KBr and KCl, cleaved from melt-grown crystals, appear to be thoroughly satisfactory.  $\text{NaClO}_3$  crystals up to several centimeters on a side may readily be grown from solution. Thymol crystallizes so easily from melt or vapor that commercial material is often sold as single crystal lumps. Moreover, clear euhedral crystals can be grown from the LGS solution.

Polycrystalline spheres were produced by pressing powder between hemispherical steel dies. The original die design (1/2" hemispheres cut into 5/8" diameter rods as shown in Figure 39) resulted in equatorial ridges and stress concentrations which often caused the sphere to fracture into halves. The dies were then modified by enlarging the hemispherical surface to the same diameter as the rod and by cutting off the ends of the rods so that when the die rods barely touch, forming a spherical cavity, their ends are flush with the confining ring (Figure 40).

The spheres are prepared by pouring into the die chamber a weighed amount of powdered solute, corresponding exactly to the theoretical weight of a finished sphere. The upper die is then inserted and pressure gradually applied until an abrupt increase is

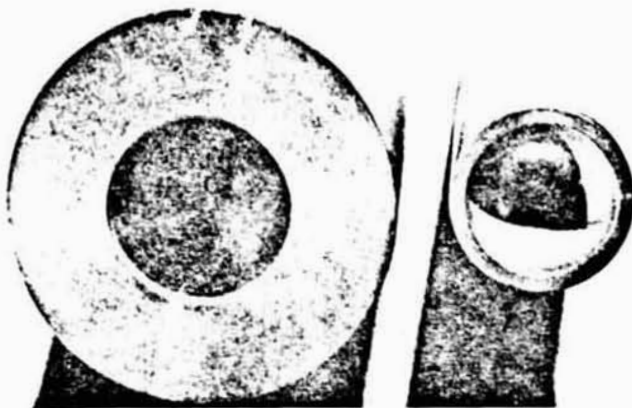


Figure 39. Original die for making polycrystalline spheres.

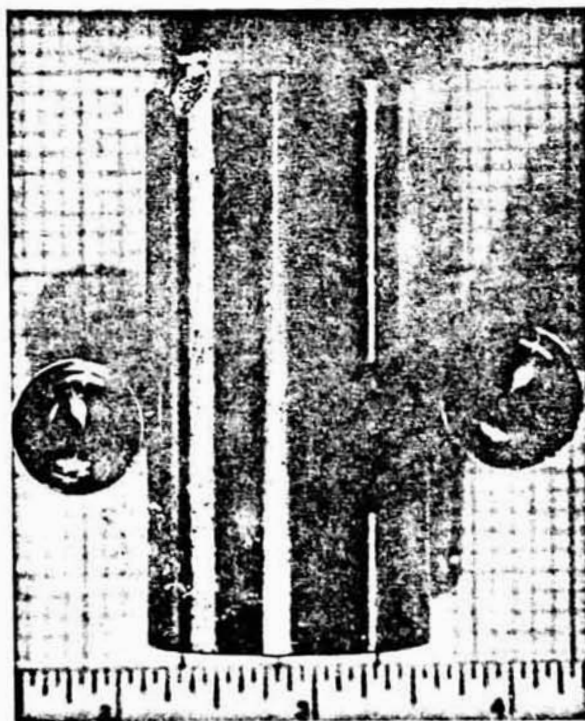


Figure 40. Improved dies for pressing polycrystalline spheres.

noted. (This indicates that the die rods are flush with the confining ring.) The pressure is maintained for about 5 minutes and then removed. The die rods are then pushed through the ring and pulled apart and the sphere is removed. It is sometimes advantageous to reposition the sphere between the dies and repeat the pressing operation several times; this produces a more symmetrical sphere.

In this manner, translucent coherent spheres of KBr, KCl,  $\text{NH}_4\text{Cl}$ , and camphor can be readily produced by room temperature pressing. Thymol is too brittle to press well at room temperature, but produces a coherent sphere at 45-50°C. Thymol also tends to adhere to the dies, so that the sphere has to be removed from between the die rods by gently heating them.

Crystals and spheres are usually mounted by drilling a #80 hole through them and then passing a fine wire through the hole. During growth and dissolution experiments, the wire is suspended horizontally across the center of the cell. Thymol crystals and spheres can also be mounted by melting them onto an electrically heated wire. In future experiments, the wire will sometimes consist of a chromel-alumel composite with a junction at the center or surface of the sphere and in some cases a second junction at the side of the cell, so that thymol gradients can be measured directly. Thus far, the only solute which has presented any difficulties is  $\text{NaClO}_3$ , which is too brittle to press or drill at room temperature.

### E. Optical and Photographic Apparatus

The preceding theoretical sections suggest that the most important observations during growth or dissolution would be of a) the average growth rate, as measured by the change of size or weight of the crystal as a function of time, b) the qualitative form of the convection pattern around the crystal, and c) the convective velocity, especially as a function of time. Similarly, the second objective of the experimental program could best be met by continuous observation of the convection pattern around a growing crystal. These requirements suggested time lapse schlieren photography as the technique of choice. Therefore most of our activities to date have been concerned with the assembly, testing and refinement of a 4-inch concave-mirror Töpler schlieren apparatus with attached time-lapse movie camera.

The Töpler schlieren method provides an image in which the brightness at each point corresponds to the magnitude and sign of the horizontal (or vertical) component of the index-of-refraction gradient. The apparatus is shown schematically in Figure 41. Light from a point source (A) is collected by a lens (B) and formed into a parallel collimated beam which passes through the sample cell (C) and through a second lens (D) which refocuses the undeviated light at point E. Here a knife edge cuts off part of the focused beam, thereby uniformly dimming the background of the image. Horizontal refraction gradients deviate the light to the left or right of the main focal point. Accordingly, these parts of the image appear either darker or lighter than the background. Thus, rising convection columns of lower density



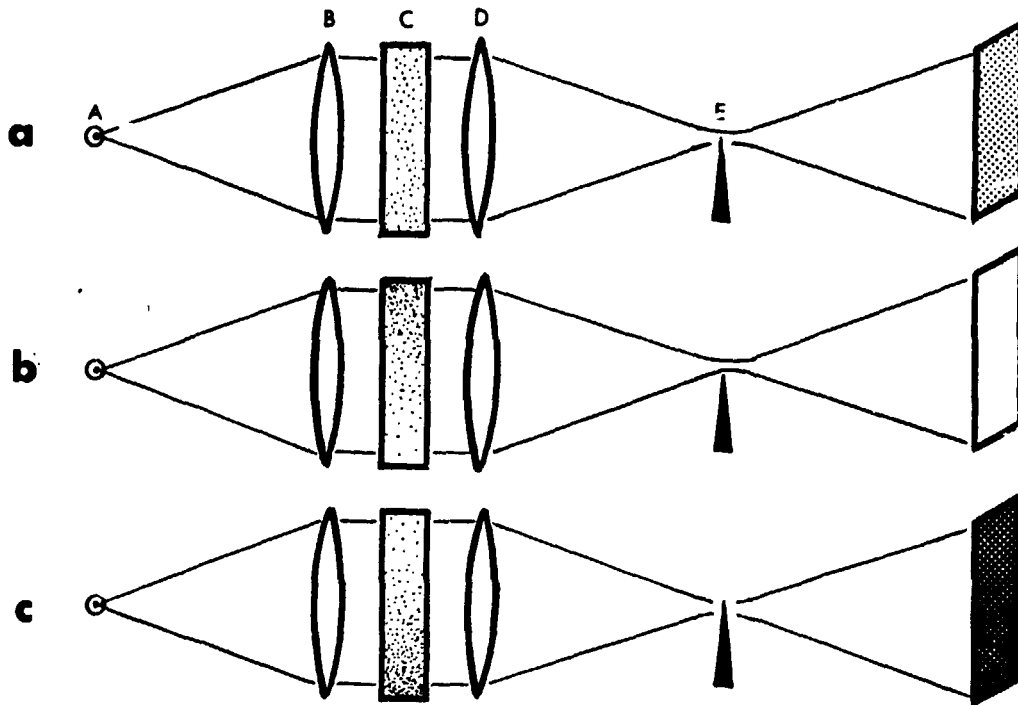


Figure 41. Diagram of Töpler schlieren apparatus.

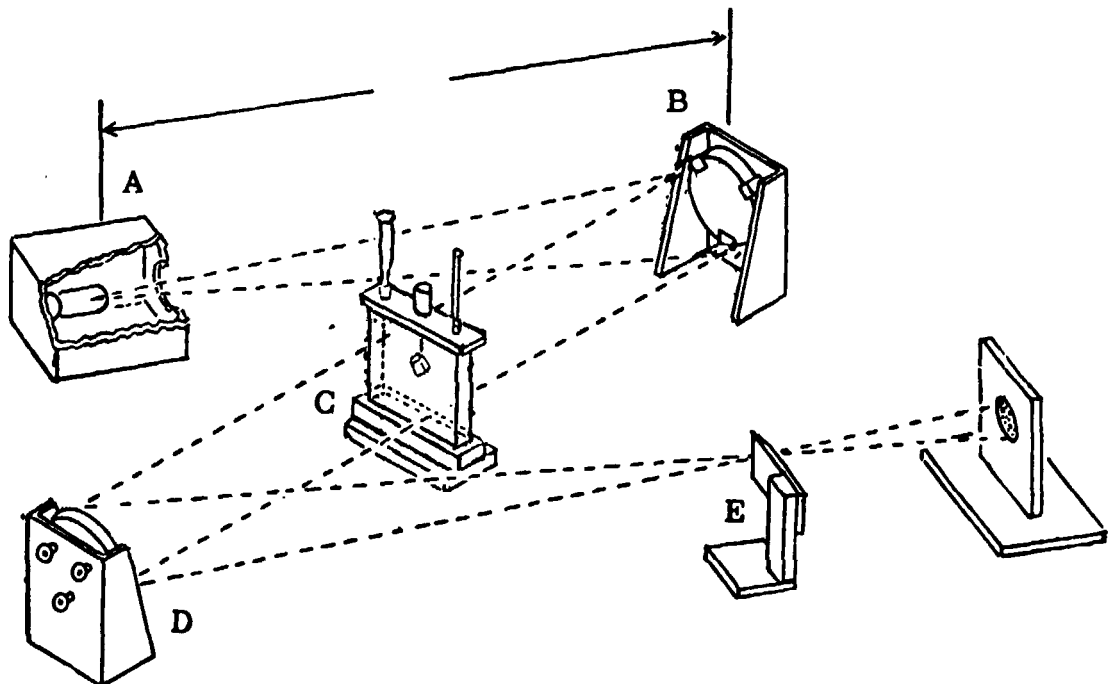


Figure 42. Sketch of mirror schlieren apparatus used at USC.

(and hence less refractive) fluid are revealed on the schlieren image by an apparent (but deceptive) three-dimensional relief. So it is seen that, in addition to providing a semiquantitative measurement of  $dn/dx$ , the schlieren technique is also a means of flow visualization and can be used to measure eddy velocities and similar phenomena. However, it does not provide any measurement of flow velocity, although it is fairly easy to incorporate a flow marking device into a schlieren apparatus. Moreover, a grid of opaque lines or dots may be introduced between B and C; the deviations of these grid points on the schlieren image may be used to provide an additional measurement of the index-of-refraction gradient. Finally, with the knife edge removed altogether, a sharp silhouette image results; this "shadowgraph" mode is very useful for measuring changes of size in the sphere or crystal.

In practice, in order to minimize chromatic and spherical aberration, concave mirrors are often used in place of lenses. A typical configuration of this type is shown in Figures 42 and 43. Ideally, to avoid astigmatism, B and D should be off-axis parabolic mirrors; these are unfortunately prohibitively expensive. The experiments described below were performed with an inexpensive (~ \$100) pair of 4-inch diameter 36-inch focal length telescope mirrors whose principal virtue was their availability.

The point light source (A) is a Sylvania concentrated-arc lamp (Model C-10) in which a tiny (0.4 mm mean diameter) brilliant (47 candles/mm) arc is maintained between a pointed rod and a concentric

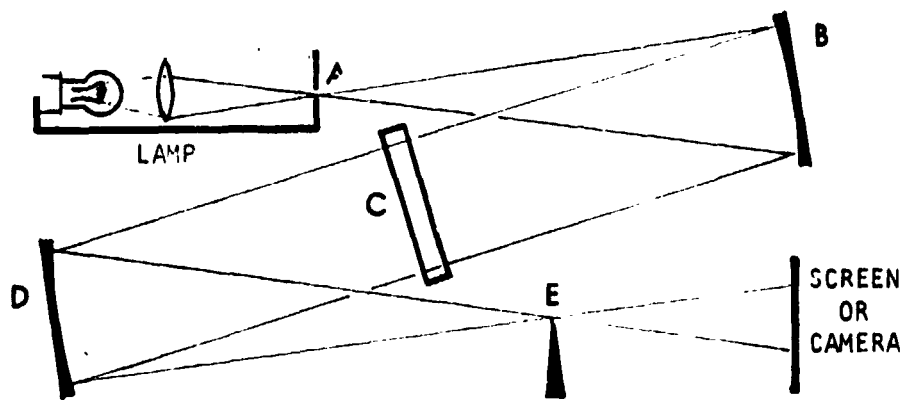


Figure 43. Alternative schlieren system using mirrors

ring of sheet zirconium. Although the arc can theory wander around the circle between the point and the ring, this has thus far caused no apparent difficulty. In all the crystallization experiments performed thus far, the lamp was used as the light source without any collimation or spatial filtering.

The chief disadvantage of this apparatus, as originally constructed, was its poor image resolution which, in the shadowgraph mode (with the knife edge removed) was no better than 0.5 mm; in the schlieren mode, it was somewhat worse (Figure 44). On the assumption that this was probably due to stray light from the arc lamp, a collimator was constructed whereby the arc image was projected, by means of two 2" diameter 8" focal length achromatic lenses, onto a pinhole positioned at point A. Using a homemade 0.6 mm diameter pinhole, the resolution was greatly improved (Figure 45) without substantial loss of image brightness. Although now adequate for our present needs, the resolution can presumably be improved further by using an even smaller pinhole. Arrangements have also been made to perform some experiments using a focused laser in place of an arc lamp; this will involve the use of a 4" achromatic lens schlieren apparatus which is now being constructed.

Another serious problem has been optical distortion from the solution cells. The plexiglas cells used in the previous experiments were shown to have numerous schlieren striae due to minute index-of-refraction variations in the superficially perfect plexiglas sheets used for their construction. Moreover, when these cells were filled with solution and inserted into the schlieren system, they shifted

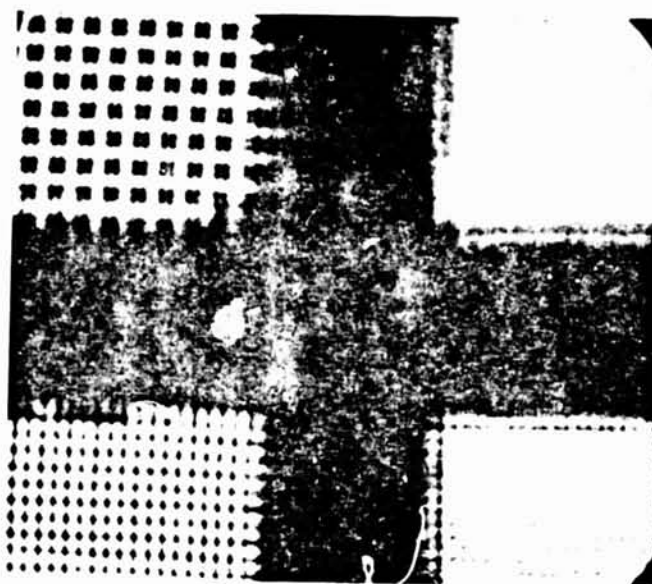


Figure 44. Resolution of schlieren system on wire screen targets without collimator (5X)

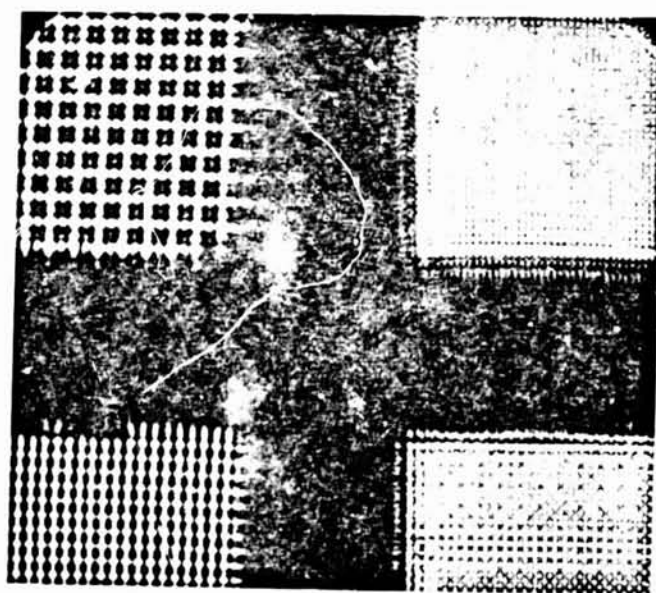


Figure 45. Resolution of schlieren system on wire screen targets with collimator (5X).

the focal point, indicating that the cell windows had a lens-like distortion.

Two sources of "schlieren free" plate glass were located and all-glass cells were constructed by joining edge-ground glass plates with epoxy cement. These cells, when inserted into the schlieren system, still show a few isolated schlieren striae (presumably due to compositional inhomogeneities) but are adequate for present use. Moreover, they cause no shift in the focal point of the system. Inquiries of vendors indicate that completely schlieren-free cells would cost several hundred dollars apiece, so that no further procurement is contemplated during the present contract. The epoxy cement used (Devcon "Two Ton"), although rated best for adhesion to glass, was slowly attacked and destroyed by the thymol/diethyl carbonate solutions. A series of trial experiments, using glued microscope slides soaked for days in various solvents, showed that Dow Corning Silicone Adhesive is the most adhesive and stable cement for our purpose.

Three modes of photographic data recording have been used (Figure 46):

a) Ordinary (lens focused) photography outside of or transverse to the schlieren apparatus (e.g., through the side walls of the solution cells). Various Polaroid or 35 mm cameras are available for this purpose. Our Bolex time-lapse movie camera has not so far been used for this purpose.

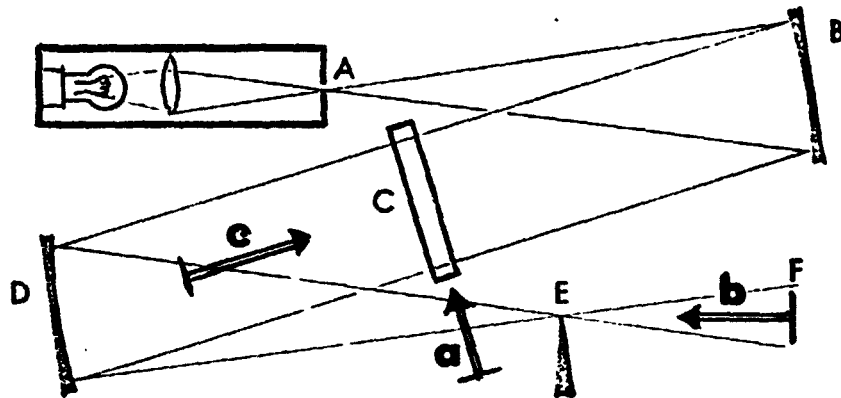


Figure 46. Modes of photography used with schlieren apparatus.

b) Schlieren and/or shadowgraph images can be taken with a lensless camera at any point beyond E. Since the magnification is a function of distance ( $M = (E-F)"/36"$ ), a moveable track has been constructed so that either overall views or closeups can be photographed. Two camera backs, a 35 mm Minoleta ST-102 (chosen for its ability to take precisely registered double exposures) and a Bolex 16 mm movie camera with automatic time-lapse, are interchangeable in this position.

c) Shadowgraphs at 1:1 magnification can be taken by inserting a camera back between C and D. Plans are now underway to record the dissolution of polycrystalline spheres using the 35 mm camera back in this mode while (between still photographs) the movie camera is used in mode b).

Other, non-photographic techniques are also available. For example, a strain-gauge microbalance is available for continuously recording the weight of the growing or dissolving crystal or sphere. This apparatus may be used in experiments on normal systems, such as KBr/water, but it is of very little value with LGS systems, in which the immersed crystals are practically weightless due to buoyancy.



## F. Experimental Results

Thus far, our principal concern has been with tasks (1) and (2), i.e., searching for and evaluating candidate LGS systems and developing necessary apparatus and techniques. Therefore, growth and dissolution experiments were performed primarily to test solution systems or apparatus rather than to obtain interpretable data. Nonetheless, preliminary experiments, which are summarized in Table VI, have yielded interesting results.

Dissolution of  $\text{NH}_4\text{Cl}$  Spheres: At the beginning of the program, it was observed that a polycrystalline  $\text{NH}_4\text{Cl}$  sphere, immersed in pure water, dissolved rapidly while the spherical form changed to a vertically elongated "nose cone" shape (Figure 47). Later photographs taken during the dissolution of an  $\text{NH}_4\text{Cl}$  sphere in a 90% saturated aqueous solution showed that the sphere gradually changed to a vertically elongated spheroid with an equatorial ridge (Figure 48). (The flat bottom is assumed to be due to the breaking away of a cracked portion of the sphere.) This observation is qualitatively consistent with theoretical expectations based on the assumption of downward flow, since the top and bottom of the sphere would be stagnation points while the maxima in both flow velocity and concentration gradient would be in the upper quadrant. We plan to repeat these experiments over a wide range of Grashof numbers with simultaneous photographs of profile and schlieren.

Dissolution and Growth of KBr: In experiment 40331A, a solution of KBr in water was saturated at  $30^\circ\text{C}$ , poured into a heated

TABLE VI. SUMMARY OF GROWTH AND DISSOLUTION EXPERIMENTS

No.	Experimental Conditions	Grashof Number	Mode of Observation	Remarks
40102	0.5" poly $\text{NH}_4\text{Cl}$ sphere dissolve in pure water at $22^\circ\text{C}$	$1.5 \times 10^6$	perspective, visual	Asymmetric "nosecone" shape developed.
40312	0.5" poly $\text{NH}_4\text{Cl}$ sphere dissolve in 90% saturated water at $23.5^\circ\text{C}$	$1.1 \times 10^5$	perspective, still photo	Asymmetric "barrel" with rough bottom (probably broken off)
40331A	0.5" cleaved KBr cube grow in 108% saturated water at $20^\circ\text{C}$	$2.6 \times 10^5$	schlieren, visual	Rapid growth with nucleation on bottom and sides of cell, corners and edges of crystal.
40513A	0.5" cleaved KBr cube at $28+23^\circ\text{C}$ in water saturated at $\sim 2.6^\circ\text{C}$	varying	schlieren, movie	Dissolution and then growth. Rapid convection sensitive to moment or shock. Coherent growth.
40515	5/8" diameter KBr crystal cylinder dissolved in 98% saturated water at $21.9^\circ\text{C}$	$1.4 \times 10^5$	schlieren, movie	Laminar convection very sensitive to shock. $3.0-3.3 \text{ mm/sec}$ plume velocity.
40331B	3/8" thymol crystal grow at $25+20^\circ\text{C}$ in diethyl carbonate saturated at $\sim 30^\circ\text{C}$	low	schlieren, still photo	Initial form poly cluster with profuse nucleation on cell walls; later euhedral growth.

(Continued)

TABLE VI. (Continued)

No.	Experimental Conditions	Grashof Number	Mode of Observation	Remarks
40513B	3/8" thymol crystal grow at 27.5+22°C in diethyl carbonate saturated at 27.5°C	low	schlieren, movie	Poor quality movie appears to show abrupt transition to dendritic growth accompanied by burst of convection.
40514A	5/8" poly thymol sphere dissolve at 23°C in 98% saturated diethyl carbonate	15.7	schlieren, movie	Stream separates from crystal and winds throughout cell. 0.3 mm/sec plume velocity.

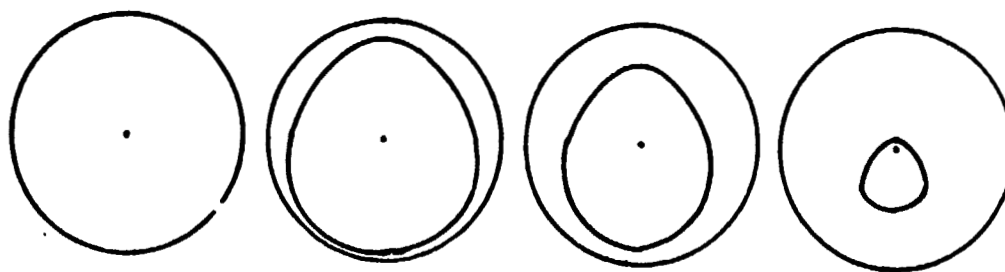


Figure 47. Successive stages of dissolution of  $\text{NH}_4\text{Cl}$  sphere in water. (Experiment 40102)

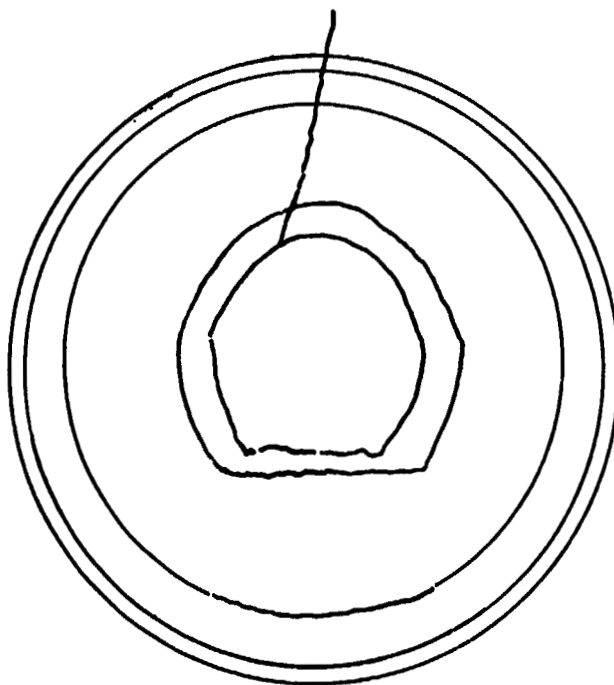


Figure 48. Successive stages of dissolution of  $\text{NH}_4\text{Cl}$  sphere in 90% solution. (Experiment 40312)  
From outside in, 0 min, 10 min, 50 min, 240 min, 270 min.

solution cell, and cooled to room temperature ( $20^{\circ}\text{C}$ ), thereby producing a supersaturation of about 8%. Rapid skeletal growth was observed at the corners of a seed crystal cube. Abundant nuclei were formed on the cell walls and on the cleaved crystal surface. Well-defined laminar schlieren were observed around and above the seed crystal. The rate of upward convection of the plume was estimated at 1 to 2 mm/sec. After 2 hours, the bottom of the cell was filled with tiny acicular crystals and the original crystal surface was overgrown with needles and/or dendrites at its edges and corners. In a later experiment (40513A), a solution was saturated at about  $4^{\circ}$  above room temperature, heated to destroy stray nuclei, and allowed to cool slowly. A cleaved KBr seed was inserted about  $5^{\circ}$  above room temperature and observed to dissolve rather rapidly so that the crystal became asymmetrically wedge shaped (the top being slightly thinner than the bottom, as would be expected). The crystal was removed and reimmersed when the solution was  $2^{\circ}$  cooler. Schlieren observation then showed that there was almost no convection around the crystal except for slight slowly moving oblique schlieren, presumably due to thermal gradients. As the solution cooled further, upward convection rapidly developed which, although apparently uniform, became violently unstable for several seconds whenever the system was disturbed (e.g., by a knock on the supporting table) or the crystal displaced. Another experiment (40515), in which a single-crystal KBr cylinder was immersed in a 98% saturated solution, showed an apparently uniform downward flow with plume velocities of about 5 to 10 mm per second, with similarly violent instabilities whenever the support table

was tapped with a finger (Figure 49). Slight flow irregularities were observed to occur occasionally even under apparently vibration-free conditions (Figure 50). During these experiments some slight residual turbulent convection, apparently due to the recirculation of the main convection current after it encountered the cell walls, was also noted but it was far weaker than the primary current around the crystal.

Thymol/Diethyl Carbonate System: In our first experiment (40331B), a solution of thymol in diethyl carbonate was equilibrated for 3 days at 30°C, poured into a preheated glass cell, and allowed to cool 5°. Insertion of a 1 cm thymol crystal initiated profuse quasi-dendritic (i.e., bladed) growth, both on the seed crystal and throughout the solution. After 30 minutes of growth, during which a polycrystalline cluster had formed around the seed crystal, a stationary vertical convection column was observed extending upward from the cluster. This schlieren pattern did not appear to change during 5 minutes of continuous observation.

After a day of growth, during which all spontaneously initiated crystals had slowly settled to the bottom of the cell, it was noted that the later stages of crystallization (i.e., at lower supersaturation) had produced transparent euhedral crystals. A dissection of the cluster similarly disclosed a core of radial blades and an outer region of transparent euhedral crystals.

A subsequent experiment (40513B) under similar conditions was monitored overnight by time-lapse cinematography. The next morning a



Figure 49. Flow about KBr, perturbed by a tap on the container. Frames from movie taken at one frame per second, starting at upper left. (Experiment 40515)

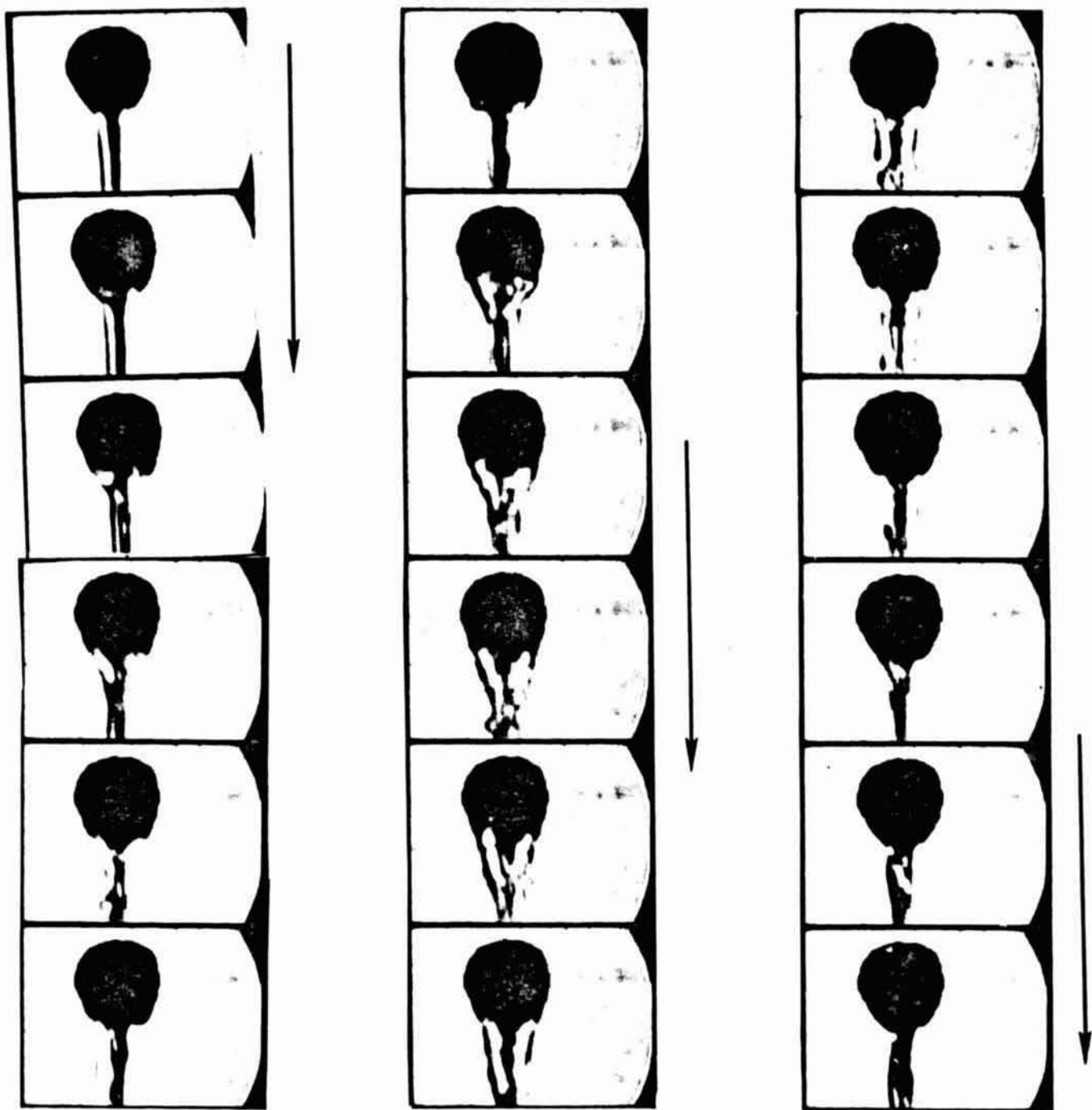


Figure 50. Irregular flow about dissolving KBr crystal in the absence of deliberate perturbations. Frames taken 1 second apart.



large radiating dendritic cluster was found in the cell. Unfortunately, most of the movie was badly overexposed, due to a shutter failure.

These experiments convinced us that our solutions had too high a supersaturation and that our equilibration procedures were inadequate. We then realized the need for continuous stirring during equilibration and modified our procedures, as was described in Section C. Subsequent experiments showed that clear euhedral thymol crystals could be grown at rates of several millimeters per day from solutions cooled  $2^{\circ}$  or  $3^{\circ}$  below their saturation point.

The convection pattern during slow growth or dissolution is quite remarkable and is very different from the theoretical predictions in Section III. For example, immersion of a polycrystalline thymol sphere into a 98% saturated solution (experiment 40514A) caused a downward laminar plume to flow at a rate of about 0.3 mm/sec (Figure 51). This convection stream was unaffected by disturbance of the cell or support table. Even displacement of the crystal merely caused a smooth curvature of the convection stream. What is most remarkable, however, is that this convection stream remained coherent and sharply defined even after it encountered the cell wall which deflected it upward. The ultimate effect, a tangle of twisted schlieren, is reminiscent of the evolution of a pyrotechnic "snake" (Figure 52).

#### G. Conclusions and Future Plans

From the foregoing experiments it appears that the apparatus and techniques developed thus far, although capable of considerable

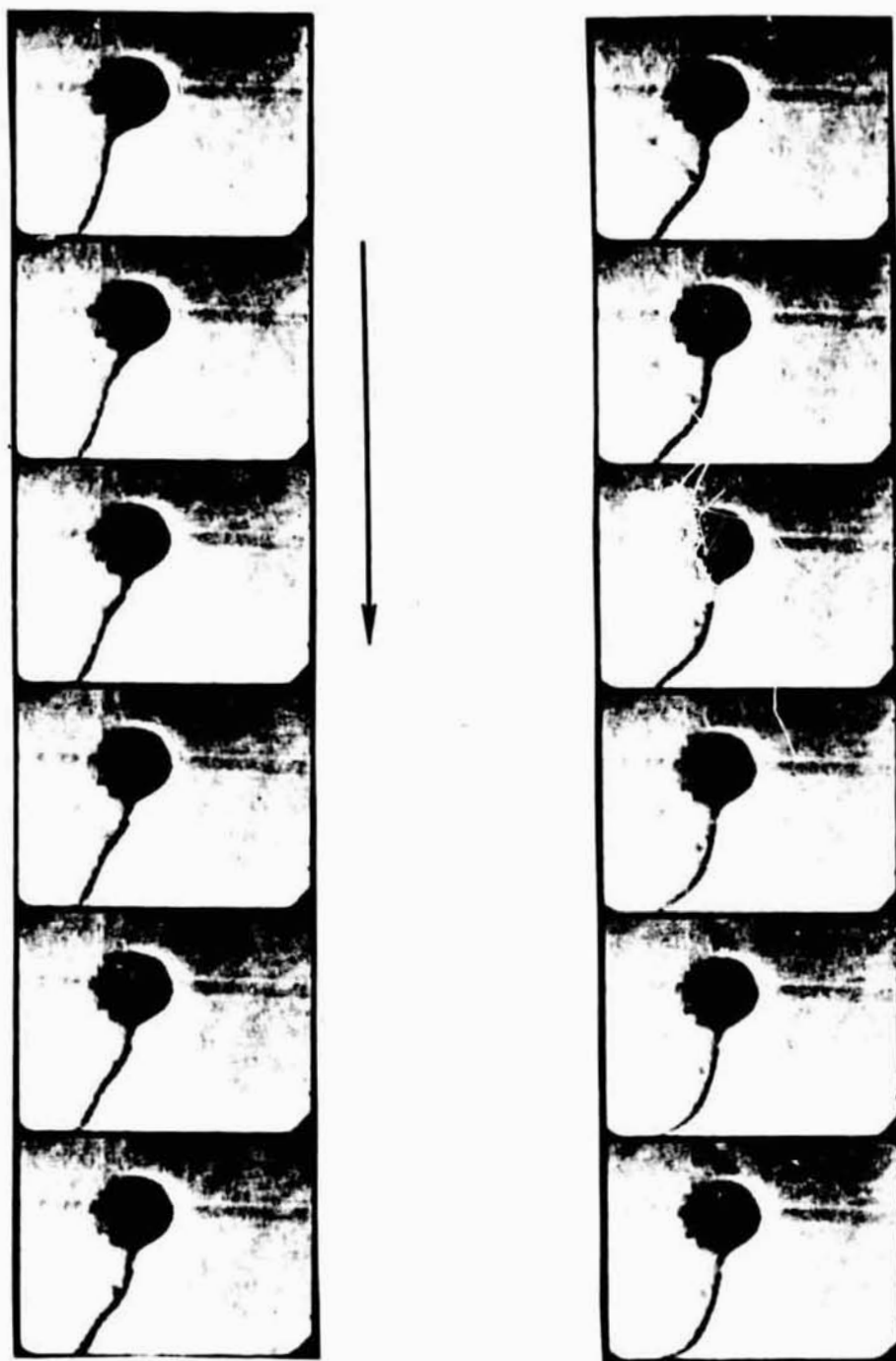


Figure 51. Plume from thymol dissolving in diethyl carbonate shortly after initiation of dissolution (experiment 40514). 5 seconds between frames.

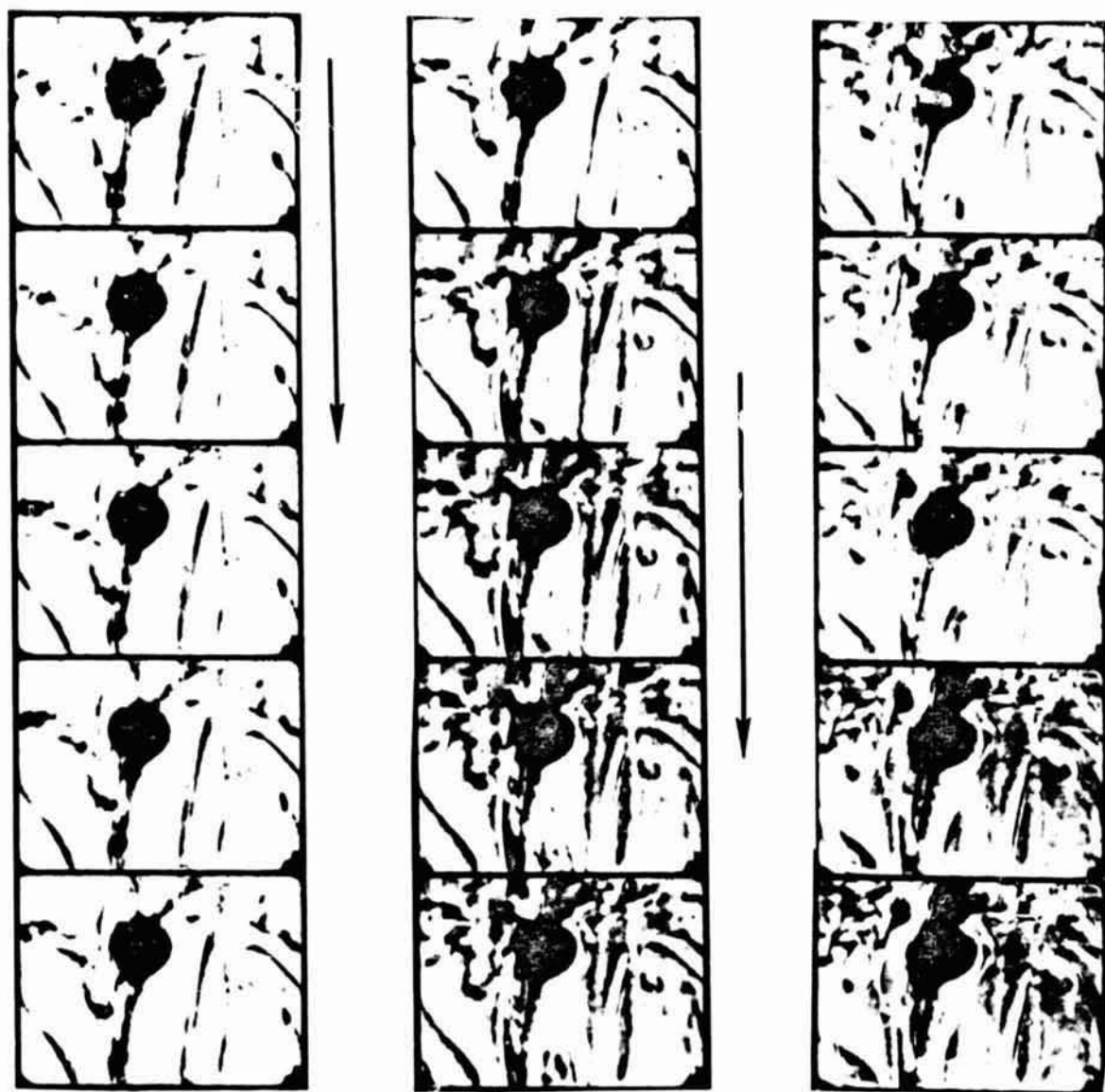


Figure 52. Meandering plume from thymol dissolving as ethyl carbonate several hours after initiation of dissolution. (Experiment 40514.) 5 seconds between frames.

further improvement, are at present adequate for the observation of a great deal of interesting phenomena. Therefore, during the next six months we plan to give primary attention to the performance of experiments and carry out only those apparatus improvements which are readily feasible or particularly needed, such as improved shadow-graph resolution and cell-temperature control.

It also appears that the thymol/diethyl carbonate system has been shown to crystallize at low Grashof numbers and that, at least at reasonably low growth rate, heat effects are not important. This is perhaps sufficiently demonstrated by comparing the dissolution of a KBr cylinder in 98% saturated aqueous solution with the dissolution of a thymol sphere in 98% saturated diethyl carbonate solution. As Table VI shows, the convective velocity varies approximately as the  $1/4$  power of the Grashof number. Therefore, it seems safe to assume that at constant gravity and acceleration, the thymol/diethyl carbonate system is a valid model at  $1 g_e$  for the crystallization of ordinary solution systems in fields of  $\sim 10^{-1} g_e$ .

There is a discrepancy between the vortex-like cell and the convection pattern predicted in Section III and the experimentally observed plume "snake". The resolution of this discrepancy will be one of the primary goals during subsequent months. At present, we tend to regard the reluctance of the convective striae to mix with the bulk solution and the re-emergence of these striae, reflected by the cell walls, into the region of crystallization, as significant warnings of problems that will be encountered during crystallization in space. For this reason, we believe that the present program should eventually

give considerable attention to the theoretical analysis and experimental simulation of low-gravity crystallization with forced convection.

The above experiments also demonstrate that our "low-gravity-simulation" systems, which might more properly be called "acceleration-insensitive" systems, cannot easily be used for predicting the effect of accelerational transients on crystallization in a spacecraft environment. However, the convective chaos effected by accelerational transients on ordinary systems, such as KBr/water, has been shown to be so spectacular that it certainly merits further study.

Finally, successful as the thymol/diethyl carbonate system appears to be, it seems necessary to keep searching for new systems--not only because of the potential toxicity of the present system, but also to demonstrate that the effects observed are not peculiar to one system, but are characteristic of any system crystallizing at a low Grashof number.

## V. FUTURE PLANS

The low gravity simulation experiments will be continued as outlined in Section IV. The effort up until now has concentrated primarily on experimental methods and techniques. In the future emphasis will shift more to actual growth and dissolution experiments. Flow phenomena and its influence on crystal growth will be studied.

If additional funding is forthcoming, a variety of theoretical calculations can be performed. Some possibilities related to surface driven flow are:

1. Extension of previous work on floating zone melting to other values of the parameters, i.e., higher Pr and Sc, higher surface tension driving forces, different equilibrium distribution coefficients, etc.
2. Transient analysis of floating zone melting of high Prandtl number material with radiant heating, for which oscillatory convection is expected.
3. Determination of shape of floating zone due to a surface tension gradient in zero g.
4. Surface driven flow and melt shape in the gradient freeze method with a free melt surface, as observed in several Skylab experiments, but not yet explained or understood.

At best, only two of these tasks could be expected to be completed in one year by an experienced Ph.D. research assistant.

Possible future calculations for free convection about a suspended object might investigate:

1. The influence of the size of the crystal growth container.
2. Influence of Gr and Sc.
3. Influence of finite solubility (changing diameter of sphere).
4. Other geometries, such as cylinder or cube.
5. Perturbations of a steady state by g fluctuations.

A graduate student research assistant could be expected to complete two of these in a one-year period.

## REFERENCES

1. J. C. Brice, The Growth of Crystals from Liquids, 2nd ed., North-Holland Publishing Co. (1973).
2. H. Kadera, "Diffusion Coefficients of Impurities in Silicon Melt," J. Appl. Phys. (Japan), 2 212 (1963).
3. C. E. Chang, "Transport Processes in Unidirectional Crystal Growth," Ph.D. Thesis, University of Southern California, Los Angeles (1973).
4. C. E. Chang and William R. Wilcox, "Localized Interface Breakdown in Zone Melting and the Travelling Heater Method," J. Crystal Growth 21, 182 (1974).
5. D. K. Donald, "Thermal Behavior in Vacuum Zone Refining," Rev. Sci. Instr. 32, 811 (1961).
6. H. J. Merk and J. A. Prins, "Thermal Convection in Laminar Boundary Layers," Appl. Sci. Res. A4, 11, 195, 207, 435 (1953-54).
7. R. Siegel, Trans. Am. Soc. Mech. Eng. 80, 347 (1958).
8. F. J. Suriano, K. T. Yang and J. A. Donlon, Int. J. Ht. Mass Transfer 8, 815 (1965).
9. M. A. Hassain and B. Gebhart in "Heat Transfer 1970," Vol. IV (Elsevier, Amsterdam, 1970).
10. P. J. Shlichta, Informal proposal submitted to NASA, July 1973.
11. W. R. Wilcox, "Simultaneous Heat and Mass Transfer in Free Convection," Che. Eng. Sci. 13, 113 (1961).
12. F. A. Schraub, et al., Trans. ASME 87D, 429 (1965).



## REFERENCES - APPENDIX A

- A-1. W. M. Kays, Convective Heat and Mass Transfer, McGraw-Hill Book Co. (1966) pp. 29.
- A-2. W. M. Rohsenow and H. Y. Choi, Heat, Mass and Momentum Transfer, Prentice-Hall, Inc. (1961).
- A-3. R. B. Bird, W. E. Stewart and E. N. Lightfoot, Transport Phenomena, John Wiley & Sons, Inc. (1960).
- A-4. W. R. Wilcox, "Crystallization Flow," J. Crystal Growth 12, 93 (1972).
- A-5. J. O. Wilkes and S. W. Churchill, "The Finite-Difference Computation of Natural Convection in a Rectangular Enclosure," AIChE J. 12, 161 (1966).
- A-6. L. C. Tien, "Freezing of a Convective Liquid in a Crystal-Growth Tube," Ph.D. Thesis, University of Michigan, Ann Arbor, Michigan (1969).
- A-7. K. E. Torrance, L. Orloff and J. A. Rockett, "Numerical Study of Natural Convection in an Enclosure with Localized Heating from Below---Creeping Flow to the Onset of Laminar Instability," J. Fluid Mech. 36, 33 (1969).
- A-8. B. W. Arden and K. N. Astill, Numerical Algorithms: Origin and Applications, Addison-Wesley Publishing Co. (1970) pp. 148.
- A-9. F. Pan and A. Acrivos, "Steady Flows in Rectangular Cavities," J. Fluid Mech. 28, 643 (1967).

## APPENDIX A

ANALYSIS OF SURFACE DRIVEN FLOW IN  
FLOATING ZONE MELTING

(Chong E. Chang)

The definitions of symbols and the assumptions were given in Section II. The coordinate system and geometry for floating zone melting were shown in Figure 1. Following are the fluid flow, heat transfer, and mass transfer equations used in the analyses (A-1, A-2, A-3).

A. Dimensional Equations(1) Continuity Equation

At constant melt density, conservation of mass requires that

$$\frac{\partial v_r}{\partial r} + \frac{v_r}{r} + \frac{\partial v_z}{\partial z} = 0 \quad (\text{A-1})$$

where  $v_r$  is the radial velocity and  $v_z$  is the axial velocity at  $r$  and  $z$ .

(2) Momentum Equations

Force balances yield the Navier-Stokes equations for a Newtonian fluid:

$$\rho \left( v_r \frac{\partial v_r}{\partial r} + v_z \frac{\partial v_r}{\partial z} \right) = - \frac{\partial p}{\partial r} + \mu \left( \frac{\partial^2 v_r}{\partial r^2} + \frac{1}{r} \frac{\partial v_r}{\partial r} - \frac{v_r}{r^2} + \frac{\partial^2 v_r}{\partial z^2} \right) \quad (\text{A-2})$$

$$\rho \left( v_r \frac{\partial v_z}{\partial r} + v_z \frac{\partial v_z}{\partial z} \right) = - \frac{\partial p}{\partial z} + \mu \left( \frac{\partial^2 v_z}{\partial r^2} + \frac{1}{r} \frac{\partial v_z}{\partial r} + \frac{\partial^2 v_z}{\partial z^2} \right) - g \quad (\text{A-3})$$

where the total pressure  $P$  may be decomposed into a hydrostatic portion  $p_0$  and a dynamic portion  $p$ , representing the change in local pressure due to the convection. Thus we define

$$P \equiv p_0 + p \quad (\text{A-4})$$

where

$$p_0 \equiv \rho_f g (\ell - z), \quad (\text{A-5})$$

$$\rho_f = \rho [1 + \beta (T - T_m)] , \quad (\text{A-6})$$

and

$$\beta \equiv \frac{1}{\rho} \left( \frac{\partial \rho}{\partial T} \right)_{p,m} \quad (\text{A-7})$$

The boundary conditions for the flow field are:

$$\left. \begin{aligned} \text{a) At } z = \ell \quad v_r &= 0, \quad v_z = -v_c \left( \frac{\rho_c}{\rho_f} \right) \\ \text{b) At } z = -\ell \quad v_r &= 0, \quad v_z = -v_c \left( \frac{\rho_c}{\rho_f} \right) \text{ or} \\ \text{c) At } z = 0 \quad v_z &= \frac{\partial v_r}{\partial z} = 0 \quad (\text{only for } v_c = 0) \\ \text{d) At } r = 0 \quad v_r &= \frac{\partial v_z}{\partial r} = 0 \\ \text{e) At } r = a \quad v_r &= 0 \text{ and} \\ \text{f) } \frac{\partial v_z}{\partial r} &= \frac{1}{\mu} \frac{\partial \gamma}{\partial z} = \frac{\sigma}{\mu} \frac{\partial T}{\partial z} \end{aligned} \right\} \quad (\text{A-8})$$

where  $\rho$  is the density of the liquid,  $\rho_c$  is the density of the solid,  $\rho_f$  is the density of the liquid at the melting point,  $\mu$  is the

viscosity,  $g$  is the acceleration field opposite to the  $z$ -axis,  $l$  is one half of the zone length,  $a$  is the radius of the zone,  $T$  is the temperature,  $T_m$  is the melting point,  $\beta$  is the thermal densification coefficient,  $v_c$  is the zone travel rate,  $\gamma$  is the surface tension, and  $\sigma \equiv \partial\gamma/\partial T$  is the temperature dependence of the surface tension.

Boundary conditions (a) and (b) arise from the zone motion, (c) and (d) from symmetry, (e) from confinement of flow to the zone. Boundary condition (e) results from equating the surface tension gradient force to the viscous force at the melt surface.

### (3) Heat Transfer Equations

A heat balance over a differential element yields for constant properties:

$$\rho C_p \left( v_z \frac{\partial T}{\partial z} + v_r \frac{\partial T}{\partial r} \right) = k \left( \frac{\partial^2 T}{\partial z^2} + \frac{1}{r} \frac{\partial T}{\partial r} + \frac{\partial^2 T}{\partial r^2} \right) \quad (A-9)$$

The boundary conditions for heat transfer are:

$$\left. \begin{aligned} \text{a) At } r = 0, \quad \frac{\partial T}{\partial r} &= 0 \\ \text{b) At } r = a, \quad -k \frac{\partial T}{\partial r} &= \sigma \epsilon_s (T^4 - T_c^4) \\ \text{c) At } \left\{ \begin{array}{l} r = a \\ \text{and} \\ z = 0 \end{array} \right\}, \quad T &= T_o \\ \text{d) At } z = l, \quad T &= T_m \\ \text{e) At } z = -l, \quad T &= T_m \text{ or} \\ \text{f) At } z = 0, \quad \frac{\partial T}{\partial z} &= 0 \text{ (only for } v_c = 0) \end{aligned} \right\} \quad (A-10)$$

where  $T_c$  is the temperature of the surroundings,  $T_m$  is the melting point,  $T_o$  is the temperature of line heat source at the periphery of the center of the zone,  $c_p$  is the heat capacity of the melt,  $k$  is its thermal conductivity,  $\sigma$  is the Stefan-Boltzmann constant, and  $\epsilon_s$  is the emissivity of the melt. Boundary conditions (a) and (f) arise from symmetry, (b) by equating condition to the melt surface to radiation into the surroundings, and (c), (d) and (e) by definition.

When the solid phase was included in the heat transfer analysis, the following alternative boundary conditions were used instead of the boundary condition 10 d). Radiation, insulation, and infinitely rapid heat transfer to the surroundings at the top of the solid were all considered. The boundary conditions for these possibilities are:

$$\left. \begin{aligned} \text{d')} \quad \text{At } z = b, \quad -k \frac{\partial T}{\partial z} &= \sigma \epsilon_s (T^4 - T_c^4) \text{ for radiation} \\ \frac{\partial T}{\partial z} &= 0 \text{ for insulation} \\ T &= T_c \text{ for infinite heat transfer coefficient} \end{aligned} \right\} \quad (\text{A-10})$$

where  $b$  is the distance from the center of the zone to the end of the solid rod.

#### (4) Mass Transfer

An impurity balance over a differential element yields:

$$v_z \frac{\partial m}{\partial z} + v_r \frac{\partial m}{\partial r} = D \left( \frac{\partial^2 m}{\partial z^2} + \frac{1}{r} \frac{\partial m}{\partial r} + \frac{\partial^2 m}{\partial r^2} \right) \quad (\text{A-11})$$

Boundary conditions for mass transfer in the mass-centered reference system are depicted in Figure A-1, and are as follows (A-4)

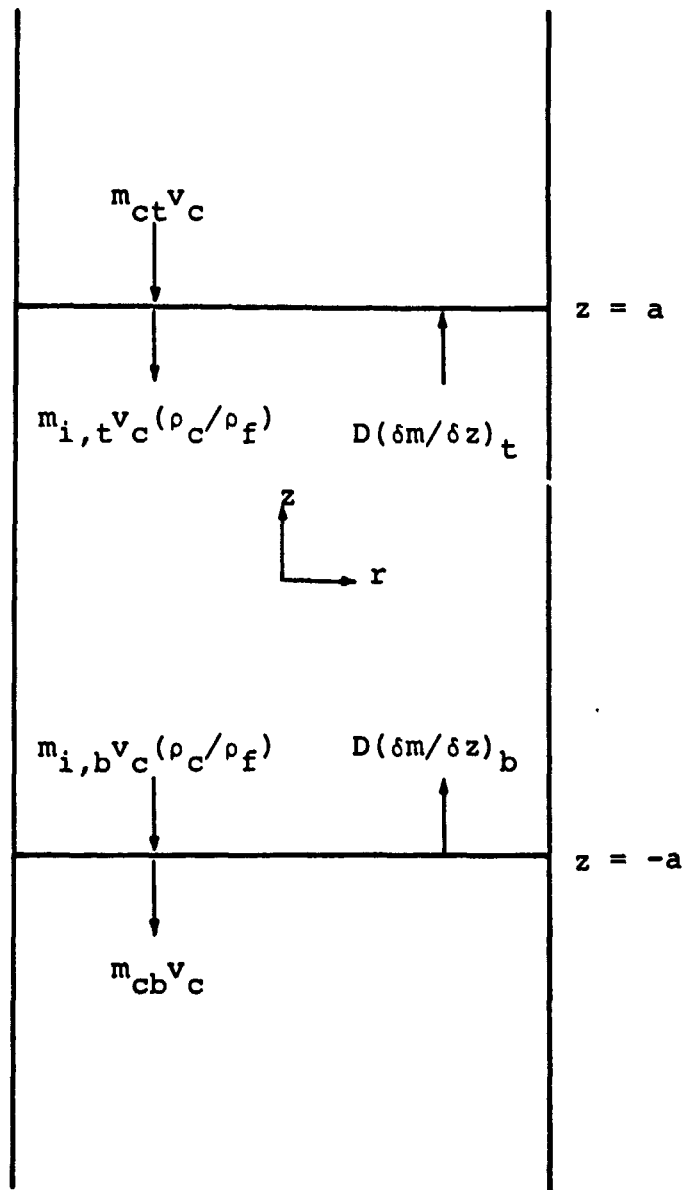


Figure A-1. The geometry of the liquid zone and the mass transfer fluxes at the liquid/solid interfaces for zone travel rate  $v_c$ .

$$\begin{aligned}
 \text{a) At } r = 0, \quad \frac{\partial m}{\partial r} &= 0 \\
 \text{b) At } r = a, \quad \frac{\partial m}{\partial r} &= 0 \\
 \text{c) At } z = -\ell, \quad m_{cb} v_c &= m_{i,b} v_c \left( \frac{\rho_c}{\rho_f} \right) + D \left( \frac{\partial m}{\partial z} \right)_b \\
 \text{d) at } z = \ell, \quad m_{ct} v_c &= m_{i,t} v_c \left( \frac{\rho_c}{\rho_f} \right) + D \left( \frac{\partial m}{\partial z} \right)_t
 \end{aligned}
 \tag{A-12}$$

where  $m$  is the mass concentration of impurity,  $D$  is the binary molecular diffusion coefficient,  $m_{cb}$  is the impurity concentration in the crystal,  $m_{ct}$  is the impurity concentration in the feed ingot (assumed constant),  $m_{i,b}$  is the impurity concentration in the melt at the growing interface,  $m_{i,t}$  is the impurity concentration in the melt at the melting interface, and  $v_c (\rho_c / \rho_f)$  is the mass velocity in the melt due to the movement of the zone at rate  $v_c$ . Boundary condition (a) comes from symmetry, (b) comes from the prohibition on transfer through the melt surface, and (c) and (d) represent material balances at the interfaces.

#### B. Dimensionless Equations

For convenience in solving the problem, equations were restated in the following dimensionless forms:

##### (1) Dimensionless Continuity Equation

$$\frac{\partial v}{\partial R} + \frac{v}{R} + \frac{\partial v}{\partial Z} = 0
 \tag{A-13}$$

where

$$R = \frac{r}{a}, \quad Z = \frac{z}{a}, \quad v_r = \frac{v_r a}{v}, \quad v_z = \frac{v_z a}{v},$$

and  $v = \mu / \rho$  is the kinematic viscosity.

(2) Dimensionless Momentum Equation

$$v_r \frac{\partial v_r}{\partial R} + v_z \frac{\partial v_r}{\partial Z} = - \left( \frac{a^4}{v^2} \right) \left( \frac{1}{\rho} \frac{dP}{dR} \right) + \left( \frac{\partial^2 v_r}{\partial R^2} + \frac{1}{R} \frac{\partial v_r}{\partial R} - \frac{v_r}{R^2} + \frac{\partial^2 v_r}{\partial Z^2} \right) \quad (A-14)$$

$$v_r \frac{\partial v_z}{\partial R} + v_z \frac{\partial v_z}{\partial Z} = - \frac{a^4}{v^2} \left( \frac{1}{\rho} \frac{\partial P}{\partial Z} + g \right) + \left( \frac{\partial^2 v_z}{\partial R^2} + \frac{1}{R} \frac{\partial v_z}{\partial R} + \frac{\partial^2 v_z}{\partial Z^2} \right) \quad (A-15)$$

The dimensionless boundary conditions for flow are:

$$\left. \begin{aligned} \text{a) At } Z = l/a, \quad v_r &= 0, \quad v_z = -v_{cf} \\ \text{b) At } Z = -l/a, \quad v_r &= 0, \quad v_z = -v_{cf} \text{ or} \\ \text{c) At } Z = 0, \quad v_z &= \frac{\partial v_r}{\partial Z} = 0 \text{ (only for } v_{cf} = 0) \\ \text{d) At } R = 0, \quad v_r &= \frac{\partial v_z}{\partial R} = 0 \\ \text{e) At } R = 1, \quad v_r &= 0, \quad \frac{\partial v_z}{\partial R} = M' \frac{\partial \theta}{\partial Z} \end{aligned} \right\} \quad (A-16)$$

where

$$v_{cf} = \left( \frac{v_c a}{v} \right) \left( \frac{\rho_c}{\rho_f} \right) \quad (A-17)$$

is the dimensionless mass velocity in the melt due to movement of the zone,

$$M' = \frac{\rho \sigma (T_o - T_m) a}{\mu^2} \quad (A-18)$$



is the dimensionless surface tension driving force parameter, and

$$\theta = \frac{T - T_m}{T_o - T_m} \quad (\text{A-19})$$

The pressure terms in the momentum equations are eliminated by differentiating Equation (A-14) with respect to Z and Equation (A-15) with respect to R, and subtracting to obtain

$$\left(v_r - \frac{1}{R}\right)\left(\frac{\partial \omega}{\partial R} - \frac{\omega}{R}\right) + v_z \frac{\partial \omega}{\partial Z} - \left(\frac{\partial^2 \omega}{\partial R^2} + \frac{\partial^2 \omega}{\partial Z^2}\right) + Gr_h \frac{\partial \theta}{\partial R} + Gr_m \frac{\partial C}{\partial R} = 0 \quad (\text{A-20})$$

where

$$\omega = \frac{\partial v_r}{\partial Z} - \frac{\partial v_z}{\partial R} \quad (\text{A-21})$$

is the dimensionless vorticity,

$$Gr_h = \frac{g\beta(T_o - T_m)a^3}{\nu^2} \quad (\text{A-22})$$

is the Grashof number for temperature variations,

$$Gr_m = \frac{g\alpha(m_t)a^3}{\nu^2} \quad (\text{A-23})$$

is the Grashof number for composition variations, and

$$C = \frac{m}{m_t} \quad (\text{A-24})$$

is a dimensionless composition,  $\alpha = (\partial \rho / \partial m) / \rho$  is the concentration densification coefficient, and  $m_t$  is the impurity concentration the feed solid would have if it had the same density as the melt.

The derivation of the terms,  $Gr_h \frac{\partial \theta}{\partial R}$  and  $Gr_m \frac{\partial C}{\partial R}$  in the momentum equation (A-20) is as follows:

The term  $-(a^4/\nu^2 \rho) (\partial P/\partial R)$  in Equation (A-14) is differentiated with respect to Z, and  $-(a^4/\nu^2) (g + \frac{1}{\rho} \frac{\partial P}{\partial R})$  in Equation (A-15) is differentiated with respect to R. Then, subtracting them by using Equations (A-4) through (A-7) we obtain:

$$\begin{aligned}
 & \frac{a^3}{\nu^2} \left[ -\frac{\partial}{\partial Z} \left( \frac{1}{\rho} \frac{\partial P}{\partial R} \right) + \frac{\partial}{\partial R} \left( \frac{1}{\rho} \frac{\partial P}{\partial Z} + g \right) \right] \\
 &= \frac{a^3}{\nu^2} \left[ -\frac{\partial}{\partial Z} \left\{ \frac{1}{\rho} \left( \frac{\partial P_o}{\partial R} + \frac{\partial P}{\partial R} \right) \right\} + \frac{\partial}{\partial R} \left\{ \frac{1}{\rho} \left( \frac{\partial P_o}{\partial Z} + \frac{\partial P}{\partial Z} \right) + g \right\} \right] \\
 &= \frac{a^3}{\nu^2} \left[ -\frac{\partial}{\partial Z} \left( \frac{1}{\rho} \frac{\partial P}{\partial R} \right) + \frac{\partial}{\partial R} \left\{ \frac{1}{\rho} \left( -\rho_f g + \frac{\partial P}{\partial Z} \right) + g \right\} \right] \\
 &= \frac{a^3}{\nu^2} \left[ -\frac{1}{\rho} \frac{\partial^2 P}{\partial Z \partial R} - \frac{\partial P}{\partial R} \frac{\partial}{\partial Z} \left( \frac{1}{\rho} \right) + \frac{\partial}{\partial R} \left\{ -\left( 1 + \beta(T - T_m) \right) g + \frac{1}{\rho} \frac{\partial P}{\partial Z} + g \right\} \right] \\
 &= \frac{a^3}{\nu^2} \left[ -\frac{1}{\rho} \frac{\partial^2 P}{\partial Z \partial R} - \frac{\partial P}{\partial R} \frac{\partial}{\partial Z} \left( \frac{1}{\rho} \right) - g\beta \frac{\partial(T - T_m)}{\partial R} + \frac{1}{\rho} \frac{\partial^2 P}{\partial R \partial Z} + \frac{\partial P}{\partial Z} \frac{\partial}{\partial R} \left( \frac{1}{\rho} \right) \right] \\
 &= -\frac{g\beta(T_o - T_m)a^3}{\nu^2} \frac{\partial \theta}{\partial R} \\
 &= -Gr_h \frac{\partial \theta}{\partial R}
 \end{aligned}$$

The term  $Gr_m \frac{\partial C}{\partial R}$  is generated by the same procedure by taking the density change due to concentration gradient into account.

The dimensionless momentum equation may alternatively be defined by a stream function  $\psi$  such that continuity is automatically satisfied from the following relationships:

$$v_r = \frac{1}{R} \frac{\partial \psi}{\partial Z} \quad (A-25)$$

$$v_z = -\frac{1}{R} \frac{\partial \psi}{\partial R} \quad (A-26)$$

$$\omega = \frac{1}{R} \left( \frac{\partial^2 \psi}{\partial R^2} - \frac{1}{R} \frac{\partial \psi}{\partial R} + \frac{\partial^2 \psi}{\partial R^2} \right) \quad (A-27)$$

From Eqs. (A-25) through (A-27), the momentum equation (A-20) is expressed by a single dependent variable  $\psi$  as follows:

$$\begin{aligned} & \frac{1}{R} \frac{\partial \psi}{\partial Z} \left( \frac{\partial^3 \psi}{\partial Z^2 \partial R} - \frac{1}{R} \frac{\partial^2 \psi}{\partial Z^2} + \frac{\partial^3 \psi}{\partial R^3} - \frac{2}{R} \frac{\partial^2 \psi}{\partial R^2} + \frac{2}{R^2} \frac{\partial \psi}{\partial R} \right) \\ & - \frac{1}{R} \frac{\partial \psi}{\partial R} \frac{\partial}{\partial Z} \left( \frac{\partial^2 \psi}{\partial Z^2} + \frac{\partial^2 \psi}{\partial R^2} - \frac{1}{R} \frac{\partial \psi}{\partial R} \right) - \frac{1}{R^2} \frac{\partial \psi}{\partial Z} \frac{\partial^2 \psi}{\partial Z^2} \\ & + \frac{1}{R^2} \frac{\partial \psi}{\partial Z} \left( -\frac{\partial^2 \psi}{\partial R^2} + \frac{1}{R} \frac{\partial \psi}{\partial R} \right) \\ & - \left( 2 \frac{\partial^4 \psi}{\partial Z^2 \partial R^2} - \frac{2}{R} \frac{\partial^3 \psi}{\partial Z^2 \partial R} + \frac{\partial^4 \psi}{\partial Z^4} + \frac{\partial^4 \psi}{\partial R^4} - \frac{2}{R} \frac{\partial^3 \psi}{\partial R^3} \right. \\ & \left. + \frac{3}{R^2} \frac{\partial^2 \psi}{\partial R^2} - \frac{3}{R^3} \frac{\partial \psi}{\partial R} \right) + Gr_h (\partial \theta / \partial Z) + Gr_m (\partial C / \partial Z) = 0 \quad (A-28) \end{aligned}$$

The boundary conditions are also transformed in terms of the stream function. Since the stream function along the axis is a constant, it may be taken as zero for simplification. On the basis

of this, the boundary conditions are

$$\begin{aligned}
 \text{a) At } Z = l/a, \quad \psi &= \frac{R^2 v_{cf}}{2}, \quad \frac{\partial \psi}{\partial Z} = 0 \\
 \text{b) At } Z = -l/a, \quad \psi &= \frac{R^2 v_{cf}}{2}, \quad \frac{\partial \psi}{\partial Z} = 0 \quad \text{or} \\
 \text{c) At } Z = 0, \quad \psi &= \frac{\partial \psi}{\partial Z} = 0 \quad (\text{for } v_{cf} = 0) \\
 \text{d) At } R = 0, \quad \psi &= \frac{\partial \psi}{\partial R} = 0 \\
 \text{e) At } R = 1, \quad \psi &= \frac{v_{cf}}{2}, \quad \frac{\partial \psi}{\partial R} - \frac{\partial^2 \psi}{\partial R^2} = M' \frac{\partial \theta}{\partial Z}
 \end{aligned}
 \tag{A-29}$$

### (3) Dimensionless Heat Transfer Equations

By introducing the previously defined dimensionless length and velocity parameters for  $r$ ,  $z$ ,  $v_z$  and  $v_r$  into Equation (A-9) we obtain

$$v_z \frac{\partial \theta}{\partial Z} + v_r \frac{\partial \theta}{\partial R} = \frac{1}{Pr} \left[ \frac{\partial^2 \theta}{\partial Z^2} + \frac{1}{R} \frac{\partial \theta}{\partial R} + \frac{\partial^2 \theta}{\partial R^2} \right]
 \tag{A-31}$$

where  $Pr = C_p \mu / k$  is the Prandtl number and

$$\theta = \frac{T - T_m}{T_o - T_m}
 \tag{A-19}$$

or

$$\theta = \frac{T - T_m}{T_m - T_c}
 \tag{A-31}$$

The dimensionless boundary conditions for energy transfer are:

$$\begin{aligned}
 & \text{a) At } R = 0, \quad \frac{\partial \theta}{\partial R} = 0 \\
 & \text{b) At } R = 1, \quad \frac{\partial \theta}{\partial R} = - \frac{a\sigma\epsilon_s}{k\Delta T} \left[ \{\theta\Delta T + T_m\}^4 - \{\theta_c\Delta T + T_m\}^4 \right] \\
 & \text{c) At } \begin{cases} R = 1, \\ Z = 0, \end{cases} \quad \theta = \frac{T_o - T_m}{\Delta T} \text{ (line heat source at } T_o) \\
 & \text{d) At } Z = l/a, \quad \theta = 0 \\
 & \text{e) At } Z = -l/a, \quad \theta = 0, \text{ or} \\
 & \text{f) At } Z = 0, \quad \frac{\partial \theta}{\partial Z} = 0 \text{ (only for } V_{cf} = 0) \\
 & \text{d') At } Z = b/a, \quad \frac{\partial \theta}{\partial Z} = - \frac{a\sigma\epsilon_s}{k\Delta T} \left[ \{\theta\Delta T + T_m\}^4 - \{\theta_c\Delta T + T_m\}^4 \right] \\
 & \qquad \qquad \qquad \text{for radiation} \\
 & \qquad \qquad \qquad \frac{\partial \theta}{\partial Z} = 0 \quad \text{for insulation} \\
 & \qquad \qquad \qquad \theta = \theta_c \quad \text{for infinite heat transfer coefficient}
 \end{aligned} \tag{A-32}$$

where  $\Delta T$  is either  $(T_o - T_m)$  if  $\theta$  is defined by Equation (A-19), or  $(T_m - T_c)$  if  $\theta$  is defined by Equation (A-31), and  $\theta_c = (T_c - T_m)/\Delta T$  is the dimensionless temperature of the surroundings.

#### (4) Dimensionless Mass Transfer Equations

The following dimensionless impurity concentration parameter  $C$  was employed with the previously defined length and

velocity parameters for  $r$ ,  $z$ ,  $v_r$ , and  $v_z$  to transform Equation (A-11) to

$$v_z \frac{\partial C}{\partial Z} + v_r \frac{\partial C}{\partial R} = \frac{1}{Sc} \left[ \frac{\partial^2 C}{\partial R^2} + \frac{1}{R} \frac{\partial C}{\partial R} + \frac{\partial^2 C}{\partial Z^2} \right] \quad (A-33)$$

where  $Sc = \nu/D$  is the Schmidt number.

The dimensionless boundary conditions for mass transfer are

$$\left. \begin{aligned} \text{a) At } R = 0, \quad \frac{\partial C}{\partial R} &= 0 \\ \text{b) At } R = 1, \quad \frac{\partial C}{\partial R} &= 0 \\ \text{c) At } Z = -\ell/a, \quad C_{i,b} &= \frac{C_{i+1,b}}{\left\{ 1 + ScV_c \left( k_o - \frac{\rho_c}{\rho_f} \right) \Delta Z \right\}} \\ \text{d) At } Z = \ell/a, \quad C_{i,t} &= \frac{C_{ct} ScV_c \Delta Z + C_{i-1,t}}{\left\{ ScV_c \Delta Z \left( \frac{\rho_c}{\rho_f} \right) + 1 \right\}} \end{aligned} \right\} \quad (A-34)$$

where  $C_{ct} (= m_{ct}/m_t)$  is the dimensionless impurity concentration in the feed crystal, subscript  $i$  denotes a  $Z$  grid point and  $V_c (= v_c a/\nu)$  is the dimensionless zone travel rate. The boundary conditions (A-35) (c) and (d) result from taking the finite difference equation form of the

boundary conditions (A-12) (c) and (d), and expressing the impurity concentration in the crystal in terms of the equilibrium distribution coefficient  $k_0$  and the interfacial concentrations.

### C. Computation

One of the typical numerical procedures for calculating the stream function in an enclosed fluid is to solve for the vorticity function, and then find the stream function from vorticity by employing a successive iteration method (A-5, A-6, A-7). Rather than finding the stream function via the vorticity equation, a single step is necessary to compute the stream function when Equation (A-28) is used. It is obvious that this procedure introduces equal or less computation errors than the former method since the errors caused in the process of computing the stream function via vorticity are entirely eliminated by using a single step computation.

An approximate solution is obtained at a finite number of equidistant grid points having coordinates  $Z = (i-1)\Delta Z$  and  $R = (j-1)\Delta R$ , where  $i$  and  $j$  are integers. The parabolic finite difference equation was employed for Equation (A-28). The resultant computation molecule is shown in Figure A-2, in which twelve current values at the nearest neighboring grid points are required for an explicit computation of the new stream function. Computations of the stream function at the grid points next to the liquid/solid boundaries and to the axis are possible due to the symmetry condition of the stream function at those boundaries. The stream functions at the

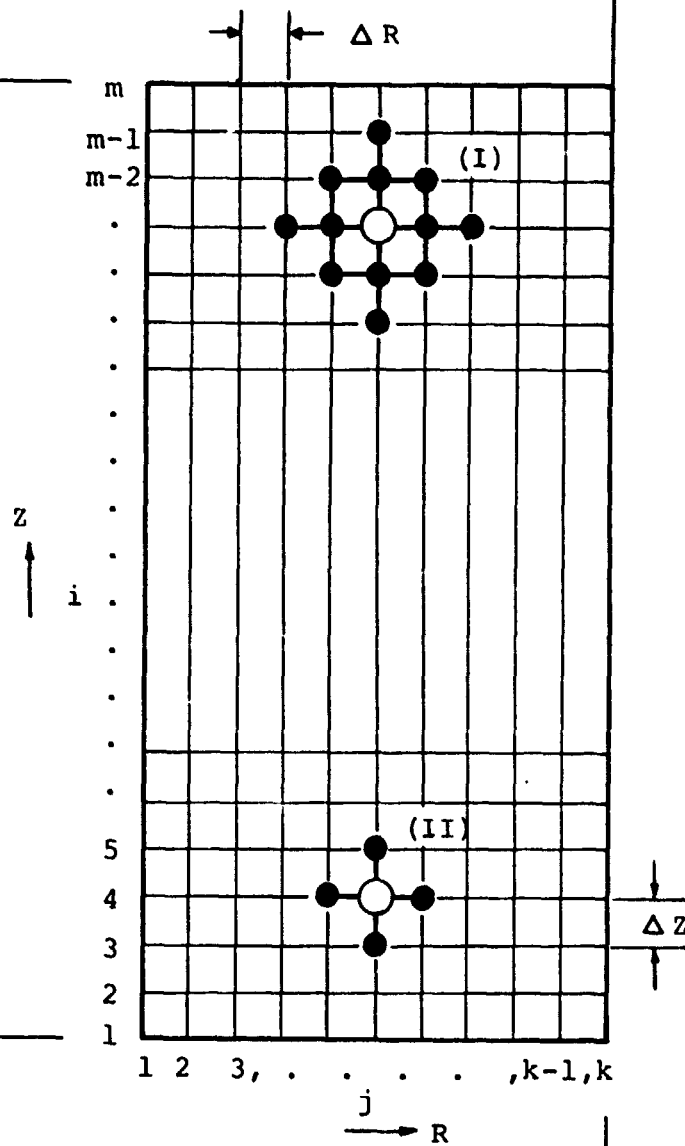


Figure A-2. The finite difference grid system and the computational molecules [(I) for stream function, (II) for temperature and concentration] used in the numerical calculations.



interior grid points next to the free liquid surface are calculated by the interpolation method, since the stream function at the free liquid surface is readily calculable using Equation (A-29) (d). The Gauss-Seidel iteration method (A-12) was employed for computer calculation. For  $M' < 350$  we obtained convergent solutions when  $11 \times 11$  grid points were used. However, an increased number of grid points were necessary for convergence with higher values of  $M'$ , as shown in Table I.

The dimensionless vorticities and velocities in the melt were computed by the finite difference equations derived from Equation (A-25) through (A-27). The calculated flow velocities were utilized for computations of the temperature and impurity concentration fields. The same computational scheme was employed for the analysis of heat and mass transfer. The finite difference of Equation (A-30) for heat transfer, and of Equation (A-33) for mass transfer resulted in the computation molecule as shown in Figure A-2. The Newton-Raphson method (A-9) was used to iteratively solve for the temperatures at the surfaces because of the non-linearity of the thermal radiation boundary conditions, Equations (A-32) (b) and (d'). A rapidly converging solution for heat transfer was attained by using an overrelaxation parameter of 1.9 when the Prandtl number was low (metals). In heat transfer analyses with high Prandtl numbers or in mass transfer analyses for high Schmidt number liquids (including silicon), introduction of the overrelaxation parameter impaired the convergence had to be employed in order to obtain a convergent solution, at the expense of an increased number of iterations.

APPENDIX B  
ANALYSIS OF FREE CONVECTION  
ABOUT A SPHERE

(Chong K. Kim)

A. Dimensionless Equations

The symbols were defined in Section III. Figure B-1 shows the spherical coordinate system used for this problem along with its

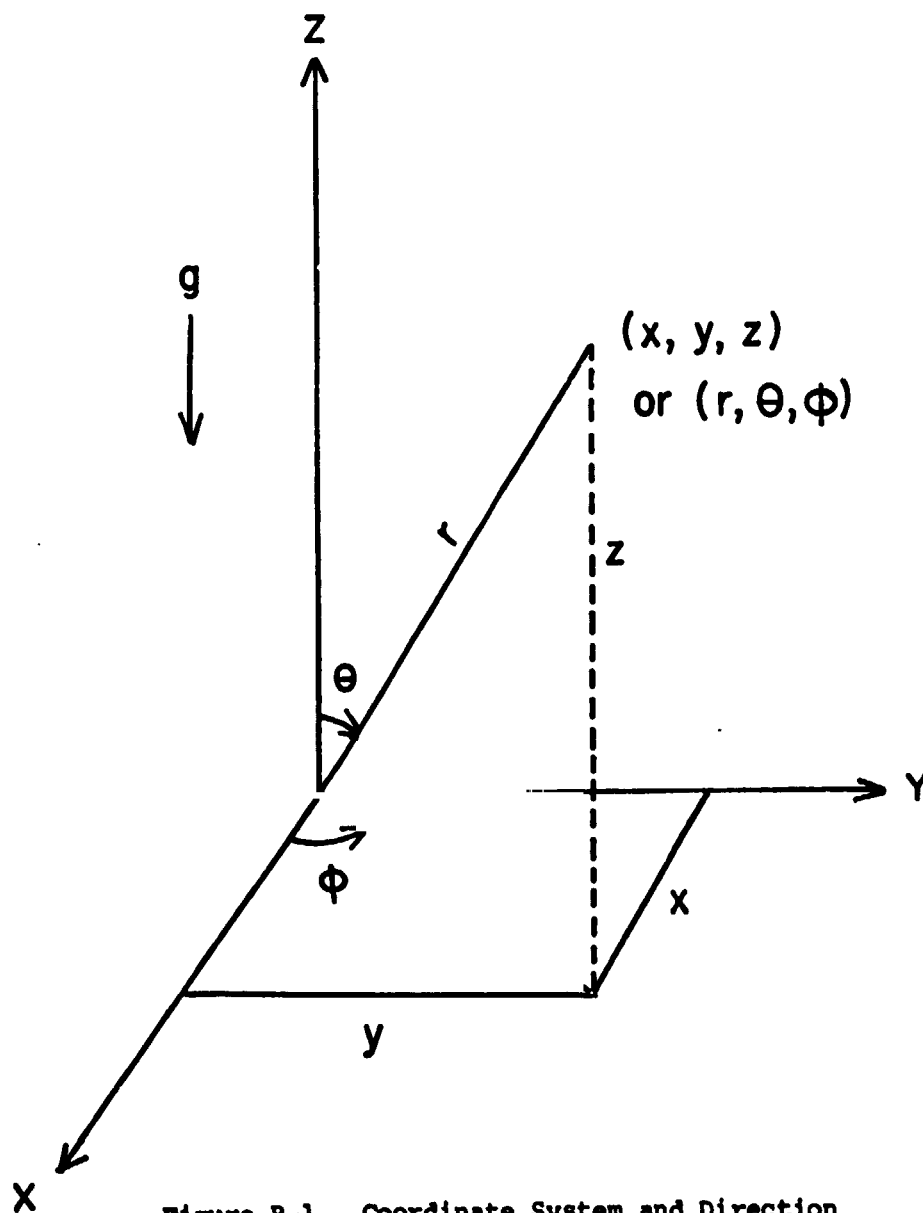


Figure B-1. Coordinate System and Direction of Gravity

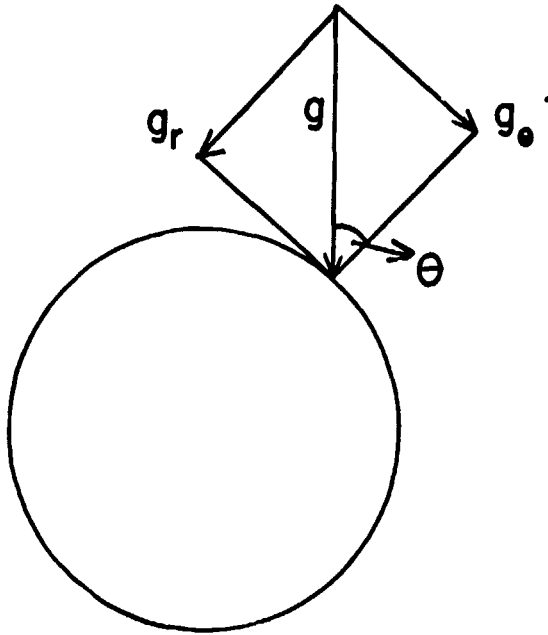


Figure B-2. Vector Analysis  
of Gravity on  
Sphere

orientation relative to the  
accelerational vector.

Figure B-2 shows that the  
acceleration body force  $g$   
may be decomposed into two  
components,  $g_r = -g \cos \theta$   
and  $g_\theta = g \sin \theta$ .

The pressure in the  
momentum equation can be  
written as the sum of the  
pressure  $p'$  due to the fluid  
motion and that due to the  
fluid density far from the  
sphere  $\rho_\infty$ , so that

$$\begin{aligned}\frac{\partial p}{\partial r} &= g_r \rho_\infty + \frac{\partial p'}{\partial r} \\ &= -g \rho_\infty \cos \theta + \frac{\partial p'}{\partial r}\end{aligned}\quad (B-1)$$

and

$$\begin{aligned}\frac{\partial p}{r \partial \theta} &= g_\theta \rho_\infty + \frac{\partial p'}{r \partial \theta} \\ &= g \rho_\infty \sin \theta + \frac{\partial p'}{r \partial \theta}\end{aligned}\quad (B-2)$$

The following dimensionless variables were employed:

$$Gr = \frac{(2a)^3 g \alpha (W_o - W_\infty)}{\nu^2}, \quad Sc = \frac{\nu}{D}, \quad u = \frac{ua}{\nu}, \quad v = \frac{va}{\nu}, \quad P = \frac{p'a^2}{\rho \nu^2} = \frac{p'a^2}{\mu \nu}.$$

Finally, in terms of dimensionless variables the differential equations are:

(a) Continuity;

$$\frac{\partial U}{\partial R} + \frac{2}{R} U + \frac{\cot \theta}{U} V + \frac{1}{R} \frac{\partial V}{\partial \theta} = 0 \quad (B-3)$$

(b) Momentum;

$$\begin{aligned}\frac{\partial U}{\partial \tau} + U \frac{\partial U}{\partial R} + \frac{V \partial U}{R \partial \theta} - \frac{V^2}{R} &= -\frac{Gr}{8} \phi \cos \theta \\ -\frac{\partial p}{\partial R} + \frac{\partial^2 U}{\partial R^2} + \frac{4}{R} \frac{\partial U}{\partial R} + \frac{1}{R^2} \frac{\partial^2 U}{\partial \theta^2} + \frac{\cot \theta}{R^2} \frac{\partial U}{\partial \theta} + \frac{2}{R^2} U &= \quad (B-4) \\ \frac{\partial V}{\partial \tau} + U \frac{\partial V}{\partial R} + \frac{V}{R} \frac{\partial V}{\partial \theta} + \frac{UV}{R} &= \frac{Gr}{8} \phi \sin \theta \\ -\frac{1}{R} \frac{\partial P}{\partial \theta} + \frac{\partial^2 V}{\partial R^2} + \frac{2}{R} \frac{\partial V}{\partial R} + \frac{1}{R^2} \frac{\partial^2 V}{\partial \theta^2} \\ + \frac{\cot \theta}{R^2} \frac{\partial V}{\partial \theta} + \frac{2}{R^2} \frac{\partial U}{\partial \theta} - \frac{V}{R^2 \sin^2 \theta} &= \quad (B-5)\end{aligned}$$

(c) Mass Transfer;

$$\begin{aligned} \frac{\partial \phi}{\partial \tau} + U \frac{\partial \phi}{\partial R} + \frac{V}{R} \frac{\partial \phi}{\partial \theta} \\ = \frac{1}{Sc} \left[ \frac{\partial^2 \phi}{\partial R^2} + \frac{2}{R} \frac{\partial \phi}{\partial R} + \frac{1}{R^2} \frac{\partial^2 \phi}{\partial \theta^2} + \frac{\cot \theta}{R^2} \frac{\partial \phi}{\partial \theta} \right] \end{aligned} \quad (B-6)$$

In order to solve the equations above we must know the appropriate boundary conditions. Initially we have a completely stationary and homogeneous system. At the surface of the sphere  $W = W_0$ . Along the Z-axis ( $\theta = 0, \pi$ ), symmetry requires that the gradient of radial velocity and of concentration with respect to  $\theta$  are zero. In mathematical form

$$\left. \begin{aligned} \text{i) at } \tau = 0, \\ \phi = 0, \quad U = 0, \quad V = 0 \\ \\ \text{ii) at } R = 1, \\ \phi = 1, \quad U = 0, \quad V = 0 \\ \\ \text{iii) at } R = 10 \\ \frac{\partial \phi}{\partial R} = 0, \quad U = 0, \quad V = 0 \\ \\ \text{iv) at } \theta = 0 \text{ and } \pi \\ \frac{\partial \phi}{\partial \theta} = 0, \quad \frac{\partial U}{\partial \theta} = 0, \quad V = 0 \end{aligned} \right\} \quad (B-7)$$

### B. Method of Solution

In order to eliminate the hydrodynamic pressure gradients,  $\frac{\partial P}{\partial R}$  and  $\frac{1}{R} \frac{\partial P}{\partial \theta}$ , from the momentum equations, they were differentiated with respect to  $\theta$  and  $R$  and subtracted from one another.

We define the stream function  $\psi$  and vorticity  $\omega$  by

$$\begin{aligned} U &= \frac{1}{R^2 \sin \theta} \frac{\partial \psi}{\partial \theta}; & V &= \frac{-1}{R \sin \theta} \frac{\partial \psi}{\partial R} \\ \omega &= \frac{1}{R} \left( \frac{\partial U}{\partial \theta} - R \frac{\partial V}{\partial R} - V \right) \end{aligned} \quad (B-8)$$

Since the changes in velocity and composition are expected to occur mainly near the sphere, we substitute  $Z = \ln R$  so that the pertinent equations become:

Mass:

$$\begin{aligned} \frac{\partial \phi}{\partial \tau} + e^{-Z} \left[ e^{-2Z} \frac{\partial (e^{2Z} U \phi)}{\partial Z} + \frac{1}{\sin \theta} \frac{\partial (V \phi \sin \theta)}{\partial \theta} \right] \\ = \frac{e^{-2Z}}{Sc} \left[ \frac{\partial^2 \phi}{\partial Z^2} + \frac{\partial \phi}{\partial Z} + \frac{\partial^2 \phi}{\partial \theta^2} + \cot \theta \frac{\partial \phi}{\partial \theta} \right] \end{aligned} \quad (B-9)$$

Momentum:

$$\begin{aligned} \frac{\partial \omega}{\partial \tau} + e^{-Z} \left[ e^{-Z} \frac{\partial (U e^Z \omega)}{\partial Z} + \frac{\partial (V \omega)}{\partial \theta} \right] \\ - e^{-3Z} \left[ \frac{\partial^2 (\omega e^Z)}{\partial Z^2} - \frac{\partial (\omega e^Z)}{\partial Z} + e^Z \frac{\partial}{\partial \theta} \left[ \frac{1}{\sin \theta} \frac{\partial (\omega \sin \theta)}{\partial \theta} \right] \right] \\ = \frac{-Gr}{8e^Z} \left[ \cos \theta \frac{\partial \phi}{\partial \theta} + \sin \theta \frac{\partial \phi}{\partial Z} \right] \end{aligned} \quad (B-10)$$

Vorticity - Stream Function:

$$\omega = \frac{1}{e^{2Z}} \left[ \frac{1}{e^Z} \frac{\partial}{\partial \theta} \left( \frac{1}{\sin \theta} \frac{\partial \psi}{\partial \theta} \right) + \frac{1}{\sin \theta} \frac{\partial}{\partial Z} \left( \frac{1}{e^Z} \frac{\partial \psi}{\partial Z} \right) \right] \quad (B-11)$$

Stream Function - Velocity:

$$U = \frac{1}{e^{2Z}} \frac{1}{\sin \theta} \frac{\partial \psi}{\partial \theta} \quad (B-12)$$

$$V = \frac{-1}{e^{2Z}} \frac{1}{\sin \theta} \frac{\partial \psi}{\partial Z} \quad (B-13)$$

Boundary Conditions:

The vorticities at the solid-liquid interface ( $Z = 0$ ) can be computed from a Taylor series expansion. Along the interface,  $\frac{\partial}{\partial \theta} \left[ \frac{1}{\sin \theta} \frac{\partial \psi}{\partial \theta} \right]$  and  $\frac{\partial \psi}{\partial Z}$  are zero,  $\omega = \frac{1}{\sin \theta} \frac{\partial^2 \psi}{\partial Z^2}$ . Using a Taylor expansion,

$$\psi_{i,m+1} = \psi_{i,m} + \frac{\partial \psi_{i,m}}{\partial Z} \frac{\Delta Z}{1!} + \frac{\partial^2 \psi_{i,m}}{\partial Z^2} \frac{(\Delta Z)^2}{2!} + \frac{\partial^3 \psi_{i,m}}{\partial Z^3} \frac{(\Delta Z)^3}{3!} + \dots \quad (B-14)$$

$$\psi_{i,m+2} = \psi_{i,m} + \frac{\partial \psi_{i,m}}{\partial Z} \frac{2\Delta Z}{1!} + \frac{\partial^2 \psi_{i,m}}{\partial Z^2} \frac{(2\Delta Z)^2}{2!} + \frac{\partial^3 \psi_{i,m}}{\partial Z^3} \frac{(2\Delta Z)^3}{3!} + \dots \quad (B-15)$$

At the surface  $Z = 0$ ,  $\psi_{i,m} = 0$  and  $\frac{\partial \psi_{i,m}}{\partial Z} = 0$ .

We can derive the following equation

$$\frac{\partial^2 \psi_{i,m}}{\partial Z^2} = \frac{8\psi_{i,m+1} - \psi_{i,m+2}}{2(\Delta Z)^2} \quad (B-16)$$

In addition, the concentration and radial velocity at  $\theta = 0$  and

$\pi$  are:

At  $Z = 0$ ,

$$\omega_{i,m}^{n+1} = \frac{8\psi_{i,m+1}^{n+1} - \psi_{i,m+2}^{n+1}}{2(\Delta Z)^2 \sin(i\Delta\theta)} \quad (\text{B-17})$$

At  $\theta = 0$ ,

$$\phi_{m,j}^{n+1} = \frac{4\phi_{m+1,j}^{n+1} - \phi_{m+2,j}^{n+1}}{3} \quad (\text{B-18})$$

$$U_{m,j}^{n+1} = \frac{4U_{m+1,j}^{n+1} - U_{m+2,j}^{n+1}}{3} \quad (\text{B-19})$$

At  $\theta = \pi$ ,

$$\phi_{m,j}^{n+1} = \frac{4\phi_{m-1,j}^{n+1} - \phi_{m-2,j}^{n+1}}{3} \quad (\text{B-20})$$

$$U_{m,j}^{n+1} = \frac{4U_{m-1,j}^{n+1} - U_{m-2,j}^{n+1}}{3} \quad (\text{B-21})$$

The computer program used was very time-consuming because we used a double-stability-checking DO loop. The convergence criterion used were as follows:

$$\frac{\text{Max}_{i,j} |\psi_{i,j}^{n+1} - \psi_{i,j}^n|}{\text{Max}_{i,j} |\psi_{i,j}^n|} \leq 10^{-4} \quad (\text{B-22})$$

$$\frac{\text{Max}_{i,j} |v_{i,j}^{n+1} - v_{i,j}^n|}{\text{Max}_{i,j} |v_{i,j}^n|} \leq 10^{-3} \quad (\text{B-23})$$